

# **Numerical Modeling of SLD Secondary Droplet Flows for in-Flight Icing**

**David Bilodeau**

Department of Mechanical Engineering

McGill University

Montreal, Québec

August 2016

A Thesis Submitted to McGill University in

Partial Fulfillment of the Requirements of the Doctor of Philosophy

© David Bilodeau, 2016

## **ACKNOWLEDGEMENTS**

While many individuals have contributed to the completion of my thesis, I wish to explicitly thank a few individuals for their assistance and mentoring. Firstly, I wish to acknowledge my supervisor Dr. Wagdi G. Habashi for his guidance and help during my time at the McGill University CFD Laboratory. In addition, I wish to express my appreciation for Dr. Marco Fossati, my co-supervisor, and the invaluable discussions, guidance, and direction he provided during my Masters and PhD thesis work.

Dr. Guido Baruzzi, at Newmerical Technologies International (now ANSYS-Montreal) has provided me with excellent and constructive criticism of my work over the past years, enabling me to see potential problems I had not considered, and offering potential solutions to move past them. Dr. Baruzzi has answered my questions and offered additional training and knowledge that has enabled me to work through many of the details involved with the completion of my thesis. I also wish to thank my colleagues in the CFD Laboratory for their help and insights both in our formal meetings and in informal encounters at other times. I most appreciated the friendship of and discussions with Ahmed Bakkar who has been a sounding board to my more outlandish ideas and helped me work through some of the problems I have faced.

I wish to thank McGill University, the CFD Laboratory and Hydro-Québec for the generous financial support that has made it possible to conduct my research. I also wish to thank CLUMEQ and Compute Canada for the computational resources offered on supercomputing clusters, without which many of the test cases in my thesis would have been difficult if not impossible to complete in a reasonable timeframe.

Above all, I would like to thank my loving and supportive wife Sydney who, along with my children, gave me so much love, support, confidence and encouragement during the long journey through my schooling. I am grateful for them picking me up when I am down, for them celebrating my successes and for their reminder that in the end, they love me through it all.

## CONTENTS

Acknowledgements.....	i
Abstract.....	v
Résumé.....	vii
List of Figures .....	ix
List of Tables .....	xiv
List of Symbols .....	xiv
Chapter I Introduction .....	1
I.1 Thesis Contributions.....	4
I.1.1 Algorithmic/Model Developments.....	4
I.1.2 Engineering Contribution .....	5
Chapter II Numerical Approaches to In-Flight Icing.....	7
II.1 Numerical Modeling of Droplet Impingement.....	8
II.2 PDEs Governing Droplet Impingement in an Eulerian Frame of Reference .....	9
II.3 Numerical Treatment of Surface Films and Runback.....	12
II.4 PDEs Governing Runback .....	13
Chapter III Literature Review .....	15
III.1 Droplet-Wall Interactions Approaches .....	15
III.2 Clustering Approaches & Stopping Criteria .....	18
III.2.1 Variance Ratio Criterion .....	20
III.2.2 The Sum of Squared Error $J_e$ .....	20
III.2.3 C-Index.....	21
III.3 Droplet Departure Models.....	21
III.3.1 Jet Pinch-off.....	22

III.3.2 Sheet Breakoff.....	23
III.3.3 Isolated Droplet.....	24
Chapter IV Numerical Modeling of Splashing and Bouncing: The Clustered Approach.....	26
IV.1 Clustering Explained.....	27
IV.1.1 Distance Metric.....	29
IV.1.2 Hierarchical Clustering Approaches.....	30
IV.1.3 Stopping Criteria.....	33
IV.1.4 An Example of Clustering Inlet Facets.....	33
IV.2 PDE Restrictions on Boundary Conditions.....	36
IV.3 Two-dimensional Test Cases.....	37
IV.3.1 Non-clustered Testing with Interacting Components.....	37
IV.3.2 Clustered Approach with Complex Interacting Components.....	39
IV.4 Three-dimensional Test Case.....	41
Chapter V Numerical Modeling of Droplet Detachment from Trailing Edges.....	46
V.1 Two-dimensional Model.....	46
V.1.1 Two-dimensional Model Details.....	46
V.1.2 Model Sensitivity.....	49
V.1.3 Two-dimensional Trailing Edge Detachment Test Case.....	52
V.1.4 Limitations.....	53
V.2 Three-dimensional Model.....	55
V.2.1 Model Explained.....	55
V.2.2 Integration within a Multishot approach.....	59
V.2.3 Model Validation.....	60
V.2.4 Test Case.....	62

V.2.5 Limitations.....	69
Chapter VI Isolated Rotor in Hover.....	71
Chapter VII Conclusions .....	86
Chapter VIII Future Work.....	90
Chapter IX References.....	91

## **ABSTRACT**

In-flight ice accretion poses a serious risk to the safety of air travel as it may cause performance degradation and loss of control. It is reported as being the cause of many incidents and accidents. Most of the supercooled droplets encountered during flight conditions are small in nature and, as such, adhere quickly to the surface where they impinge and either freeze where they first impact the surface or runback along the surface due to aerodynamic forces acting on the droplets during the freezing process. On the contrary, when supercooled large droplets (SLD) impinge on a surface, they may stick, fragment and splash, or bounce back into the airstream surrounding the surface. These rebounded droplets may impinge at an unprotected location on an aircraft. Additionally, the larger droplets may runback along the surface with a longer freezing time, arriving at a trailing edge and be entrained again in the airflow.

An Eulerian approach to account for the secondary droplet flow resulting from splashing and bouncing of supercooled large droplets on aircraft surfaces is presented and optimized to reduce computational cost via statistical clustering approaches. The numerical approach presented decouples pre- and post-impact conditions into separate computational domains. After computing the post-impact computational simulations to account for splashed and bounced droplets, the pre- and post-impact solutions are combined for a final solution, having conserved mass in the system. In the proposed approach, each surface facet could be a unique secondary simulation. As the computation of an additional simulation for each surface facet is quite high, statistical approaches are used to combine the secondary solutions to provide a lower cost approach to estimate the effect of splashing and bouncing on aircraft surfaces. Criteria are proposed for grouping predicted secondary droplets, and are tested on a multi-

element two-dimensional airfoil. Comparison with experiment shows improvement over simple post-processing, non-conservative approaches, with an acceptable level of error compared to a costly, straightforward non-clustered approach. The approach is then applied to a three-dimensional multi-element wing with flap and slat extended and the effect of the splashing and bouncing on a five-minute ice accretion is examined.

A two-dimensional model to determine the minimum size of liquid droplets detaching from a geometric corner is proposed first. The model lacks validation and when extended to three-dimensions, the assumption of one-way coupling with the airflow is deemed inappropriate. A three-dimensional model to predict the detaching of droplets from a geometric corner is then proposed and validated against the limited experimental data available for detachment from a flat plate. This is accomplished by assuming that the angle subtending the corner approaches  $180^\circ$ . The model compares well with the limited experimental data for detaching droplet sizes. Subsequently, the model is applied to a three-dimensional wing with minimal observed effect on the ice accreted in time. Additionally, the model is applied to turbomachinery problems where the higher liquid water content and shorter chord length is presumed to increase the effect of the secondary droplets on the downstream components. Minimal effect was again observed of the detaching mass from the trailing edge of a turbofan blade.

Finally, the splashing and bouncing approach along with the detachment model are applied to a three-dimensional rotor in hover to assess the potential effect of secondary droplets on a helicopter in flight, which, again, proves minimal.

## RÉSUMÉ

Le givrage en vol représente un risque grave pour la sécurité aérienne pouvant causer des pertes de performance conduisant à une perte de contrôle. Le phénomène est la cause de nombreux incidents et accidents. La majorité des gouttelettes surfondues rencontrées en vol sont de petite taille et adhèrent rapidement aux surfaces qu'elles impactent. Elles gèlent soit immédiatement ou s'écoulent le long de la surface, portées par les forces aérodynamiques. Lorsque des gouttelettes plus grosses, dites SLD, impactent la surface, elles peuvent être soit coller à la surface, s'étendre, se fragmenter et éclabousser, ou rebondir dans le courant d'air. De telles gouttelettes qui rebondissent, lorsqu'elles se réintègrent au flux d'air, peuvent impacter d'autres régions non-protégées, en aval sur l'avion. De plus, elles peuvent s'écouler jusqu'en en bordure de la surface et réintégrer le flux d'air.

Une approche Eulérienne est présentée, tenant compte de l'écoulement secondaire de gouttelettes SLD causé par leur éclatement et rebondissement. Le coût de calcul est optimisé par une méthode de regroupement statistique. L'approche numérique découple les conditions pré- et post-impact en des domaines de calcul indépendants. Suite à ce processus, les solutions pré- et post-impact sont combinées en une solution finale conservant la masse totale du système. Dans cette méthodologie, chaque facette surfacique est en effet une simulation secondaire unique. Le temps et coûts de calcul de telles simulations supplémentaires étant très élevés, des approches statistiques sont utilisées. Des critères de partitionnement des gouttelettes secondaires sont testés sur une aile à éléments multiples en deux dimensions. La comparaison avec les données expérimentales démontre une amélioration par rapport à un

simple post-traitement des données, ainsi qu'en comparaison aux approches non conservatrices. La méthodologie est acceptable par rapport à l'approche assez coûteuse sans partitionnement. L'approche est par la suite appliquée à une aile tridimensionnelle à rabat et latte étendus et les effets d'éclaboussure et rebondissement sont examinés après cinq minutes de cumul de glace. Par la suite, un modèle bidimensionnel est proposé pour déterminer la taille minimale de gouttelettes pouvant s'arracher à partir d'un coin géométrique. Le modèle manque toutefois de validation et, lorsqu'il est étendu à trois dimensions, l'hypothèse d'un couplage à sens unique avec le flux d'air est jugée inappropriée. Un modèle tridimensionnel est alors proposé et validé sur une plaque plane. Le modèle se compare bien avec les données expérimentales et est appliqué à une aile, démontrant un effet minime sur l'impact global. Finalement, le modèle est appliqué à un problème de turbomachines où la teneur plus élevée en eau liquide et la plus courte longueur de corde sont présumés augmenter l'effet des gouttelettes secondaires sur les composantes en aval. Un effet minimal est à nouveau observé. Enfin, l'approche est appliquée à un rotor d'hélicoptère en vol stationnaire pour évaluer l'effet potentiel de gouttelettes secondaires, et, à nouveau, l'effet se montre minimal.

## LIST OF FIGURES

Figure I-1 Possible rime and glaze ice shapes [9] .....	2
Figure II-1: Modular Approach used in FENSAP-ICE [10, 13, 17, 19-21].....	7
Figure II-2: A summary of the mass and energy transfer for a control volume in the ICE3D framework from [30]. .....	12
Figure III-1: Types of surface runback during the icing process from Fortin, <i>et al.</i> [57] .....	22
Figure III-2: Apparatus used by Lasheras, <i>et al.</i> [62] to study jet pinch-off in the presence of a co-flowing gas .....	23
Figure III-3: Two-dimensional view of the sheet generator in the experiments of Mansour and Chigier [58].....	23
Figure III-4: Surface tension force on a spherical cap shape from Kumbur, <i>et al.</i> [56].....	24
Figure IV-1: Framework to compute rebound solutions where each facet is a separate simulation. ....	28
Figure IV-2: Re-injection framework for splashing and bouncing with statistical clustering introduced.....	28
Figure IV-3: Single linkage for a grouping of 4 points in a two-dimensional plane. Progressing from left to right, a single link is defined based on the minimum distance between points in each cluster.....	31
Figure IV-4: Complete linkage for a grouping of 4 points in a two-dimensional plane. Progressing from left to right, a single link is defined based on the maximum distance between points in each cluster.....	31
Figure IV-5: $ L_2 $ of the error contained within the clusters employing the different linkage approaches.....	32
Figure IV-6: $ L_\infty $ of the error contained within the clusters given the different linkage approaches.....	32
Figure IV-7: A sample dataset (left) showing the first 3 dimensions in one of the 8-dimensional spaces tested with the identified clusters (right).....	33
Figure IV-8: Normalized droplet rebound diameter contours on the Trap-wing geometry. The primary diameter was 391.775 $\mu\text{m}$ .....	34

Figure IV-9: Predicted inlet velocities for the rebounded droplets. Surface contours denote the normalized magnitude of the inlet velocity..... 35

Figure IV-10: Predicted clusters for this single primary diameter..... 36

Figure IV-11: Detail of the computational mesh near the airfoil for the McDonnell Douglas LB606b. The mesh contains 235,000 nodes ..... 38

Figure IV-12: Comparison of the collection efficiency for the non-clustered treatment of splashing and bouncing on the slat (left), main element (center), and flap (right) ..... 39

Figure IV-13: Collection efficiency for the Appendix O validation case comparing the non-clustered (w/ re-injection) and clustered (w/ re-injection clustered) approach to a simple post-process (w/o re-injection) for the slat (left), main element (center) and flap (right) ..... 40

Figure IV-14: Normalized lift penalty and drag increase comparison between the non-clustered and clustered approach for 30 minutes of ice accretion..... 41

Figure IV-15: Cumulative distribution for the 10 diameters used to approximate the MVD=92  $\mu\text{m}$  distribution from Papadakis, *et al.* [71]..... 42

Figure IV-16: Sample LWC contours of the splashed and bounced droplet mass using 89 clusters. .... 43

Figure IV-17: Comparison of the Collection Efficiency considering splashing and bouncing. Insets show  $\beta_{clustered} - \beta_{post-process}$  to highlight the effect of the secondary droplets..... 43

Figure IV-18: A comparison of the iced regions considering 5 minutes at the test conditions ... 44

Figure IV-19: The total collection efficiency as a function of the total clusters. The red dot shows the clustered approach with the stopping criterion..... 45

Figure V-1: Model of a two-dimensional isolated droplet at a geometric corner..... 47

Figure V-2: Regions where droplet remains attached and regions where detachment is assumed to occur. .... 47

Figure V-3: A representative result of the one-at-a-time sensitivity study for the conditions evaluated ..... 51

Figure V-4: Typical results of the 2 Variable sensitivity study perturbing the shear stress and pressure at the detachment location (Left) and the most extreme result of the 2-Variable sensitivity study (Right)..... 52

Figure V-5: LWC contours from the re-injection of detached droplets.....	53
Figure V-6: The channel of Theodorakakos, <i>et al.</i> [77] without (left) and with (right) an artificial droplet in the air path. Significant pressure variation exists around the droplet.....	55
Figure V-7: Spherical cap shape, located at trailing edge of an airfoil, projected into two dimensions.....	56
Figure V-8: Intersection of the assumed droplet with a surface on one side of the corner. ....	56
Figure V-9: Static and Dynamic contact angles for various droplet sizes as reported by Theodorakakos, <i>et al.</i> [77] as Figure 7.....	60
Figure V-10: Comparison between the experimental data of Theodorakakos, <i>et al.</i> [77], Volume of Fluid results from Theodorakakos and the results of the proposed detachment model for three surface A) a carbon cloth, B) a carbon paper and C) a second type of carbon paper .....	62
Figure V-11: Change in collection efficiency comparing no detachment to the predicted effect of detachment. The final difference is very small and is highlighted (right). ....	63
Figure V-12: Turbofan geometry studied .....	64
Figure V-13: Mach contours around the turbofan blade along with select streamlines. ....	65
Figure V-14: Pressure contours at several radial positions on the turbofan blade.....	66
Figure V-15: Iso surfaces showing the effect of the detached droplets.....	67
Figure V-16: LWC at the exit planes from 3 turbofan blades .....	68
Figure V-17: Final LWC contours from both the primary and detached droplets as they will affect the first compressor stage of the geometry studied.....	69
Figure VI-1: Appendix O Distribution with discrete diameters used to approximate the conditions.....	72
Figure VI-2: Initial mesh employed to study the Caradonna geometry. Full mesh (left), detail of rotor (top-right) and structured layers near the rotor tip (bottom-right) .....	73
Figure VI-3: Mesh employed to study the NACA 0012 rotor after 3 levels of adaptation and enrichment. Full mesh (left), detail of rotor (top-right) and structured layers near the rotor tip (bottom-right).....	73
Figure VI-4: Pressure coefficient computed at $r/R = 0.50$ as compared to Caradonna and Tung [81] .....	74

Figure VI-5: Pressure coefficient computed at $r/R = 0.68$ as compared to Caradonna and Tung [81] .....	74
Figure VI-6: Pressure coefficient computed at $r/R = 0.80$ as compared to Caradonna and Tung [81] .....	75
Figure VI-7: Pressure coefficient computed at $r/R = 0.96$ as compared to Caradonna and Tung [81] .....	75
Figure VI-8: Sample pressure coefficient at $r/R = 0.50$ , when a freestream temperature of $-3^{\circ}\text{C}$ is employed to permit ice accretion, compared to Caradonna and Tung at $24^{\circ}\text{C}$ [81] .....	76
Figure VI-9: Droplet streamlines (left) in the Y-X plane. Iso-surface showing the shadow region and slice showing LWC contours (top-right). Collection efficiency ( $\beta$ ) on the blades (bottom-right).....	77
Figure VI-10: Collection efficiency on the surface of a single rotor blade from a post-processing approach .....	78
Figure VI-11: Collection efficiency on the surface of a single rotor blade following re-injection and re-impingement .....	78
Figure VI-12: Collection efficiency on the surface of a single rotor blade, comparing a post-process and re-injected approach .....	79
Figure VI-13: Collection efficiency comparing primary impingement and final solution post re-injection at $r/R = 0.201$ .....	79
Figure VI-14: Collection efficiency comparing primary impingement and final solution post re-injection at $r/R = 0.402$ .....	80
Figure VI-15: Collection efficiency comparing primary impingement and final solution post re-injection at $r/R = 0.604$ .....	81
Figure VI-16: Collection efficiency comparing primary impingement and final solution post re-injection at $r/R = 0.805$ .....	81
Figure VI-17: Collection efficiency comparing primary impingement and final solution post re-injection at $r/R = 0.938$ .....	82
Figure VI-18: Mach contours near the tip of the Caradonna geometry with select streamlines to show the tip vortices.....	82

Figure VI-19: Primary droplet streamlines due to tip vortices. Surface contour is LWC..... 83

Figure VI-20: LWC contours from the re-injected droplets. Values below 2E-07 are blanked .... 84

Figure VI-21: LWC contours on the rotor and at a distance  $y/R=0.10$  below the rotor. Values below 1E-7 are truncated to better show the region potentially impacted by the re-injection . 84

## LIST OF TABLES

Table IV-1: Parameters from the work of Papadakis, <i>et al.</i> [71] on the LB606b test case.....	38
Table IV-2: Summary of conditions used for the validation of the clustering approach.....	40
Table IV-3: Summary of test conditions for the Trap-wing case .....	41
Table V-1: Geometric characteristics of the MD LB606b airfoil .....	50
Table V-2: Test conditions for the sensitivity study. Common conditions: characteristic length (L) = 0.9144 m and $T_{\infty} = 268.15$ K .....	51
Table V-3: Summary of test conditions for the Trap-wing case .....	63
Table V-4: Summary of test conditions for the turbofan case .....	64
Table V-5: Results of the detached mass.....	67
Table VI-1: Summary of test conditions for the isolated rotor case.....	71
Table VI-2: Change in Collection Efficiency due to splashing and bouncing effects .....	78

## LIST OF SYMBOLS

$\dot{x}$	the flux of x
$\vec{x}$	the vector quantity of x
$\hat{x}$	a unit vector of x
$\beta$	collection efficiency or measure of local impinging flux non-dimensionalized by free-stream liquid mass flux
$m$	mass
$\dot{m}$	mass flux of ice
$\dot{q}$	heat flux
$T_{wall}$	wall temperature
$\dot{\tau}$	wall shear stress

$\vec{i}_a$	velocity vector of the airflow
$\vec{i}_d$	velocity vector of the droplet flow
$m_s$	rebounded mass
$m_o$	original mass
$d$	droplet diameter
$d_s$	splashed droplet diameters
$d_o$	incident droplet diameters
$L$	characteristic length
$V_{t,s}$	tangential component of velocity of splashed droplets
$V_{t,o}$	tangential component of velocity of incident droplets
$V_{n,s}$	normal component of velocity of splashed droplets
$V_{n,o}$	normal component of velocity of incident droplets
$\vec{i}_a$	primary droplet impingement velocity
$\vec{i}_{a,jmai}$	droplet impingement velocity due to primary and rebounded mass
$\rho_w$ or $\rho_d$	density of water ( $\text{kg}/\text{m}^3$ )
$\rho_a$	density of air ( $\text{kg}/\text{m}^3$ )
$h_f$	height of the film during ice accretion (m)
$\theta_i$	incident droplet angle ( $^\circ$ ) measured from the surface tangential plane toward normal vector
$f_u = \frac{u_s}{u_o}$	ratio of rebound velocity to incident velocity
$f_m = \frac{m_s}{m_o}$	ratio of rebounded mass to incident mass

$f_d = \frac{d_s}{d_o}$  ratio of rebounded droplet diameter relative to incident droplet diameter

$f_N = \frac{N_s}{N_o}$  ratio of the number of rebounded droplets relative to incident droplets

$\bar{i}_D$  drag force in Eulerian droplet momentum equations

$\bar{i}_G$  gravitational force in Eulerian droplet momentum equations

$\bar{i}_B$  buoyancy force in Eulerian droplet momentum equations

$\bar{i}_S$  splash force in Eulerian droplet momentum equations as proposed by Honsek in the Body Force approach

$LWC = \frac{m_d}{V_{tot}} = \rho_d \frac{V_d}{V_{tot}}$  liquid water content or the ratio of the mass of water per unit volume of fluid ( $\text{kg}/\text{m}^3$ )

$LWC_o$  liquid water content predicted from primary impingement ( $\text{kg}/\text{m}^3$ )

$LWC_s$  liquid water content predicted to splash from the splashed mass ratio ( $\text{kg}/\text{m}^3$ )

$LWC_{rebnd}$  summation of LWC predicted by the secondary impingement solutions ( $\text{kg}/\text{m}^3$ )

$MVD$  median volumetric diameter ( $\mu\text{m}$ )

$K = \frac{\rho_d d^2 U_\infty}{18L\mu_a}$  non-dimensional droplet inertia parameter

$C_D = \begin{cases} \frac{24}{Re_d} (1 + 0.15 Re_d^{0.687}) & Re_d \leq 1300 \\ 0.40 & Re_d > 1300 \end{cases}$  drag coefficient used for smaller droplets

$C_D = \begin{cases} (1.0 - f)C'_D + fC''_D & We_b \leq 12 \\ C'_D & We_b > 12 \end{cases}$  drag coefficient used for larger droplets

$f = 1.0 - (1.0 + 0.07\sqrt{We_b})^{-6}$  eccentricity used in the large droplet drag model

$C'_D$  drag coefficient of an oblate disk

$C''_D$  drag coefficient of a sphere

$\Lambda'$  local volumetric fraction of water to air

$\Lambda = \frac{\Lambda'}{\Lambda'_\infty} = \Lambda' \left[ \frac{\rho_d}{LWC_\infty} \right]$  the non-dimensional local volumetric fraction of water to air

$\alpha = \ln \Lambda$  the natural log of the local volume fraction of water to air

$C_D$  Drag coefficient

$Re = \frac{\rho V L}{\mu}$  Reynolds number, a measure of the ratio of inertial to viscous forces

$Re_D = \frac{\rho V_D d}{\mu}$  Droplet Reynolds number

$We = \frac{\rho V^2 L}{\sigma}$  Weber number, a measure of the ratio of the inertial to surface tension forces

$We_s = \frac{\rho V_n^2 d}{\sigma}$  Surface Weber number

$We_{s,c}$  Critical Surface Weber Number defined in the Bai and Gosman droplet-wall interaction model

$K_c = Oh^{-2/5} We_s$  Cossali parameter

$K_W = K_c^{0.859} \left( \frac{\rho_w}{LWC} \right)^{0.125}$  Wright modified Cossali parameter, or LEWICE splashing parameter

$Oh = \frac{\mu}{\sqrt{\rho \sigma d}} = \frac{\sqrt{We}}{Re}$  Ohnesorge number, the ratio between the viscous to surface tension and inertial forces

$La = \frac{\sigma \rho d}{\mu^2} = \frac{Re^2}{We}$  Laplace number, the ratio of the surface tension to viscous forces

$Fr = \frac{U_\infty}{\sqrt{Lg}}$  Froude number, the ratio of the inertial to gravitational forces

$\varepsilon$  Solid emissivity

$\rho_f$  density of the fluid ( $\text{kg}/\text{m}^3$ )

$c_f$  specific heat of the fluid ( $\text{J}/\text{kg}\cdot\text{K}$ )

$c_s$  specific heat of the solid ice ( $\text{J}/\text{kg}\cdot\text{K}$ )

$\sigma$  surface tension ( $\text{N}/\text{m}$ )

$L_{evap}$  latent heat of evaporation ( $\text{J}/\text{kg}$ )

$L_{fusion}$  latent heat of fusion ( $\text{J}/\text{kg}$ )

$T$  temperature either asymptotically or locally ( $\text{K}$ )

$\tilde{i}$  ice recovery temperature ( $^\circ\text{C}$ )

$\bar{v}_d$  velocity of the droplets upon impingement ( $\text{m}/\text{s}$ )

$\tilde{i}$  temperature either asymptotically or locally ( $^\circ\text{C}$ )

$J_e(2)/J_e(1)$  the stopping criteria of Duda and Hart [1]

$VRC = \left( \frac{BCSS}{k-1} \right) / \left( \frac{WCSS}{n-k} \right)$  the variance ratio of Calinski and Harabasz [2] used for clustering

$BCSS$  between cluster sum of squared error

$WCSS$  within cluster sum of squared error

$n$  number of unique data sets being clustered

$k$  number of clusters

$\zeta$  the z-score from the percentile confidence level

$d_c$  the dimensionality of the distance/dissimilarity used for clustering

$J_e(m) = \sum_{i=1}^m \sum_{s \in \chi_i} (s - \bar{\mu}_i)^2$  the error contained within the m cluster(s) being considered

$\chi_i$  a cluster

	$s$	an individual data point
	$\bar{\mu}_i$	mean of the samples in the $\chi_i$ cluster
$C = [d_w - \min d_w] / [\max d_w - \min d_w]$		C-index from Hubert and Levin [3]
	$d_w$	the sum of the within cluster distances/errors
$\cos(\theta_{ij})$		the angle between the $i$ inlet node re-injection velocity vector and the direction vector joining the $i$ and $j$ re-injection nodes (rad)
	$D_i$	diameters of the $i$ re-injection droplet (m)
	$\hat{V}_i$	$i^{\text{th}}$ unit re-injection boundary vector
	$D$	diameter of the primary droplet before impingement (m)
	$\theta$	static contact angle between droplet and surface (rad)
	$P_{0(r)}$	the pressure at the trailing edge node in the two-dimensional detachment model (Pa)
	$P_{s(r)}$	the pressure in the field above the trailing edge in the two-dimensional detachment model (Pa)
	$\psi$	denotes the angle of the corner at the trailing edge (rad)
$r > r_{crit} = \sqrt{\frac{0.06 * \sigma}{g(\rho_{water} - \rho_{air@corner})}}$		critical radius for the inclusion of body forces from Zhang, <i>et al.</i> [4]
$F_{drag} = K_1 \frac{1}{2} C_{drag} \rho_{gas} U^2 A_p$		drag force (N)
	$K_1$	corrective coefficient either from experiment or analytical results
	AoA	Angle of attack

## Chapter I INTRODUCTION

In-flight ice accretion poses a serious risk to the safety of air travel. Ice accretion may cause performance degradation and loss of control and is reported as being the cause of many incidents and accidents [5]. In order to enhance the safety of flight into known icing conditions, standards of certification have been adopted in the FAA's "Appendix C" [6], based on temperature, pressure, altitude, droplet size and the water content of the icing cloud. Any class of passenger-carrying aircraft must demonstrate safe operation within that entire envelope for certification. "Appendix O" [7] has recently been implemented which extends the range of aero-icing conditions required for certification to include the effect of so-called Supercooled Large Droplets (SLD), defined as droplets exceeding 100 microns in diameter. SLD have been identified as the causes of accidents and incidents starting with the crash of an ATR-72 in 1994 [8].

Depending on the aircraft's surface temperature and water properties such as impinging velocity and size, a droplet may freeze at the location of initial impingement leading to rime ice. If the droplet does not completely freeze at the site of initial impingement, water mass is driven downstream in the form of a shear-driven liquid film that refreezes further downstream, leading to glaze ice. Rime ice shapes are characterized by relatively streamlined profiles that follow the shape of the clean surface, whereas glaze ice shapes are defined by irregularities such as ridges, horns and feather-like structures. Glaze ice formation, in particular, leads to significant degradation in aerodynamic performance of both lifting and control surfaces. Figure I-1 shows possible glaze and rime ice shapes.

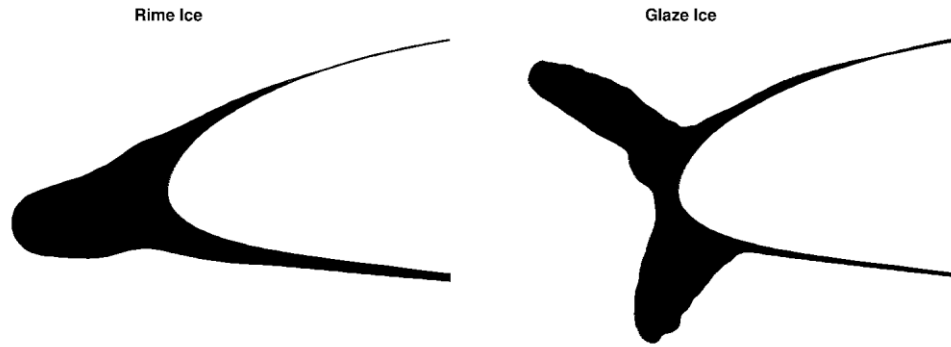


Figure I-1 Possible rime and glaze ice shapes [9]

Large droplet dynamics and impact behavior is different from small droplets as these can distort, break up before impingement, splatter, bounce and shatter. In the SLD regime, a post-splashing flow of droplets thus “re-enters” the airstream and these secondary, smaller droplets can be easily carried to areas that are not directly exposed to primary impingement or impacted by run-back conditions and, as a consequence, these might not have been considered in the design of ice protection systems (IPS) [5, 10].

Due to their large diameters, droplets in the SLD range can no longer be classified as being stratified in the atmosphere but appear much more like droplet clouds falling at terminal velocity. Hence, additional velocity components, with a magnitude dictated by the terminal velocity, are needed to model the effect of the gravitational forces [10-12]. Droplets will also deform due to the aerodynamic shear forces, resulting in a non-spherical shape that will cause an increase in the effective drag as compared to that of a spherical droplet. This aerodynamic shear may also eventually lead to breakup of the droplets resulting in a reduction of the median volumetric diameter (MVD) of the droplet prior to impingement [10-12].

Depending on several characteristic impingement conditions – namely the non-dimensional surface roughness, surface film height, and the normal component of droplets’ momentum relative to the surface – the droplet-wall interaction may result in either complete deposition of the droplet mass at the location of initial impingement, or a partial deposition with a portion of the mass being re-introduced into the flow. Splashing is typically defined as having a relatively

low splashed to primary impinging mass ratio (or in other words, where the quantity of mass that rebounds is significantly less than that of the primary impingement), whereas ‘bouncing’ approaches a complete returning of all impinging mass to the free-stream. Additionally, splashing typically results in fragmentation of the droplets upon impact with the surface, causing the rebounded droplet diameters to be much smaller than that of the primary. In the case of “Appendix C” conditions, the momentum of the impinging droplets is low enough to justify the assumption that the amount of mass being re-introduced into the flow is negligible, with the deposition resulting in either glaze or rime ice after it freezes. For impingement conditions in the “Appendix O” envelope, however, both numerical and experimental studies have shown that it is quite possible for a non-negligible fraction of the impinging mass to re-enter the flow and re-impinge on a surface downstream of the ice protection systems [10, 13].

As manufacturers aim for certification using the new “Appendix O” rules in the design of their ice protection systems, the numerical models that were designed for the maximum MVD of 40  $\mu\text{m}$  of “Appendix C” need to be amended. Within the context of “Appendix C”, assumptions were made that are no longer valid in the SLD regime, namely:

- Droplets travel at the free stream velocity relative to the approaching airfoil
- Droplets maintain a spherical geometry along their impingement trajectories
- Droplets do not break up due to aerodynamic shear in the vicinity of the airfoil
- Droplets do not coalesce, bounce or splash upon impact with the aircraft surface

Different methods have been suggested to extend numerical simulation codes to impingement within the SLD regime such as the Honsek-Habashi Body Force approach [10, 13] or the Wright-Potapczuk Lagrangian approach [14-16].

In addition to the need to model droplet rebound due to splashing and bouncing in the Appendix O regime, it is possible that depending on the impinging and surface conditions, those droplets still in the liquid state on the surface may coalesce to form rivulets or a thin film [17]. That liquid is subject to pressure and shear forces that drive it along the surface where, depending on the balance of energy, it may freeze or could detach and then impinge on other

downstream surfaces. Though detachment on a surface is classified as a second order effect [15], there are cases where it is possible that the effect of liquid detachment from a surface may have an impact on the impingement characteristics of downstream components.

Since the accurate prediction of wetted regions and quantity of mass caught is needed for the design of ice protection systems (IPS) and for overall safety analysis, an efficient approach is required to account for re-injected water and detection of secondary wetted regions. This thesis will specifically address the following three problems: modeling the liquid-surface interaction to determine if splashing/bouncing occurs, the prediction of detachment due to the presence of a surface end, and numerically addressing the re-injection of mass from surface locations back into the flow and tracking its path to determine where secondary impingement occurs (if any).

## **I.1 Thesis Contributions**

This thesis makes contributions both in terms of model development as well as in the understanding of the impact of SLD on realistic geometries. In terms of modeling, approaches are provided to explore some of the complex physics of SLD splashing and bouncing and detachment. These approaches are applied to better understand the effect of SLD on both fixed-wing aircraft and on rotating components.

### **I.1.1 Algorithmic/Model Developments**

This thesis makes fundamental contributions to the numerical modeling of droplet rebound/detachment for in-flight icing conditions, summarized as:

- A two-dimensional approach for modeling splashing and bouncing of supercooled large droplets in an Eulerian framework has been extended to three-dimensions.
- An alternative, lower cost approach was developed by making use of statistical clustering to group surface facets with unique inlet conditions. While this grouping does introduce an error in the form of a systemic bias, the magnitude of the error is deemed acceptable for a lower cost tool to justify the additional computational expense of the non-clustered approach.

- Criteria are proposed to assign a dissimilarity/error value between facets and clusters for the purpose of grouping unique inlet conditions.
- Both a two-dimensional and a three-dimensional droplet detachment model are proposed. The three-dimensional model is partially validated and then applied to both aircraft and turbomachinery geometries.

### **I.1.2 Engineering Contribution**

This thesis makes significant engineering contributions to the assessment of SLD effects on aircraft:

- The clustered approach is applied to a multi-element Trap-wing with slat and flap extended and a comparison is made between a post-process approach and the clustered approach. An almost 25% increase in the mass of ice in five minutes is found with significant increases to the ice affected regions of the lower surface, leading to potentially greater drag due to surface roughness.
- When the clustered approach is applied to an isolated rotor in a hover condition, relatively little difference is found on both the rotor and at a distance below the rotor indicative of the distance to a rotorcraft body. In this case, the clustered approach confirms what engineering judgement would suggest, that very little SLD splashing and bouncing will re-impinge and the added expense of computing the non-clustered approach is not needed.
- Application of the three-dimensional detachment model demonstrated that detachment from a trailing edge of an aircraft wing is a second order effect, having very little impact on the ultimate ice accretion.
- Application of the three-dimensional detachment model on a turbofan blade demonstrated that droplets detach before arriving at a trailing edge, with trailing edge detachment amount to a negligible effect on the ultimate impingement and ice accretion.

- The detachment and splashing and bouncing approaches have provided additional tools to investigate the effects of SLD in the “Appendix O” regime defined by the FAA for certification.

To provide the appropriate context for the development of the proposed models, a summary of the numerical approaches for in-flight icing is presented in Chapter II.

## Chapter II NUMERICAL APPROACHES TO IN-FLIGHT ICING

It is possible to numerically model in-flight ice accretion by several approaches, each with its own advantages and disadvantages. The first approach is to model in-flight icing in a fully unsteady coupled manner with airflow, droplet dynamics and thermodynamics being determined at each instant of time. While the potential exists for high accuracy with this approach, it is prohibitively costly [18]. This is partly due to the differing characteristic lengths and time scales between the aerodynamics, the droplets, and the ice accretion. An alternative approach that is most often used is a modular iterative method (referred to as multishot). The airflow, droplet impingement and mass of accreted ice during a specific period of time are solved for in a loosely coupled manner at each step of a multishot methodology, as shown in Figure II-1.

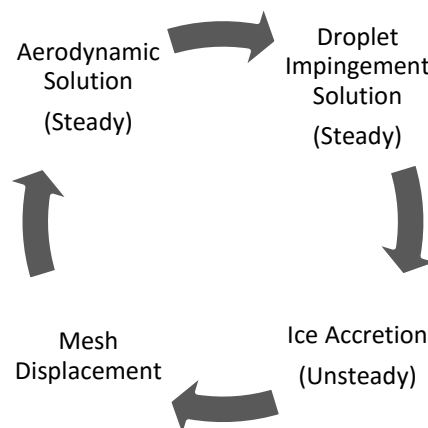


Figure II-1: Modular Approach used in FENSAP-ICE [10, 13, 17, 19-21]

Within each shot, one-way coupling is employed whereby the airflow affects the droplet dynamics and both affect ice accretion. The multishot loop is closed as the geometry and the grid are deformed to account for the ice accreted, and the following airflow solution is initiated over the new ice shape. It is also assumed in the multishot approach that the changes in the aerodynamic and droplet impingement solutions are negligible during the selected ice accretion time. The multishot methodology saves on computational cost over a fully coupled, unsteady solution, and provides a reasonably accurate prediction of ice shape and locations. The selection of the duration of each time step is a difficult problem that is based on the

atmospheric conditions that the simulation is reproducing and an examination of the rate of ice growth given those conditions. This thesis makes use of the FENSAP-ICE<sup>TM</sup> suite of software that follows the multishot approach for in-flight icing.

## **II.1 Numerical Modeling of Droplet Impingement**

A critical phase in the numerical modeling of ice accretion is droplet impingement. Approaches exist to provide very accurate modeling of individual droplets as influenced by the airflow in the form of coupled solutions. Some of these approaches include the Level Set [22, 23], Volume of Fluid [24], and other approaches to model the explicit interface between the liquid and gas phases. Alternatively, macroscopic approaches can model large numbers of droplets with a significant computational cost advantage by modeling the net force acting on the droplets due to the interaction with the airflow. In the framework of in-flight ice accretion, microscopic modeling of droplets is impractical as the cost is astronomical, whereas the macroscopic approach gives accurate solutions at a fraction of the cost.

From a numerical point of view, the macroscopic modeling of droplet flows may be solved following two approaches, namely an Eulerian or Lagrangian frame of reference. For the Lagrangian frame of reference, the frame moves with the droplets in motion, and the trajectory of a droplet may be solved for by integrating its instantaneous velocity over time. A disadvantage of the Lagrangian approach to solving droplet impingement is that, as surface geometric complexity increases, an accurate droplet simulation requires the computation of a very large number of seed locations in an attempt to appropriately define the impingement limits. This is further complicated by three-dimensional effects as the goal of defining the inlet seed limits is influenced by cross-flow, vortices, and turbulent effects. When it comes to the computation of local mass flux or collection efficiency, the Lagrangian approach makes use of the inlet seed limits (limits where seeded droplets impinge on geometry) to determine the impinging mass flux as compared to the inlet mass flux, which is difficult to extend into three-dimensions [25, 26].

In the Eulerian formulation, droplets are treated as a continuum that yields a set of partial differential equations representing continuity, momentum, and energy of the dispersed droplet

phase. Hence, the local volume fraction of droplets and the velocity of droplets may be computed at the same nodal locations as the air solution, which avoids the computationally expensive and interpolation based particle tracking process of a Lagrangian formulation [10, 25].

While the Eulerian formulation is computationally elegant, the Lagrangian formulation is capable of easily describing the interaction of droplet-wall processes for SLD and is the closest description of experimental studies. Droplets location and velocity are determined in time throughout the domain until a solid boundary is encountered, at which time semi-empirical correlations may be used to provide the conditions for deposition and rebound and subsequent tracking of further re-injected droplets. As the notion of an individual droplet does not exist in the Eulerian reference frame, it is difficult to conceive the mathematical description of what is occurring during a droplet-wall interaction and to appropriately model it. A detailed derivation of the equations governing droplet motion in an Eulerian reference is outside the scope of this thesis and the author refers the interested reader to the work of Honsek [10] or Bourgault [25] for their detailed presentation of the partial differential equations governing droplet impingement in an Eulerian frame of reference. Final equations with relevant details will be presented below to provide a basis for the proposed approach.

## **II.2 PDEs Governing Droplet Impingement in an Eulerian Frame of Reference**

There are many assumptions preceding the derivation of the PDEs governing droplet impingement in an Eulerian framework with some of the more significant ones being:

- Droplets form a dispersed yet continuous medium
- Droplet-droplet interactions (such as collisions and coalescence) are negligible
- Solid boundaries are modeled as outflow boundaries (droplet-wall interaction in the form of splashing is ignored)
- Heat and mass are not exchanged between the gas and liquid phase
- Aerodynamic shear and other effects do not have an effect on the droplet surface properties

Neglecting droplet-droplet interactions is justifiable in the computational domain. In the region of a solid boundary, however, neglecting droplet-wall interaction, especially in the SLD regime, is not appropriate and must be accounted for in some manner. The non-dimensional continuity equation governing droplet impingement in an Eulerian framework, recast in terms of liquid water content (LWC) is [10, 20, 25]:

$$\frac{\partial \alpha}{\partial t} + \bar{u}_d \cdot \nabla \alpha + \nabla \cdot \bar{u}_d = 0 \quad (\text{II.1})$$

where  $\alpha$  is the natural log of the non-dimensional local volume fraction of the liquid to gas phase and  $\bar{u}_d$  is the velocity of the liquid phase. Based on the assumptions above, droplets are subjected to aerodynamic drag, gravity, and buoyancy forces. The non-dimensional, recast and simplified form of the equations governing momentum for droplet impingement are [10, 20, 25]:

$$\frac{D\bar{u}_d}{Dt} = \frac{\partial \bar{u}_d}{\partial t} + \bar{u}_d \cdot \nabla \bar{u}_d = \frac{C_D Re_d}{24K} (\bar{u}_a - \bar{u}_d) + \left(1 - \frac{\rho_a}{\rho_d}\right) \frac{\hat{g}}{Fr^2} \quad (\text{II.2})$$

$$K = \frac{\rho_d d^2 U_\infty}{18L\mu_a} \quad (\text{II.3})$$

where  $C_D$  is a drag coefficient,  $Re_d$  is a droplet Reynolds number,  $\bar{u}_a$  is the velocity of the air,  $\rho_a$  is the density of air,  $\rho_d$  is the density of the water droplets,  $\hat{g}$  is a unit gravitational vector,  $K$  is a non-dimensional droplet inertia parameter defined in equation (II.3) and  $Fr$  is the Froude number, or a ratio of the inertial to gravitational forces. In equation (II.3),  $d$  is the diameter of the droplets,  $U_\infty$  is the magnitude of the freestream velocity,  $L$  is a characteristic length of the problem and  $\mu_a$  is the viscosity of air. The continuity (II.1) and momentum (II.2) equations are spatially discretized by means of a weak-Galerkin Finite Element formulation. The droplet drag coefficient presented in (II.2) is modeled differently based on the size of the droplet. The drag acting on small droplets is modeled by the formulation presented by Durst, et al. [27]

$$C_D = \begin{cases} \frac{24}{Re_d} (1 + 0.15 Re_d^{0.687}) & Re_d \leq 1300 \\ 0.40 & Re_d > 1300 \end{cases} \quad (11.4)$$

whereas for large droplets an extended model by Cliff, et al. is adopted [28]

$$C_D = \begin{cases} (1.0 - f) C'_D + f C''_D & We_b \leq 12 \\ C'_D & We_b > 12 \end{cases} \quad (11.5)$$

with the eccentricity function  $f$  defined as a function of the breakup Weber number:

$$f = 1.0 - (1.0 + 0.07 \sqrt{We_b})^{-6} \quad (11.6)$$

$$We_b = \frac{\rho_a d U_\infty^2 |\vec{t}_a \cdot \vec{a}_1|}{\sigma} \quad (11.7)$$

$C'_D$  and  $C''_D$  are drag coefficients that relate to that of an oblate disk and a sphere, respectively. Thus, as the droplet becomes more and more non-spherical, the drag coefficient tends towards that of an oblate disk as the shape changes also in direction. This extension of the drag model into the SLD range is important to accurately model the aerodynamic forces to which the droplets are subjected. Droplet breakup is modeled by making use of the correlations of Pilch and Erdman [29].

A non-dimensional parameter that is useful in the modeling of ice accretion is the local collection efficiency  $\beta$ , as it quantifies the potential for accretion at a given location. It represents the normalized influx of water at a solid boundary whose surface normal ( $\hat{n}$ ) points into the computational domain:

$$\beta = \left( \frac{\dot{m}_d}{A} \right) / \left( \frac{\dot{m}_d}{A} \right)_\infty = \frac{u'_n LWC}{U_\infty LWC_\infty} = - \frac{(\vec{u}'_d \cdot \hat{n}) \Lambda' \rho_d}{U_\infty \Lambda'_\infty \rho_d} = - \left( \frac{\vec{u}'_d \cdot \hat{n}}{U_\infty} \right) \frac{\Lambda'}{\Lambda'_\infty} \quad (11.8)$$

where  $\Lambda$  is a non-dimensional volume fraction of the liquid to gas phases. Simply, the collection efficiency – also known as catch efficiency or percent impingement – is a measure of the quantity of impinging liquid as compared to that in the free-stream. It is defined locally as the impinging mass flux, non-dimensionalized by the free-stream mass flux. Equation (11.8) can

be recast using non-dimensional parameters, as was used for (II.1) and (II.2) above, in terms of the droplet volume fraction  $\alpha$  and droplet velocity  $\vec{v}_d$  [20, 25]:

$$\beta = -\alpha \bar{u}_d \cdot \hat{n} \quad (II.9)$$

For accurate ice accretion in SLD conditions, droplet impingement must be accurate in terms of collection efficiency and droplet velocity as both participate in the equations governing ice growth. A review of models available in the literature for describing the droplet-wall interaction is presented in III.1.

### II.3 Numerical Treatment of Surface Films and Runback

Within the multishot approach presented in Chapter II above, the ice accretion module handles surface films and runback. Both a solid, liquid and gas (dispersed) phase of water are present in the vicinity of the solid surface, requiring careful treatment of the energy transfer to determine the rate of ice growth and liquid runback. Several models exist to account for surface films and runback with the Shallow Water Icing Model (SWIM) being a popular approach [20]. Conservation principles are applied to energy and mass transfer within a control volume as seen in Figure II-2. The film is assumed to be shallow, allowing the approximation in a linear gradient of the film velocity based on the wall shear stress [20].

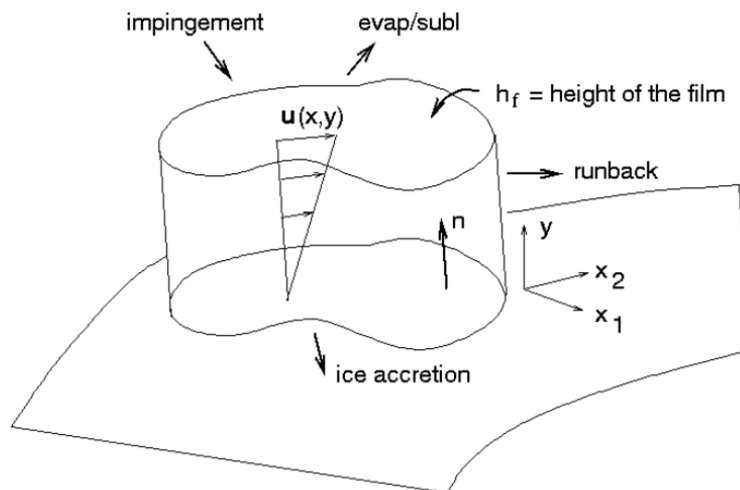


Figure II-2: A summary of the mass and energy transfer for a control volume in the ICE3D framework from [30].

Within the standard ICE3D formulation, no mechanism exists to account for the possibility of film detachment and subsequent droplet impingement.

#### II.4 PDEs Governing Runback

While the full derivation of the PDEs governing ice accretion and film runback is beyond the scope of this thesis, an interested reader is referred to the work of Bourgault [20] for details involving their derivation. The final form of the PDEs will be presented only for clarity as a part of the approach for modeling droplet detachment.

$$\rho_f \left[ \frac{\partial h_f}{\partial t} + \bar{\nabla} \cdot (\bar{V}_f h_f) \right] = V_\infty LWC \beta - \dot{m}_{evap} - \dot{m}_{ice} \quad (II.10)$$

$$\rho_f \left[ \frac{\partial h_f c_f \tilde{T}_f}{\partial t} + \bar{\nabla} \cdot (\bar{V}_f h_f c_f \tilde{T}_f) \right] = \left[ c_f (\tilde{T}_\infty - \tilde{T}_f) + \frac{\|\bar{V}_d\|^2}{2} \right] V_\infty LWC \beta - L_{evap} \dot{m}_{evap} \\ + (L_{fusion} - c_s \tilde{T}) \dot{m}_{ice} + \sigma \varepsilon (T_\infty^4 - T_f^4) - c_h (\tilde{T}_f - \tilde{T}_{ice,rec}) \quad (II.11)$$

In equation (II.10), the right hand side terms reflect the mass flux due to impingement, evaporation and change of state to ice within the control volume respectively. The terms on the left hand side solve for the height and momentum of the film as a part of the conservation of the mass. Equation (II.11) expresses the conservation of energy.  $\rho_f$  is the density of the fluid,  $c_f$  is the specific heat of the fluid,  $c_s$  is the specific heat of the solid ice,  $\sigma$  is the surface tension,  $\varepsilon$  is the surface emissivity,  $L_{evap}$  is the latent heat of evaporation,  $L_{fusion}$  is the latent heat of fusion,  $T$  is the temperature either asymptotically or locally,  $\tilde{T}_{ice,rec}$  is the ice recovery temperature which introduces the energy lost due to friction, and  $\bar{V}_d$  is the velocity of the droplets upon impingement. In this context, the  $\sim$  on the temperature denote the temperature in Celsius with all other temperatures in Kelvin.

Additional compatibility relations are needed to close the system of equations and they are summarized in (II.12) - (II.15)

$$h_f \geq 0 \quad (II.12)$$

$$\dot{m} \quad (II.13)$$

$$h_f \tilde{T}_f \quad (II.14)$$

$$\dot{m} \quad (II.15)$$

where  $h_f$  is the height of the film,  $\dot{m}$  is the mass flux of the ice and  $\tilde{T}_f$  is the temperature of the film in Celsius. These compatibility relations ensure that the film height is always positive, that the liquid is freezing into water instead of melting and assume that freezing occurs at  $0^\circ\text{C}$  with film at or above that temperature and ice at or below. While this formulation allows for the calculation of film and runback, it is unable to account for the departure due to droplet detachment.

A literature review is presented in Chapter III for both splashing and bouncing approaches as well as detachment models. Following that, proposed approaches for computing splashing and bouncing effects, along with test cases, are presented in Chapter IV. Chapter V presents a two-dimensional and a three-dimensional detachment model with validation of the latter. Test cases, using the detachment model are also presented. Chapter VI presents the results of the combined effect of both splashing and bouncing and detachment on an isolated rotor in hover.

## Chapter III LITERATURE REVIEW

As current Eulerian formulations do not directly account for droplet rebounding, a method is sought to account for the effect of droplet re-injection into the flow after rebound. To the best knowledge of the author, the approaches proposed by Honsek [10] and by the author in a two-dimensional context [31, 32] are the only fully Eulerian approaches for modeling droplet-wall interaction in the context of SLD. The approach proposed by the author decouples the pre- and post-impact simulations but suffers from a dramatic increase in computational cost. Additionally, a review of droplet detachment models is presented in III.3.

### III.1 Droplet-Wall Interactions Approaches

Several approaches have been presented in the literature to model the interaction of droplets impingement with walls for splashing/bouncing situations. The effect of splashing and bouncing is often modeled as a “local” phenomenon where the mass that rebounds has no effect on any other location. This approach is a post-processing method that simply removes mass from the collection efficiency in the splashing/bouncing region. Recently, alternative approaches were proposed in the Lagrangian reference frame by Wright, *et al.* [14, 16] and in the Eulerian reference frame by Honsek and Habashi [13]. All current approaches make use of droplet-wall interaction models to determine the amount of mass that is predicted to splash or bounce. The earliest models were typically fitted to an experimental database, such as the one proposed by Bai and Gosman [33], which provided a threshold for the onset of droplet rebound based on the properties of the impinging droplets and surface conditions. This threshold is in the form of a critical Weber number that is based on the Laplace number to a power, and a coefficient that is computed from the surface roughness. The critical Weber number, as seen in equation (III.1), proposed by Bai and Gosman is a measure of the ratio of the surface roughness as balanced by the viscous and surface tension forces. The Laplace number is a measure of the ratio of the surface tension to viscous forces. When the computed value of the droplet surface Weber ( $We_s$ ) number falls below the critical value, the inertia of the droplet is believed to be sufficient for the droplet to rebound [10].

$$We_s = A(r)La^{-0.18} < We_{s,c} = 5 \quad (III.1)$$

where  $A(r)$  is a roughness dependent coefficient and  $La$  is the Laplace number. Later, Mundo and Tropea sought to include not only the surface tension and inertia of the droplet in the threshold for splashing/bouncing but also viscous forces. For their threshold, they defined the Cossali parameter – a non-dimensional number that combines the Weber and Reynolds numbers to account for surface tension, inertial and viscous forces [10, 34-36] – though the range of their experiments was limited, resulting in limited applicability. Trujillo and Lee [37] proposed a method that builds upon the models and experimental data of Bai and Gosman [33], Mundo and Tropea [34-36], and Stow and Hadfield [38], to define a threshold based on the film thickness, surface roughness, and impinging droplet characteristics. This results in a purely empirical expression for a critical Cossali parameter for impact on a dry surface. They then recast a similar parameter as stated by Yarin and Weiss [39] to allow for a mathematical relationship for a critical Cossali number at the onset of splashing. Trujillo and Lee [37] assumed this threshold to be valid over the range of surface roughness and velocities encountered by engine manifolds during cold start, which have similar characteristics to those of airfoil and control surfaces [10].

Other models have been proposed and are summarized in great detail in [40], along with another more recent post-processing model proposed by Technische Universität Darmstadt (TUD) [41, 42]. Of interest in all the post-processing approaches is that they are all tuned to specific experimental data and discrepancies have been shown when attempting to match other experimental databases. There also appears to be additional physical phenomena, such as the effect of inflow turbulence, the effect of model scaling, and the effect of the measuring system, that are not currently understood in the experimental icing tunnels [43], though additional research is being conducted to improve the fundamental understanding of droplet impingement and ice accretion.

Recently, a slightly different approach was proposed by Jung and Kim [44] to account for the effect of splashing and bouncing in an Eulerian framework. It makes use of the model of Bai and Gosman [33], but modifies the equation for the local liquid water content (LWC) on the wall by the mass-loss ratio from Bai and Gosman. This has the same effect as post-processing the

impingement solution, as the additional equation is only loosely coupled to the continuity and momentum equations.

Once a droplet has been determined to splash, bounce, or detach, the problem of numerically modeling the re-injected mass becomes the next important step in determining the potential for re-impingement and/or secondary wetted regions. The approach proposed by Wright and Potapczuk [15, 16, 26] makes use of the Lagrangian framework to model both pre- and post-impact droplets based on a droplet-wall interaction criterion. They assume that all droplets are independent and, as such, droplets on primary trajectory do not interact with droplets rebounded off the surface. As droplets arrive at the surface, a droplet-wall model is used to determine if the droplet splashes or bounces and if so, what mass, diameter and initial vector is to be re-injected. Post-impact droplets are seeded from the surface and tracked [14]. When splashing is predicted, droplet fragmentation is neglected and a single 'representative' droplet is seeded into the flow. Wright and Potapczuk also modified the model of Trujillo and Lee [37] to introduce an impinging angular dependence into the threshold which was fitted to the experimental data of Papadakis [9, 45]. At present, the experimental database of Papadakis is the most complete data for collection efficiencies (the non-dimensional impinging mass flux on the surface) for Appendix C or Appendix O conditions.

A different, more rigorous approach, was presented by Honsek and Habashi [10, 13] in the Eulerian framework by introducing a repelling body force term into the droplet momentum equations in the vicinity of the surface. This force, defined by the droplet-wall interaction model selected, is based on the change of momentum introduced by the translation of the rebounded mass following impingement. While accounting for the effect of splashing and bouncing, it is not possible to distinguish between primary impingement and mass being re-injected from the surface, limiting this approach to only handle splashing and bouncing. Additionally, the force term introduced on the surface introduces a systemic bias whereby the locations on the surface which have already experienced impingement act to repel possible secondary impingement.

An approach was recently formulated in two dimensions [46, 47] making use of the Eulerian framework with the pre- and post-impact droplets being modeled without interaction. In the approach, discrete locations on a surface have their boundary conditions altered from a free boundary (wall) to a Dirichlet boundary (inflow). As locations cannot simultaneously have two boundary conditions, the specification of an inflow boundary precludes impingement from other locations, necessitating that each location to be computed as a separate impingement solution. The approach was set up to allow the explicit tracking of liquid mass, injected from a surface location back into the free-stream, and the combination with the primary droplet impingement solutions. While costly in two dimensions, it is predicted to be prohibitively costly in three dimensions. As a result of this high cost, it is unlikely to be of benefit during the design of an aircraft or of the Ice Protection System. In three dimensions, it may be possible to determine locations that can be simultaneously re-injected without precluding the potential for re-impingement, thus allowing for conservation of mass and momentum while reducing the cost of the two-dimensional approach [47]. This is sought through statistical clustering of the boundary conditions for the inlet of the secondary droplet solutions, while preventing or minimizing the introduced systemic bias. As a result, means to reduce the computational cost as a new approach is proposed in three-dimensions are reviewed in Section III.2.

### **III.2 Clustering Approaches & Stopping Criteria**

The problem of identifying clusters in a dataset falls into the category of pattern recognition. Many approaches can be found in the literature to compute clusters within a dataset, such as hierarchical clustering [3, 48], k-means clustering [49], distributions model [50], etc. Agglomerative hierarchical clustering begins with all data sets as clusters of one. Then, they are linked together iteratively using some distance/similarity function and the linked groups form new clusters. This is repeated until some criterion is met to indicate that the clustering has finished. K-means clustering prescribes a set number of clusters,  $K$ , and then defines centroids for each cluster such that the overall error/dissimilarity is minimized over all the data sets. With an unknown number of clusters, k-means clustering must be applied iteratively to test the alteration in the global error/dissimilarity given a set number of clusters,  $K$ .

The issue of the unknown number of clusters contained within a dataset has been extensively studied in the literature, resulting in the introduction of a large number of ‘stopping’ criteria [1-3, 51]. A stopping criterion is a mathematical relationship, threshold or method, which examines certain changes within the clusters of the data. For example, some stopping criteria examine the change in the error contained within a cluster while others examine the compactness of the clusters. The purpose of a stopping criterion is to determine the natural number of clusters in a data set. When searching for natural groupings in datasets, there are many different problem classes that produce different types of data, resulting in great variation between the datasets. For example, some stopping criterion were proposed for the statistical analysis of document retrieval from search results [52], and other stopping criteria for the study of inter-organizational relationships [53]. Some of the stopping criteria proposed in the literature function well only for the dataset for which they were developed [51]. These criteria are either global, in that the quantity examined is defined as a summation across all clusters, or local, in that the quantity examined is only computed for the cluster under consideration. Milligan and Cooper [51] reviewed over 30 different stopping criteria on the basis of their generality (the ability of the criteria to be applied to datasets to which they were not originally linked) and accuracy (the ability to determine the correct number of clusters contained within the dataset). They concluded that the Variance Ratio Criterion [2] (VRC) proposed by Calinski and Harabasz, the  $J_e(2)/J_e(1)$  [1] criterion proposed by Duda and Hart, and the C-Index [3] criterion by Hubert and Levin, were the most general and accurate. These three criteria will be reviewed in Sections III.2.1 through III.2.3 below.

Out of the hundreds of randomly generated datasets that Milligan and Cooper [51] used in 4-, 6-, and 8- dimensional Euclidian spaces containing between 2 and 5 natural clusters, the VRC and  $J_e(2)/J_e(1)$  correctly identified and assigned the data to the appropriate clusters more than 90% of the time. The C-Index correctly identified and assigned the data about 80% of the time. The other criteria proved to be less accurate when used on datasets that they were not designed to match. For brevity, only the best criteria, or those that are most general and

accurate, are reviewed herein and the interested reader is recommended to the work of Milligan and Cooper [51].

### III.2.1 Variance Ratio Criterion

The Variance Ratio Criterion (VRC) [2] proposed by Calinski and Harabasz examines a ‘global’ change in the Variance Ratio as defined in (III.2). In equation (III.2),  $BCSS$  is defined as the between cluster sum of squared distance/error,  $k$  is the number of clusters,  $n$  is the number of discrete data sets, and  $WCSS$  is the sum of the within cluster sum of squared distance/error. To implement the VRC within the context of hierarchical clustering, all discrete data sets are linked into a single cluster. They are then divided according to the reverse order of their linking with the change in the VRC being examined during this division. When the VRC reaches a local maximum, the division stops and the natural number of clusters has been determined.

$$VRC = \left( \frac{BCSS}{k-1} \right) / \left( \frac{WCSS}{n-k} \right) \quad (III.2)$$

### III.2.2 The Sum of Squared Error $J_e$

The  $J_e(2)/J_e(1)$  criterion is a ‘local’ criterion since it examines the change in the sum of squared error as a single cluster is divided into 2 clusters. The  $J_e(2)/J_e(1)$  criterion begins with the assumption that a single cluster is better than two clusters. The hypothesis is rejected only if [1, 51]:

$$\frac{J_e(2)}{J_e(1)} < 1 - \frac{2}{\pi d_c} - \zeta \sqrt{\frac{2(1-8/d_c \pi^2)}{n d_c}} \quad (III.3)$$

$$J_e(m) = \sum_{i=1}^m \sum_{s \in \chi_i} (s - \bar{\mu}_i)^2 \quad (III.4)$$

where  $d_c$  is the dimensionality of the distance/dissimilarity metric,  $\zeta$  is the z-score computed from the percentile confidence level,  $n$  is the number of datasets in the cluster,  $s$  is an individual data point,  $\bar{\mu}_i$  is the mean of the samples in the  $\chi_i$  cluster, and  $m$  is either a 1 or 2

to compute either  $J_e(1)$  or  $J_e(2)$ . As in the VRC, within the context of hierarchical clustering, all discrete data sets are linked into a single cluster. They are then divided according to the reverse order of their linking but instead of applying the criteria to the global change, each resultant cluster is examined and individual clusters may continue to be divided.

### III.2.3 C-Index

The C-index, from Hubert and Levin [3] is again a ‘global’ criterion in that it examines the change of  $C$  as clusters are divided. In the context of equation (III.5),  $d_w$  indicates the sum of the within cluster distances/errors. The computation of  $C$  has the effect of looking at the change of the overall error/dissimilarity across all the clusters as normalized by the distribution of the error within any particular cluster.

$$C = [d_w - \min d_w] / [\max d_w - \min d_w] \quad (III.5)$$

Unlike the VRC, the C-index approach looks for a local minimum in the change of  $C$  as the clusters are divided in order to stop.

### III.3 Droplet Departure Models

In the literature, there are several droplet departure models proposed to predict the shedding or detachment of droplets from a surface [54-56]. While the terms shedding and detaching are often used interchangeably, in the strictest sense, shedding is defined as the inception of droplet motion along the surface and detachment is the removal from the surface. In these approaches, forces are balanced in normal and tangent directions. The forces to which the droplet is subjected are usually grouped into adhesion (resisting both shedding and detaching), shedding (acting in the tangential direction) and detaching forces (acting in the normal direction). According to Zhang, *et al.* [4], if the Bond number is below about 0.06, the effect of the gravitational and buoyancy forces are negligible. The Bond number (or Eötvös number) characterizes the relative strength of the net buoyancy to surface tension forces. For values lower than 0.06, it is safe to assume little significance from the inclusion of these two body forces.

An understanding of shape of the liquid mass at a location is important in the modeling of the detachment forces. According to Fortin, *et al.*, [57] liquid runback on an airfoil may exist as either a film, rivulets or beads (discrete droplets) as seen in Figure III-1. If this liquid arrives at a geometric corner in the form of a film, it may be more suitable to model the detachment based on the concepts of Mansour and Chigier [58] in their work on sheet breakup (see Section III.3.2). In the case of rivulets or beads, an isolated droplet model (see Section III.3.3) as in the cases of Chen, *et al.* [55], Kumbar, *et al.* [56], and Zhang, *et al.* [4] or a model based on the concept of Jet Pinch-off (see Section III.3.1) may be more suitable.

The transition between a continuous film, rivulets and isolated droplets on a surface is governed by a complex interaction of forces acting on the free surface of the liquid. The shape of the liquid, whether film, rivulet or droplet, is governed by the minimization of surface energy [59-61]. A review of Jet Pinch-off, Sheet Breakoff and Isolated Droplet departures models is found below.

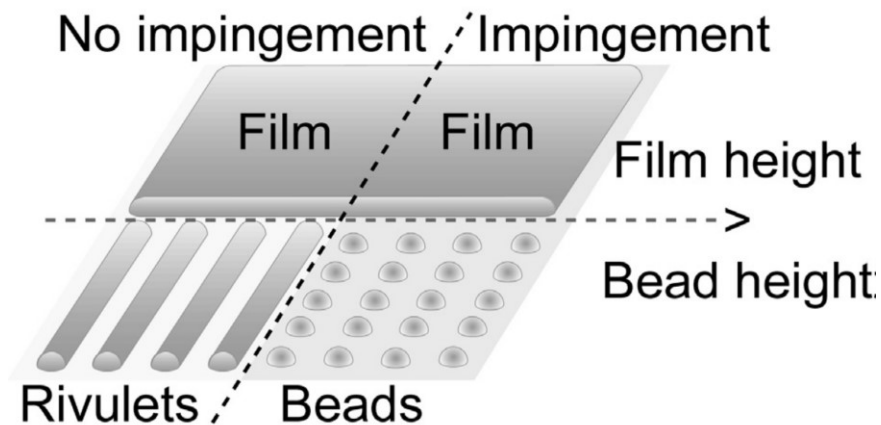


Figure III-1: Types of surface runback during the icing process from Fortin, *et al.* [57]

### III.3.1 Jet Pinch-off

Lasheras, *et al.* [62] studied jet pinch-off in the presence of a co-flowing gas. They used a co-flowing nozzle, as seen in Figure III-2, to generate jets with a variety of velocities. By altering the velocity, the breakup length and droplet sizes could be manipulated, though only at a distance downstream of the nozzle. In the region near the nozzle, the jet remained cohesive for a length,

and then began to break up into a mixture of very large droplets (with diameters greater than the jet diameter) and smaller droplets. Following the primary breakup, additional breakup occurs with a mixture of smaller droplets and a significantly reduced ratio of larger droplets existing as the liquid is transported downstream.

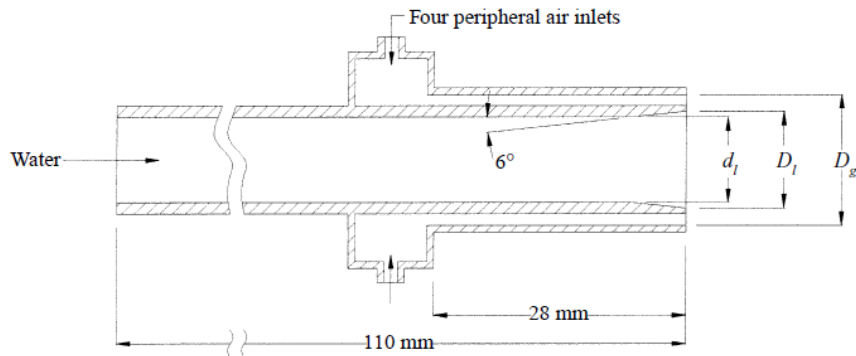


Figure III-2: Apparatus used by Lasheras, *et al.* [62] to study jet pinch-off in the presence of a co-flowing gas

### III.3.2 Sheet Breakoff

Mansour and Chigier [58] performed experiments where a two-dimensional sheet of liquid was surrounded by co-flowing air as seen in Figure III-3. Their generated sheets varied in thickness and they tested various relative velocities between the air and liquid.

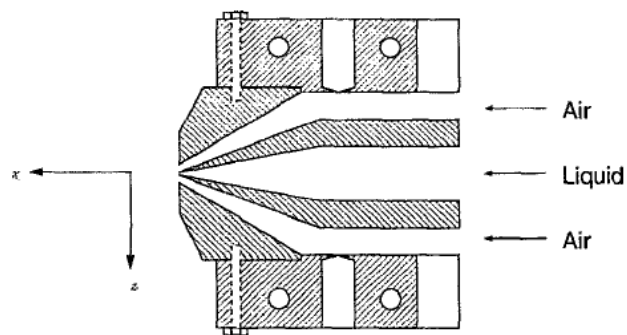


Figure III-3: Two-dimensional view of the sheet generator in the experiments of Mansour and Chigier [58]

As a result of their experimental work, they developed correlations for the breakup length of the sheet, or the length the sheet remains cohesive, based on the velocity of the fluid and the pressure in the air nozzles. In the situation of water detachment from a trailing edge during runback, the liquid accumulation as a sheet could be modeled with a breakup length as it flows

past the end of the surface. The experiments lack detail into the size of the droplets upon breakup though the authors present some images showing the breakup of the sheet into large and small droplets followed by secondary breakup of the large droplets into smaller droplets.

### III.3.3 Isolated Droplet

Other models or experiments in the literature model an isolated droplet on a surface. In these cases, the forces acting on the droplet are modeled using approaches that differ in the assumed shape of the droplet, the shape of the contact line, and the variation of the contact angle. Assuming the forces acting on an isolated droplet are 'small' enough, a circular cross-section can be assumed. Once the forces become 'large', the assumption of a circular cross-section introduces additional errors, as in reality deformation will occur. It is also possible that break-off, or the phenomena whereby some of the liquid droplet is entrained in the airstream, may occur if the shearing forces become great enough [63, 64].

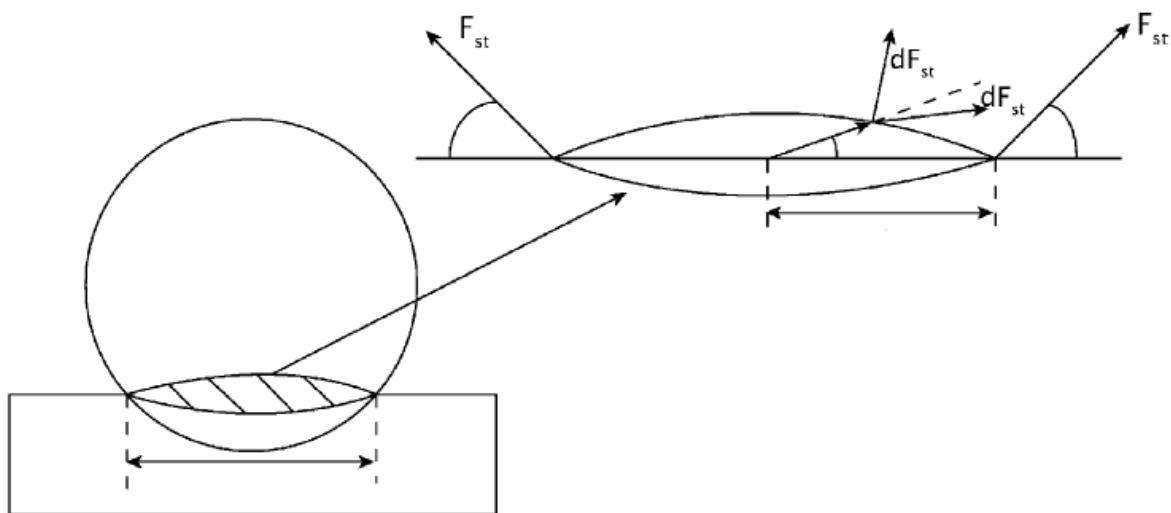


Figure III-4: Surface tension force on a spherical cap shape from Kumbur, *et al.* [56]

The surface tension force acts along the contact line and in the direction of the local contact angle as shown in Figure III-4. The shear and pressure forces act over the shape of the droplet and components act in the normal and tangential directions. Hence, the ultimate expressions for the forces acting for detachment modeling are based on the shape of the liquid surface, the

shape of the contact line, and the variation of contact angle along the contact line. Schillberg and Kandlikar [54] review different detachment models based on the assumed droplet shapes and profiles. These models are primarily for channel flow conditions with the droplet on a flat surface. Some of the assumed shapes are spherical, spherical caps, and cylindrical shapes. Other droplet models assume [65] a non-circular, non-symmetric contact line and a non-spherical shape. Despite their differing assumptions, many make use of simplified expressions for the drag force (combined shear and pressure), based on the work of Goldman, *et al.* [66]. Goldman solved the Stokes equations for a neutrally buoyant sphere of water in the vicinity of a solid surface and provided an asymptotic coefficient for the value of the drag force of a sphere in contact with a surface at small particle Reynolds numbers [67]. Chen, *et al.* [55] and Kumbar, *et al.* [56] assume that the drag can be computed from simple conditions before and after the droplet and applied to either the frontal area or an area derived from the droplet dimensions. Chen, *et al.* [55] compute the surface tension force as a simple product of values, whereas Kumbar, *et al.* [56] integrate the surface tension force, assuming a linear variation, around a circular contact line. Zhang, *et al.* [4] make use of drag force correlations from the literature and, like Chen, *et al.* [55], compute the surface tension force from the advancing and receding contact angles. Unlike Chen, Zhang, *et al.* [4] provide a corrective coefficient to the drag which they suggest would have to be determined experimentally for each surface-liquid pair.

Building on the open literature, an approach is proposed in Chapter IV to account for SLD splashing and bouncing in an Eulerian framework at a reduced cost. This approach introduces pattern recognition in the form of clustering to reduce the number of secondary simulations that must be computed to determine the effect of the secondary droplets.

## Chapter IV NUMERICAL MODELING OF SPLASHING AND BOUNCING: THE CLUSTERED APPROACH

The proposed Eulerian approach for SLD re-injection and re-impingement (later referred to as the non-clustered approach) proposed previously [31] is summarized here for completeness. A first fundamental assumption is that any interaction between rebounding droplets and incoming particles will be neglected. Thus, the pre- and post-impact droplets dynamics are decoupled. The simulation of droplet impingement with splashing, bouncing and re-injection in a *mass-conservative* Eulerian framework can be described as follows:

- i. The incident droplet impingement locations and mass caught are computed in the Eulerian framework [25]
- ii. The primary impingement solution is post-processed using a droplet/wall interaction model to determine the mass of water to be removed due to splashing/bouncing, as well as the diameter, angle, velocity and concentration of the droplets to be re-injected
- iii. The droplets in the splashing/bouncing regions are re-injected
- iv. The overall collection efficiency is the sum of the post-processed and corresponding re-injected droplet solutions

Additionally, if the momentum that is lost due to the collision of the droplets with the surface is included with that of the pre- and post-impact droplets flows, momentum is conserved. In the non-clustered approach, each surface facet is treated independently from the other surface facets since re-injected water could re-impinge on neighboring re-injection sites. A facet can be a re-injection site or an impingement boundary, but not both simultaneously. The methodology outlined above results in the conversion of surface facets in the primary impingement region (exit boundary condition) to inlets with initial velocity and LWC dictated by the amount of rebounding water. This causes a significant increase in computational cost.

In two-dimensions, this cost was mitigated by computing the rebound solutions only on a pertinent subset of the computational mesh, thereby reducing the number of degrees of freedom of the problem [32, 47]. This pertinent subset was defined heuristically by selecting all elements bounded by 10% of a characteristic length in the upstream direction, 50% of a characteristic length in the surface normal direction from the site of the re-injection, and the

last geometric point in the downstream direction [32, 47]. Three-dimensional flow domains are typically much more complex, increasing the difficulty of selecting an appropriate limited subset of the computational mesh. Additionally, since the relative size of splashed droplets is significantly smaller than their primaries, they are more susceptible to aerodynamic phenomena, hence this technique of limiting the computational domain is extremely difficult if not impossible to determine. With such a high cost, the effect of splashing and bouncing or the potential susceptibility of a particular design to SLD phenomena could never be explored as a part of the design phase for a new aircraft. Additionally, without some form of justification of the high computational cost, an engineer may have difficulty allocating the necessary computational resources to determine the full effect of SLD splashing and bouncing will have on their design. As a result, clustering of rebound boundary conditions is introduced as a new approach to reduce the total computational cost of the secondary droplet flows so as to provide a tool that can demonstrate potential susceptibility and justify the great expense of the non-clustered approach.

#### **IV.1 Clustering Explained**

Computational cost is mitigated by the implementation of a statistical clustering approach that groups multiple inlet facets together. Rather than compute a secondary simulation for each of the facets predicted to splash or bounce as shown in Figure IV-1, facets are grouped/clustered to limit the number of secondary computations performed. This clustering is done on the basis of similarity of inlet conditions and avoidance of re-impingement on neighboring active re-injection facets. Details regarding the evaluation of the similarity of inlet conditions and the avoidance of neighboring active re-injection facets are presented in IV.1.1 and an example of the clustering process is presented in IV.1.4. While the grouping of the re-injecting facets does not reduce the degrees of freedom of the secondary droplet flow solutions, it reduces the number of additional solutions that must be computed to provide the additional secondary re-impingement and shadow regions. With facet clustering, the *mass-conservative* Eulerian framework discussed above is altered so that facet clusters are re-injection rather than individual facets.

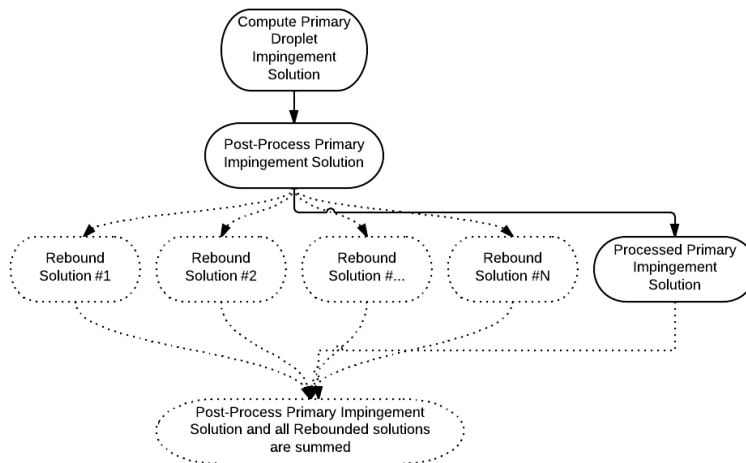


Figure IV-1: Framework to compute rebound solutions where each facet is a separate simulation.

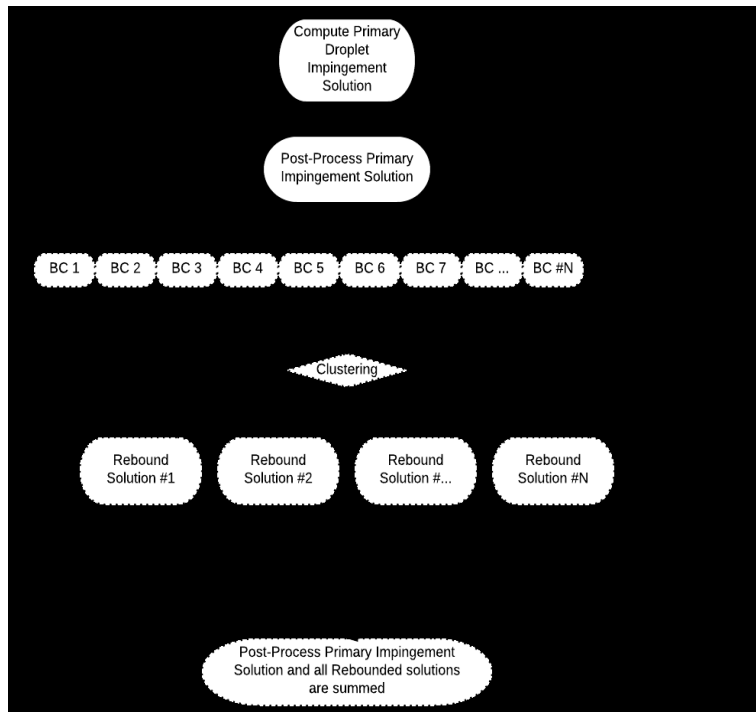


Figure IV-2: Re-injection framework for splashing and bouncing with statistical clustering introduced

The new framework is shown in Figure IV-2. Given the uncertainty of defining a-priori the most appropriate number of clusters and their associated boundary conditions (droplet diameter, inlet velocity, and LWC), hierarchical clustering [1-3, 48, 51, 68-70] appears to be the most suitable approach. Several factors contribute to the selection of hierarchical clustering, namely: it can be implemented efficiently and in a parallel manner; without knowing the number of

clusters a priori, many of the data structures to compute the clusters can be re-used during the iterative process; and that both local and global stopping criteria can be easily implemented. Individual inlet conditions (location, initial velocity, rebounded droplet diameter, rebounded LWC) are first linked using Agglomerative Hierarchical clustering using one of the linkage approaches indicated in IV.1.2. Then, once only a single cluster is present, the cluster is split using Divisive Hierarchical clustering, applying the stopping criterion to determine the natural number of clusters.

### IV.1.1 Distance Metric

As part of data clustering, a distance or dissimilarity metric must be defined to establish the relationship between individual data points, between data points and clusters, and between clusters. This is split into two problems: definition of the distance/dissimilarity between any two data points and selection of the minimum of the dissimilarity values when grouping between clusters. The latter case will be discussed in IV.1.2. To define the distance between any two data points, the following criteria are proposed:

$$E_1 = \begin{cases} \sum_{i=1}^2 |\cos(\theta_{ij})| & \theta_{ij} < \frac{\pi}{2} \\ 0 & \theta_{ij} > \frac{\pi}{2} \end{cases}; j \in (1,2), j \neq i \quad (\text{IV.1})$$

$$E_2 = \frac{|D_i - D_j|}{D} \quad (\text{IV.2})$$

$$E_3 = \left| \frac{\cos^{-1}(\hat{V}_i \cdot \hat{V}_j)}{\pi} \right| \quad (\text{IV.3})$$

where  $\theta_{ij}$  is the angle between the  $i$  inlet node re-injection velocity vector and the direction vector joining the  $i$  and  $j$  re-injection nodes,  $D$  is the diameter of the primary droplet before impingement,  $D_i$  and  $D_j$  are the diameters of the  $i$  and  $j$  re-injection droplets,  $\hat{V}_i$  is the  $i^{\text{th}}$

unit re-injection boundary vector. The final distance or error is defined as the summation of the three individual errors  $E_1$ ,  $E_2$ , and  $E_3$ .

The purpose of equation (IV.1) is to provide a first-order approximation for the probability that droplets rebounding from a surface facet  $i$  will re-impinge on surface facet  $j$  being considered for inclusion in the cluster. If a surface facet is defined as an inlet, it must not be a re-impingement site for droplets launched concurrently from another re-injection facet. While the approximation provided by equation (IV.1) cannot account for what happens to the droplets after they leave the surface, it attempts to prevent clustering of facets that are likely to cause simultaneous re-impingement on each other.

Equation (IV.2) looks at the normalized difference in the secondary droplet diameters. This has the effect of grouping facets experiencing droplet bouncing where the secondary droplet diameter is comparable to the primary droplet diameter. As the PDEs governing droplet impingement in an Eulerian framework can handle only a single diameter within any finite element, clustering by similar diameter helps to reduce the loss of information should an average diameter be used when re-injected droplets pass through the same element in the region around the geometry. Additionally, equation (IV.2) also allows for increased numerical stability as the similarity in the droplet diameter as a boundary condition allows for improved convergence rates.

In order to improve convergence and allow for a higher CFL number, equation (IV.3) is introduced to increase numerical stability. As the PDEs, discussed in II.2, governing droplet impingement are non-dimensionalized by both the freestream LWC and velocity, equation (IV.3) acts to stabilize the equations by bringing the equations close to unity.

#### **IV.1.2 Hierarchical Clustering Approaches**

To address the case of the selection of the minimum of the dissimilarity values when grouping between clusters, single linkage [48], complete linkage [69], average linkage [52], Wards Method [52], and many other possibilities exist. Single linkage links clusters based on the individual data sets best values, or the value of the distance metric being the lowest. It is fast

but may cause clusters of extremely dissimilar features to exist and often forms long chains where only the most closely linked have similar features. An example of the single linkage approach to Agglomerative Hierarchical clustering is shown in Figure IV-3. Alternatively, the complete linkage approach creates dense clusters with extremely similar features, though is computationally expensive as it requires the computation of a matrix of distances/similarities after each link is made. An example of the complete linkage approach of Agglomerative Hierarchical clustering is shown in Figure IV-4.

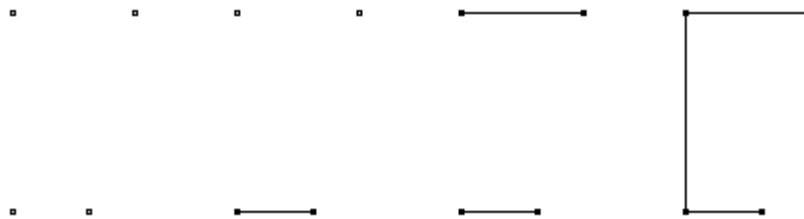


**Figure IV-3: Single linkage for a grouping of 4 points in a two-dimensional plane.**  
 Progressing from left to right, a single link is defined based on the minimum distance between points in each cluster

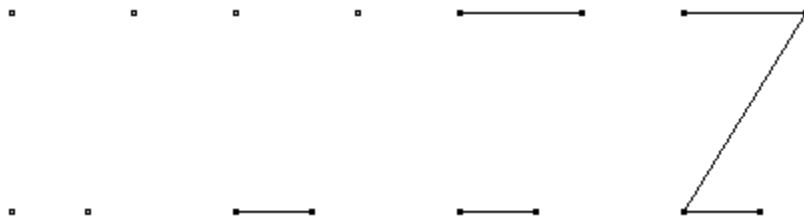


**Figure IV-4: Complete linkage for a grouping of 4 points in a two-dimensional plane.**  
 Progressing from left to right, a single link is defined based on the maximum distance between points in each cluster

Should the divisive step of Agglomerative-Divisive Hierarchical Clustering be implemented on the simple datasets of Figure IV-3 and Figure IV-4, the worst edge (or the edge added as the last linkage) would be removed first and then a stopping criterion, as discussed in III.2 above, would be applied to determine if the appropriate number of clusters had been determined.

The single linkage, complete linkage and a constrained complete linkage approach were implemented and tested with an evaluation of the change in the error contained within the clusters in time. Figure IV-5 and Figure IV-6 show the  $|L_2|$  and  $|L_\infty|$  for clustered prescribed on the Trap-wing geometry from the AIAA HiLiftPW-1. In Figure IV-5 and Figure IV-6,

Agglomerative Hierarchical clustering grouped all secondary droplet inlet boundary conditions into a single cluster. Then the division process was employed with the horizontal axis showing the number of discrete clusters during the division. As can be seen, the complete linkage offers the lowest level of error/dissimilarity of the implemented methods for the entire division process. The constrained complete linkage required that clustered inlet locations share an edge of the computational mesh that was employed but otherwise was the same as the single linkage approach.

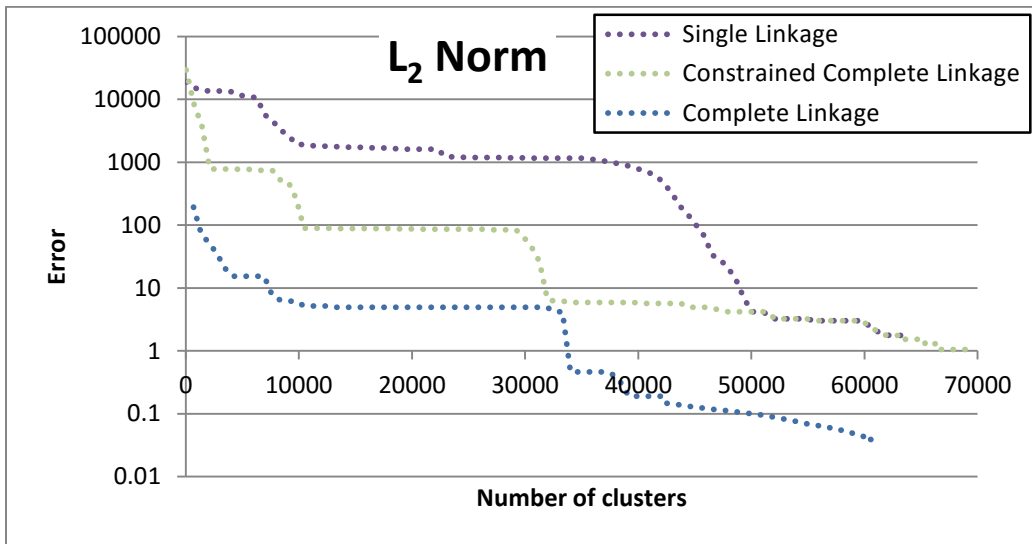


Figure IV-5:  $|L_2|$  of the error contained within the clusters employing the different linkage approaches

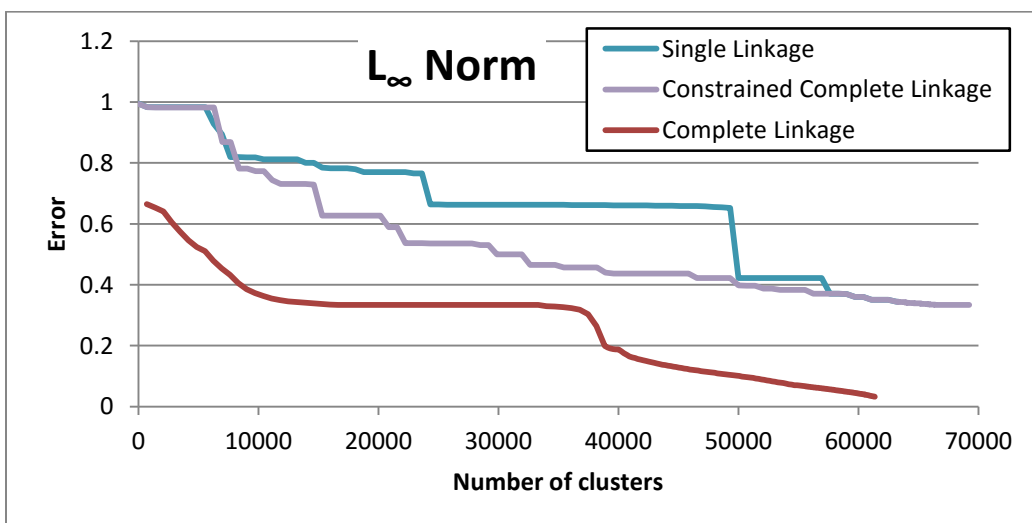


Figure IV-6:  $|L_∞|$  of the error contained within the clusters given the different linkage approaches

### IV.1.3 Stopping Criteria

The  $J_e(2)/J_e(1)$  [1] stopping criterion proposed by Duda and Hart was selected since it is one of the most general and accurate. As a local criterion, the  $J_e(2)/J_e(1)$  also brings many attractive features as it can be applied in parallel to each cluster that is formed and the quantities for the criterion can also be computed in parallel, thus allowing for optimal use of a parallel computing architecture. Hierarchical Agglomerative-Divisive Clustering was implemented using parallel techniques found in the literature [70] on a shared memory architecture and the  $J_e(2)/J_e(1)$  stopping criterion [1, 51].

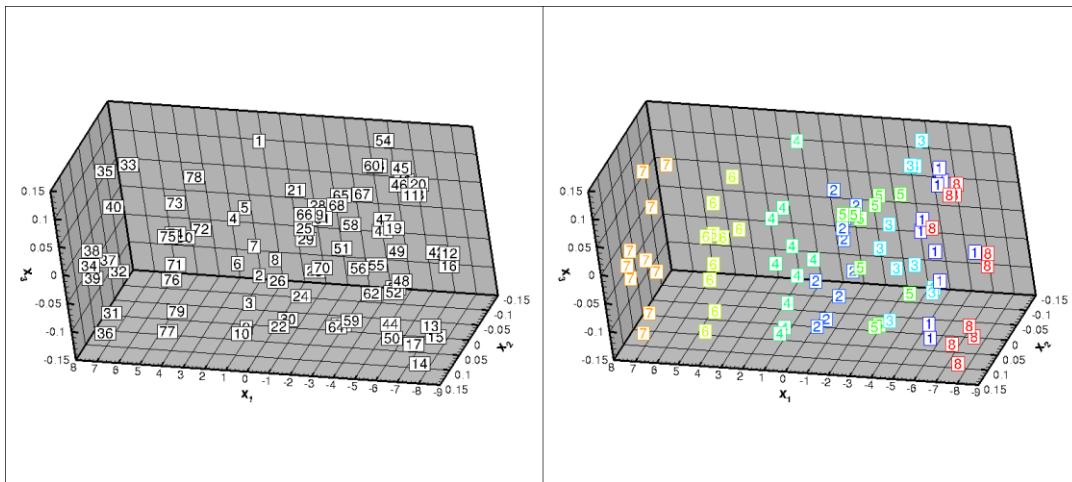


Figure IV-7: A sample dataset (left) showing the first 3 dimensions in one of the 8-dimensional spaces tested with the identified clusters (right)

Similar to the testing performed by Milligan [51], the performance of the clustering algorithm was evaluated on random datasets with a known number of clusters generating points in 4-, 6-, and 8-dimensional spaces. The distance metric used to cluster the data was a summation of the absolute Euclidian distance in each of the  $x_n$  dimensions. Figure IV-7 shows the first 3 dimensions (left) of a sample 8-dimensional space on which the clustering algorithm was tested. The right side of Figure IV-7 shows the correctly identified 8 natural clusters in the sample data.

### IV.1.4 An Example of Clustering Inlet Facets

To demonstrate the clustering, using the distance metric proposed in IV.1.1, a single diameter of a multi-diameter solution is herein presented. The geometry studied was the Trap-wing from

the AIAA HiLiftPW-1. For this example, the primary diameter selected was  $391.775 \mu\text{m}$ , the largest of the 10 discrete diameters employed by Papadakis, *et al.* [71] in their  $92 \mu\text{m}$  MVD distribution. Figure IV-8 shows the diameter contours of the predicted rebound droplets, as normalized by the primary droplet diameter. In this case, the droplet rebound model of Wright and Potapczuk [15, 16, 26, 72] was employed, giving rise to a smooth variance of predicted diameters. Visible on both the body and the main element are regions of bouncing where the rebounded diameter is approximately equal to that of the primary diameter.

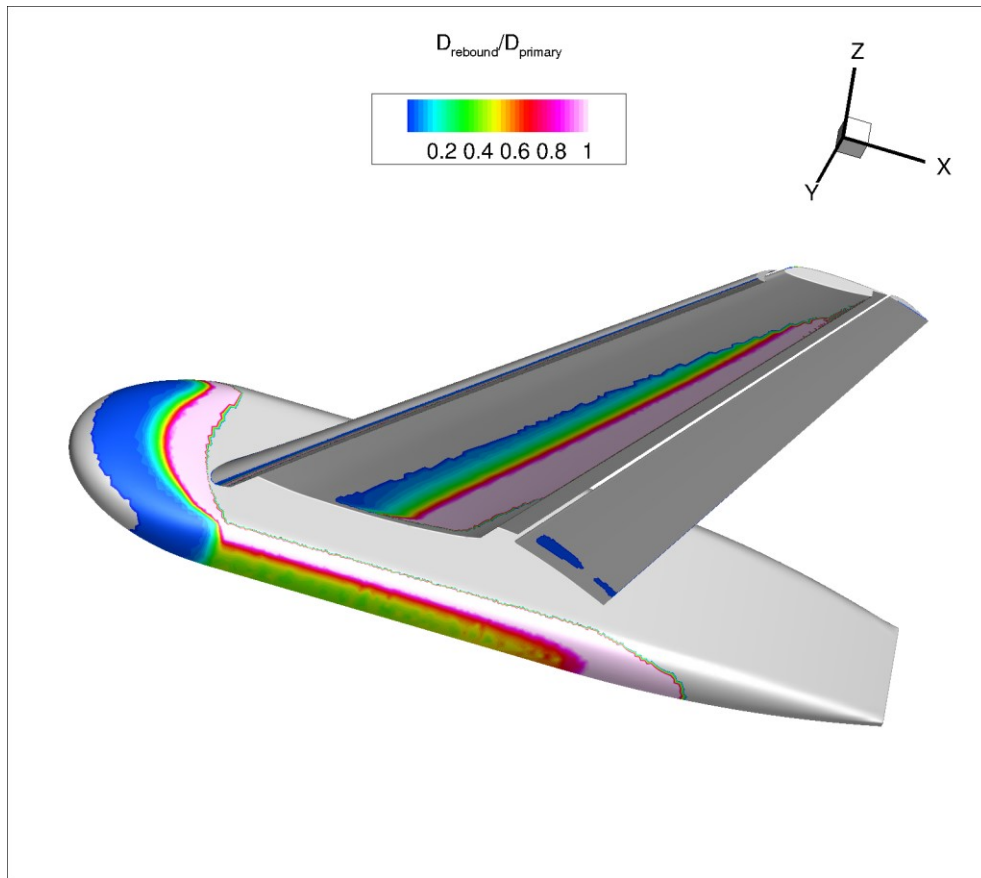


**Figure IV-8: Normalized droplet rebound diameter contours on the Trap-wing geometry.  
The primary diameter was  $391.775 \mu\text{m}$**

In Figure IV-9, the inlet velocities, as determined by the droplet rebound model, are shown. The surface contours show the magnitude of the velocity of the rebounded droplets, as normalized by the freestream velocity of  $70 \text{ m/s}$ . The three-dimensional nature of the flow may cause significant cross-flow and other effects. However, due to the large size and great momentum of these larger droplets, very little three-dimensional effect is seen. As such, the bulk of the inlet

velocity vectors lie in a series of two-dimensional planes. As the clustering approach was applied to the 30,025 discrete locations with inlet characteristics, making use of the distance metric as defined in IV.1.1 and the  $J_e(2)/J_e(1)$  stopping criterion, 6 discrete clusters were predicted. These clusters are shown in Figure IV-10. Due to the magnitude of the secondary droplets velocities and the alignment of the inlet vectors, the primary deciding factor in the clustering of these inlet conditions was predominately the droplet diameter. This resulted in clusters that closely resemble the splashing and bouncing regions of Figure IV-8. Given a much smaller inlet diameter where the three-dimensional effects of the aerodynamic flow result in more complex primary impingement, the approach presented herein predicts a greater number of clusters as discussed in IV.4 below.

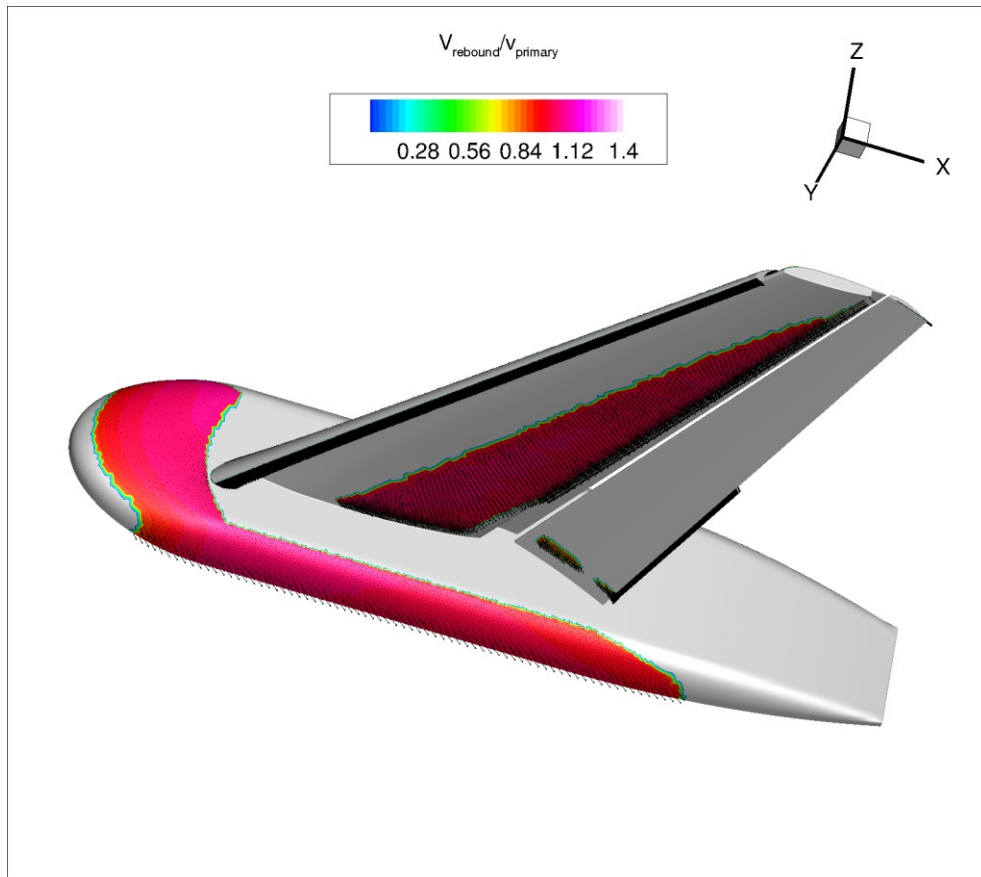


**Figure IV-9: Predicted inlet velocities for the rebounded droplets.  
Surface contours denote the normalized magnitude of the inlet velocity**

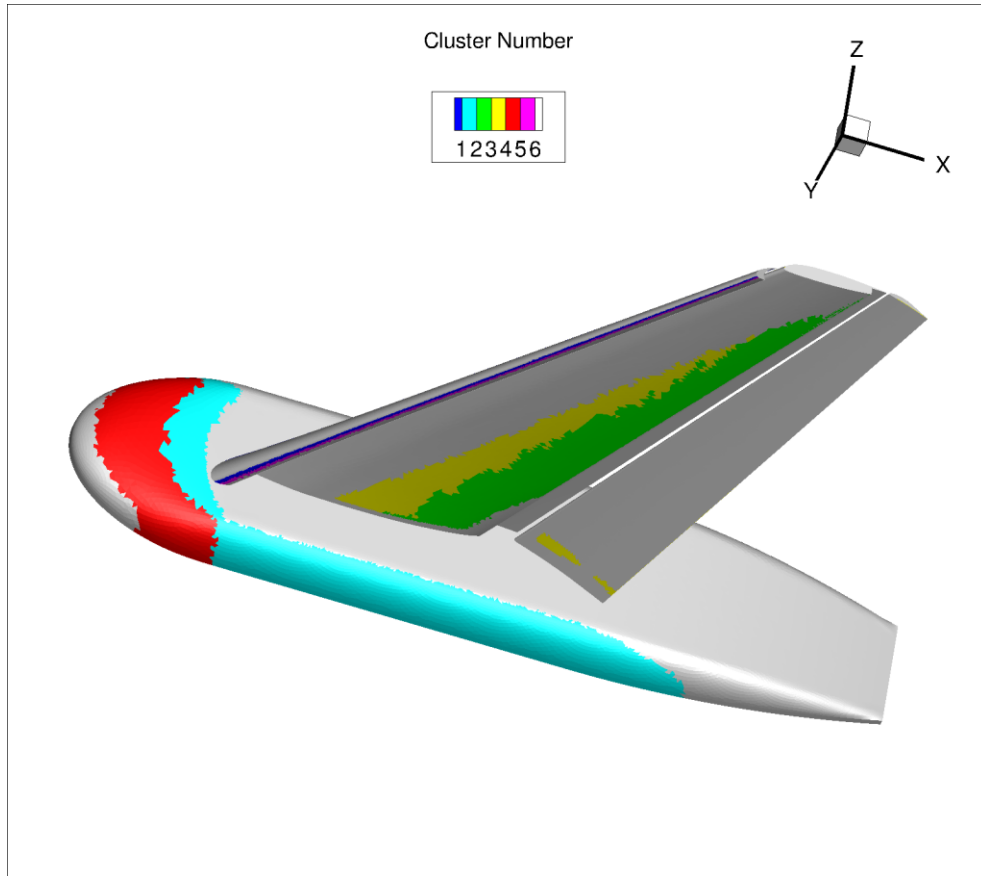


Figure IV-10: Predicted clusters for this single primary diameter

## IV.2 PDE Restrictions on Boundary Conditions

Of fundamental importance in the clustering of droplet inlet conditions is the well-posedness of the PDEs as subjected to dissimilar boundary conditions. Similar to the examination of the boundary conditions and well-posedness analysis performed by Bourgault, *et al.* in [25], an analysis was performed to assess the effect of discontinuous boundary conditions on the droplet equations. Bourgault proved the well-posedness of the continuity and momentum equations for Eulerian droplet impingement modeling for  $n$ -dimensional flow ( $n \geq 2$ ) subjected to continuous, smooth boundary conditions. The smoothness of the boundary conditions is described in the variation of the first derivatives of the applied boundary conditions of neighboring locations of the inflow region of the boundary. Each of the steps employed by Bourgault were examined to determine if non-smooth (discontinuous first derivatives), discontinuous boundary conditions would have an effect on the proof. All steps of the proof are found to be valid, even with the alteration of the assumed state of the boundary conditions.

The bulk of the steps in the Bourgault's proof of well-posedness are application of the momentum equation to an arbitrary domain  $\Omega$  and the integration of the PDE over that domain. In order to finish the proof of well-posedness, it is necessary to apply the Hölder inequality to one of the terms on the right-hand-side of the resulting inequality and then to bound the energy of the equation using Gronwall's inequality. Neither the Hölder nor Gronwall inequalities have a restriction on the continuity of the domain or the continuity of the first derivative of the boundary conditions. As such, the droplet equations are still well-posed in three-dimensions when subjected to non-smooth, discontinuous boundary conditions, as is being proposed by injecting multiple locations simultaneously. In the two-dimensional approach [47], as only a single facet had a prescribed inlet boundary condition, a well-posedness assessment was not necessary as the boundary conditions were still smooth and continuous. No restrictions are placed on the boundary conditions by the process of proving the well-posedness, and as such, the statistical approach to determine the most appropriate clustering of inflow boundary conditions is not affected by the equations themselves.

### **IV.3 Two-dimensional Test Cases**

In the literature, there is very little experimental data for the effect of splashing and bouncing. Of what data is available, most is purely two-dimensional and limited to simple geometries without interacting components. To the knowledge of the author, the work on the MacDonnell-Douglas LB606b by Papadakis, *et al.* [71] is the only experimental SLD impingement results where splashed or bounced droplets from one component may interact significantly with additional components downstream of the component.

#### **IV.3.1 Non-clustered Testing with Interacting Components**

The LB606b test case from Papadakis, *et al.* [71] was selected to examine the accuracy of the non-clustered method on complex interacting components. The parameters of the simulation are summarized in Table IV-1 with a portion of the computational mesh in the region of the geometry shown in Figure IV-11.

Parameter	Value	Parameter	Value
$V_\infty$	78.7 m/s	LWC	0.21 g/m <sup>3</sup>
$P_\infty$	95630 Pa	MVD	92 μm
$T_\infty$	276.9 K	AOA	4°
$c$	0.9144 m		

Table IV-1: Parameters from the work of Papadakis, *et al.* [71] on the LB606b test case

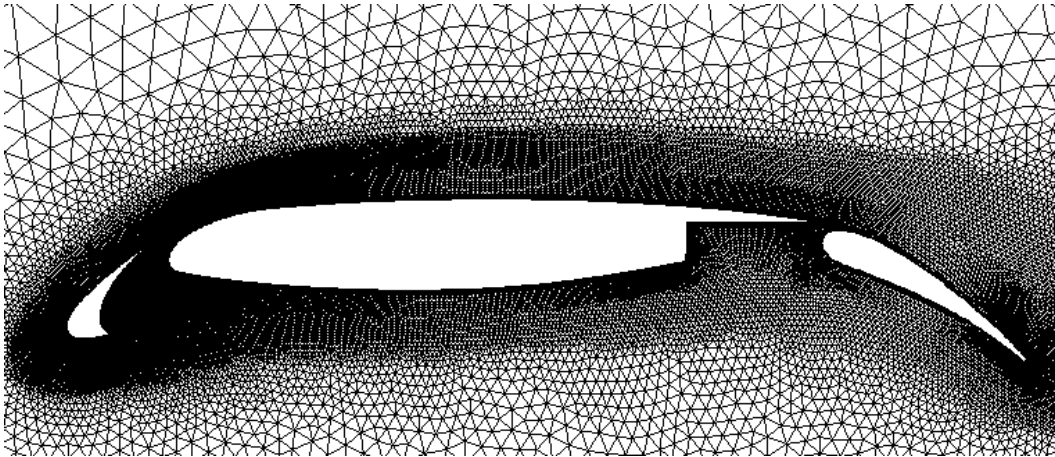


Figure IV-11: Detail of the computational mesh near the airfoil for the McDonnell Douglas LB606b. The mesh contains 235,000 nodes

Figure IV-12 shows a comparison between the experimental data and the non-clustered treatment of splashing and bouncing for the slat, main element, and flap. The agreement is very good on the slat, however very little secondary mass impinges on the slat. The bulk of the splashed or bounced droplets are carried either to the main element, the flap or leave the computational domain altogether. While the explicit tracking of splashed and bounced droplets slightly improves the collection efficiency results on the main element, a notable discrepancy is observed between CFD and experimental results. This might be the result of a combination of factors, both on the numerical and experimental side. For example, on the experimental side, the use of blotting paper to measure droplet impingement in the experiment changes the rebound/absorbency of the surface and cannot be reproduced by the numerical model. On the numerical side, the semi-empirical models describing the droplet/wall interaction [13, 16] are tuned to a generalized database of results, primarily on single element airfoils. A notable improvement from the non-clustered treatment of splashing and bouncing is observed at the leading edge of the flap. A significant increase in the local collection efficiency is observed as a

result of the splashed and bounced droplets from further upstream. Near the trailing edge of the slat, a discrepancy with the experimental data remains, although the non-clustered approach shows improvement over the plain post-processing approach.

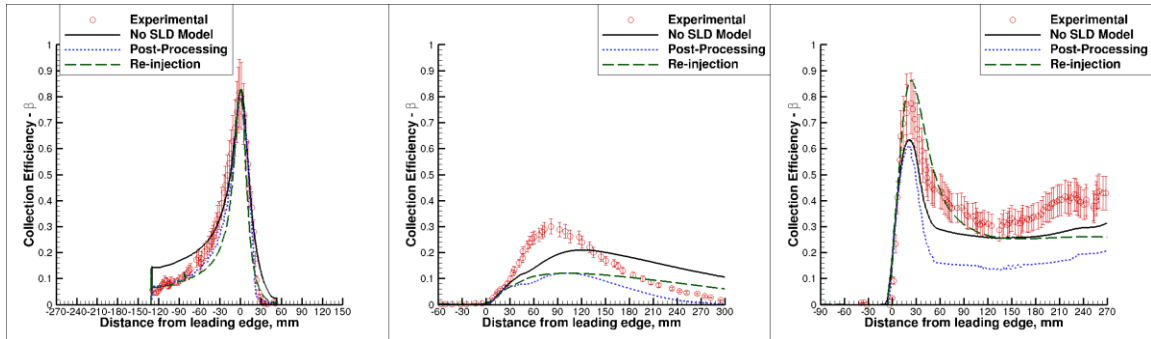


Figure IV-12: Comparison of the collection efficiency for the non-clustered treatment of splashing and bouncing on the slat (left), main element (center), and flap (right)

### IV.3.2 Clustered Approach with Complex Interacting Components

To validate the results of using the clustering approach to limit the computational cost, a previous test case [32] was selected, also using the McDonnell Douglas LB606b. The conditions for the non-clustered case are summarized in Table IV-2 with 97 droplet diameters used to approximate an Appendix O freezing drizzle condition. In the absence of experimental results, the non-clustered re-impingement solution is taken as a reference to compare the effects introduced by the clustering approach. The initial computational mesh is the same as the one used for the previous test, shown in Figure IV-11, but was enriched using solution-based mesh-enrichment [73] up to 411,000 nodes. The non-clustered approach required the computation of more than 55,000 additional droplet simulations. For the clustered solution, the  $J_e(2)/J_e(1)$  stopping criterion was used with agglomerative-divisive hierarchical clustering to reduce the re-injection computation to 489 additional droplet simulations. Figure IV-13 shows that the difference between the results of the clustered approach and the non-clustered approach for the slat and the leading edge region of the main element is quite small. In the flap cove, the clustered approach fails to capture all of the secondary impingement predicted by the non-clustered approach. The clustered approach matches very well the impingement near the leading edge of the flap, and for much of the lower surface of the flap. Some discrepancies are observed near the trailing edge of the flap.

<i>Parameter</i>	<i>Value</i>
Re	$24.31 \times 10^6$
$M_\infty$	0.2833
$T_\infty$	268.15 K
Pressure altitude	3,000 ft.
LWC	$0.15 \text{ g/m}^3$
AOA	$5^\circ$

Table IV-2: Summary of conditions used for the validation of the clustering approach

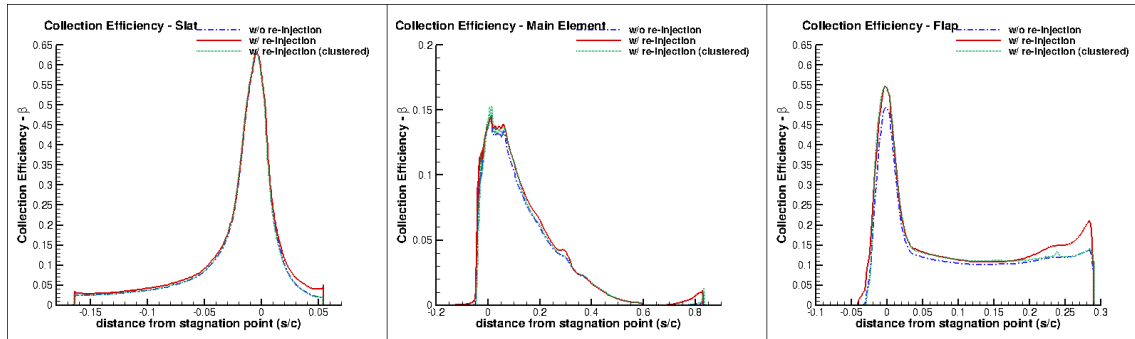


Figure IV-13: Collection efficiency for the Appendix O validation case comparing the non-clustered (w/ re-injection) and clustered (w/ re-injection clustered) approach to a simple post-process (w/o re-injection) for the slat (left), main element (center) and flap (right)

To further examine the discrepancies between the non-clustered approach and the clustered approach, ice was accreted assuming that the airflow and the droplet impingement remained unchanged for 30 minutes. The aerodynamic performance degradation was evaluated for the two computed ice shapes and a comparison between the predicted lift penalty and drag increase for the two approaches is shown in Figure IV-14. The maximum difference in lift penalty is less than 15% and the maximum difference in drag increase is less than 17%. The computational cost difference however was extreme, with the non-clustered approach costing an additional 14 core years whereas the clustered approach required less than 0.14 additional core years to the 0.8 core years needed to calculate the primary impingement. A core year is defined as a CPU running for 365 days continuously and is used to examine the cost of a numerical simulation when parallel CPUs are used. Although there are some differences between the two approaches, the accuracy of the clustered approach is acceptable, while its computational cost remains reasonable as a lower cost method of demonstrating the susceptibility of the airfoil to the Appendix O conditions. Also, having computed a low cost

solution and possibly noting a significant effect from the rebounded droplets, the non-clustered case could be justified to determine a more accurate representation of the SLD effect.

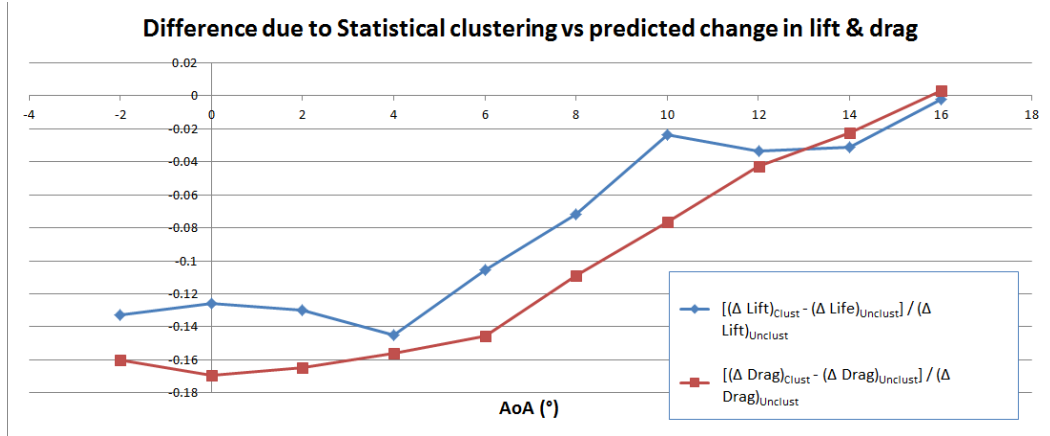


Figure IV-14: Normalized lift penalty and drag increase comparison between the non-clustered and clustered approach for 30 minutes of ice accretion

#### IV.4 Three-dimensional Test Case

The Trap-wing geometry from AIAA HiLiftPW-1 was selected for the assessment of the method in three dimensions subject for the impingement conditions summarized in Table IV-3. The ten (10) droplet diameters [71] used to approximate the distribution for an MVD of 92  $\mu\text{m}$  are shown in Figure IV-15. The computational mesh used to compute the flow and droplet primary solutions consisted of more than 8,800,000 nodes and more than 21,000,000 elements.

Parameter	Value	Parameter	Value
$V_\infty$	78.7 m/s	LWC	0.21 g/m <sup>3</sup>
$P_\infty$	19871 Pa	MVD	92 $\mu\text{m}$
$T_\infty$	230.48 K	AOA	8°
$c$	6.27 m		

Table IV-3: Summary of test conditions for the Trap-wing case

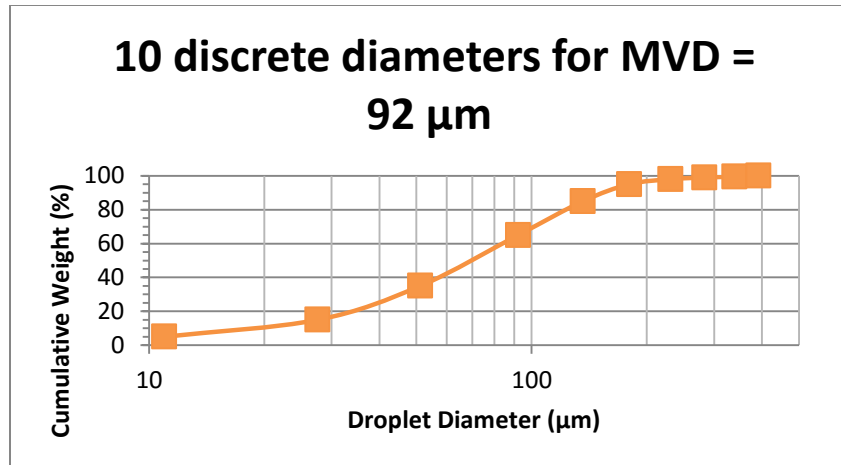


Figure IV-15: Cumulative distribution for the 10 diameters used to approximate the MVD=92 μm distribution from Papadakis, *et al.* [71]

The clustered approach was applied using the  $J_e(2)/J_e(1)$  stopping criterion for agglomerative-divisive hierarchical clustering, with sample LWC contours shown in Figure IV-16. These sample LWC contours show only the regions with LWC greater than freestream, either resulting from the deflection of the droplets due to the aerodynamic forces around the wing or from the splashing and bouncing. Clearly visible above the upper surface of the wing is an increase in the LWC as a result of the secondary droplets. Additionally, along the upper surface of the fairing there is an increase in the LWC and a change in the shadow region due to the presence of the secondary droplets. Figure IV-17 shows the comparison of the simple post-processing approach to splashing and bouncing (left) with the clustered re-injection result (right). Several regions showing the difference between the two solutions ( $\beta_{clustered} - \beta_{post-process}$ ), are highlighted.

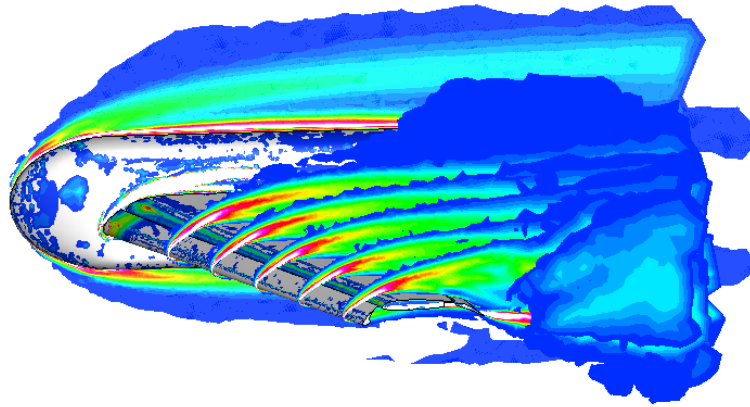


Figure IV-16: Sample LWC contours of the splashed and bounced droplet mass using 89 clusters.

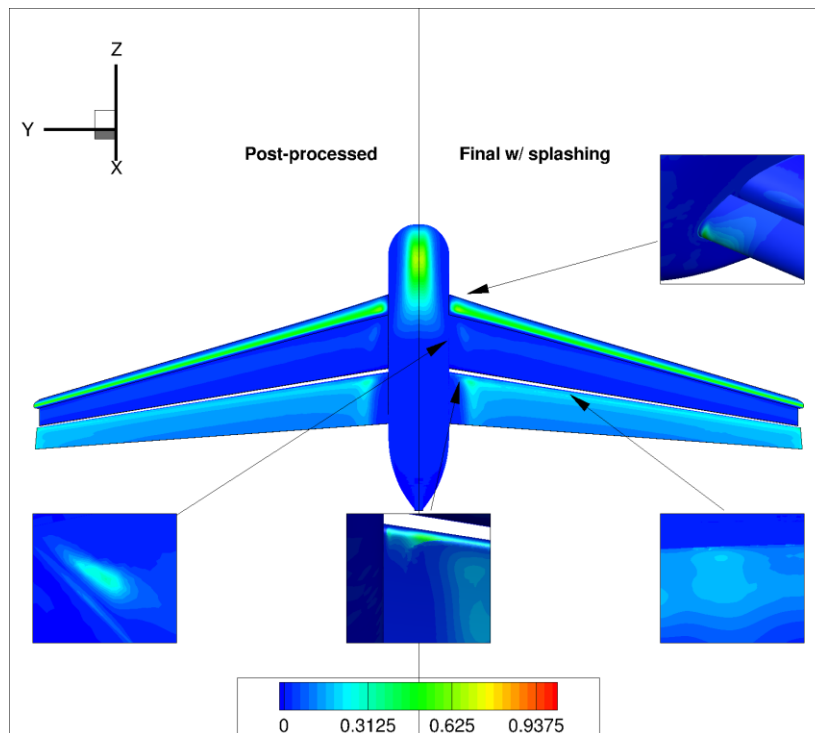


Figure IV-17: Comparison of the Collection Efficiency considering splashing and bouncing. Insets show  $\beta_{clustered} - \beta_{post-process}$  to highlight the effect of the secondary droplets

Ice accretion was computed for a 5-minute duration using the conditions in Table IV-3, resulting in very different icing characteristics and a 28% increase in ice mass as shown in Figure IV-18. While much of the contaminated region is covered by thin amounts of ice, this ice may have an

effect on the surface roughness. This roughness can alter the aerodynamic performance of the wing with an additional drag penalty and can possibly cause flow separation.

While the cost of computing the splashing and bouncing on the Trap-wing using the non-clustered approach would have been prohibitive with more than 900,000 re-injections solutions to compute, an attempt was made to determine if the impingement solution was reasonable. This was done by removing the stopping criterion and instead stopping the divisive step of the hierarchical clustering at a user-defined maximum. This maximum value was increased from 5 to 10, 20, 30 and finally 40 clusters per discrete primary diameter, or a global maximum of 50 to 400 clusters. The re-injected droplets were tracked and the final collection efficiency was compared to the clustered approach. As the number of clusters increased, collection efficiency approached that of the clustered approach as seen in Figure IV-19. The clustered approach however only required 89 total clusters with some of the primary diameters impingement solutions only requiring 4 clusters and others requiring greater than 15 clusters. Without an a priori knowledge if the splashing and bouncing will have an effect on this geometry and condition, it would be hard to justify the extremely high cost of computing every single facet as an individual solution in order to obtain an accurate picture of the effect of the rebounded droplets.

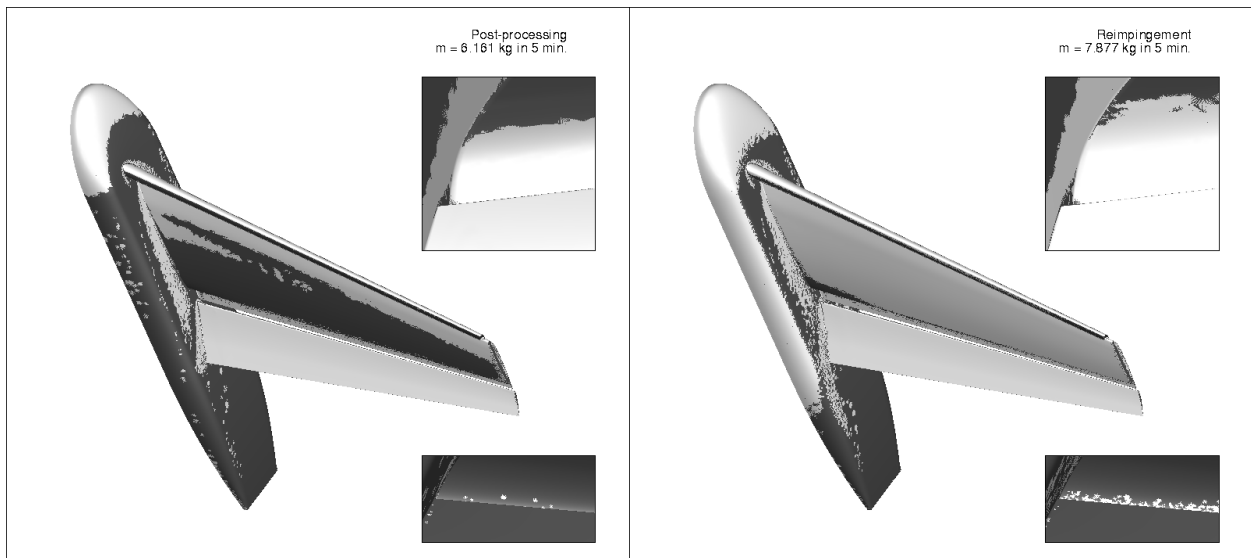
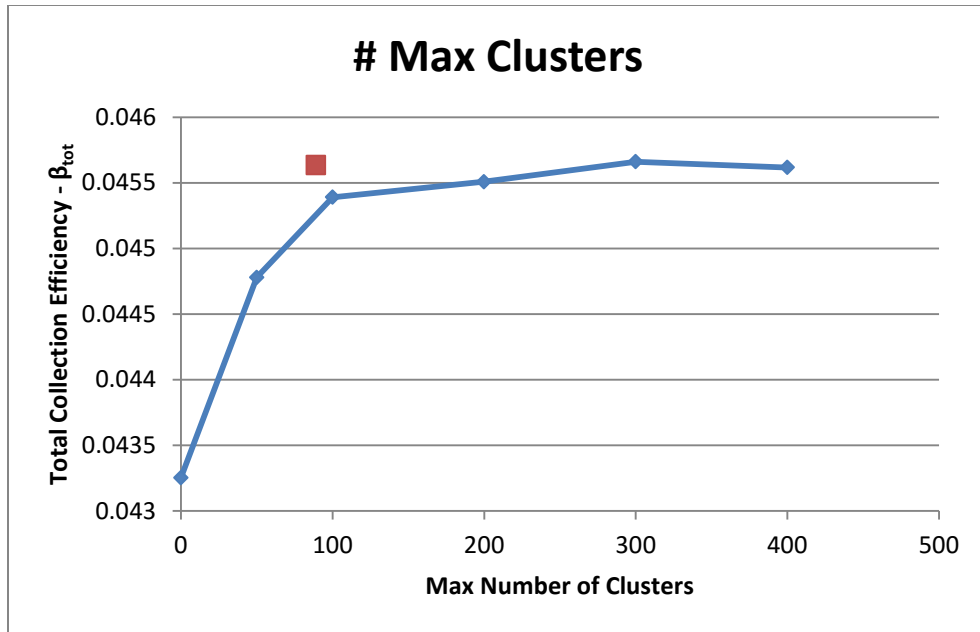


Figure IV-18: A comparison of the iced regions considering 5 minutes at the test conditions



**Figure IV-19: The total collection efficiency as a function of the total clusters.  
The red dot shows the clustered approach with the stopping criterion**

An additional phenomenon that may have an impact on SLD impingement is the detachment of liquid runback from trailing edges. As a part of the evaluation of the potential effect of detachment, both a two-dimensional and a three-dimensional model are proposed in Chapter V, along with validation (where possible) and limitations.

## Chapter V NUMERICAL MODELING OF DROPLET DETACHMENT FROM TRAILING EDGES

A mathematical model for the detachment of water droplets at trailing edges is developed first in two dimensions. It will need to account for the forces acting on the droplet due to aerodynamic shear, surface pressure, gravity, buoyancy, and the resistance to detachment due to surface tension. The component of the centrifugal forces acting in the two-dimensional plane will also be considered. While there are previously proposed models for droplet detachment, they are primarily for flat plate conditions and not for conditions and geometries typical of in-flight icing. Droplets at trailing edges may experience extremely dissimilar forces from the upper and lower surface conditions which will require giving special attention to the modeling of those forces. Another phenomenon that the model will need to be prepared for is the presence of separated regions. This model is then extended to three-dimensions with care taken to the decisions regarding the shape of the droplet surface and contact angle distribution.

### V.1 Two-dimensional Model

A two-dimensional model is proposed first with simplifying assumptions into the droplet shape and contact with the surface. The droplet is assumed to not affect the aerodynamics in the region of a sharp corner, allowing one-way coupling to be used with the aerodynamic solution.

#### V.1.1 Two-dimensional Model Details

The droplet is assumed to have a quasi-circular profile with the center at the geometric corner, as shown in Figure V-1. If the assumption is made that the forces acting on an isolated droplet are 'small' enough, a circular cross-section can be assumed. Once the forces become 'large', the assumption of a circular cross-section is not very accurate, as deformation will occur. As there is no conclusive research in the literature at present as to the deformation of an isolated droplet on a surface in the range being considered, a quasi-circular cross-section is always assumed. The profile deviates locally from a circle only at the point of contact with the upper and lower surfaces, to respect the contact angle  $\theta$ . As the model is being designed for water droplets on aircraft surfaces (which are primarily aluminum) and the contact angle for water-aluminum is close to  $90^\circ$ , the deviation from a circular profile is not significant. Local normal ( $\hat{n}$ ) and tangential ( $\hat{t}$ ) directions are defined on the surfaces in contact with the droplet. It is assumed

that the intersection of the droplet with the edges occurs at the droplet radius  $r$ . The angle  $\psi$  defines the corner between the edges.

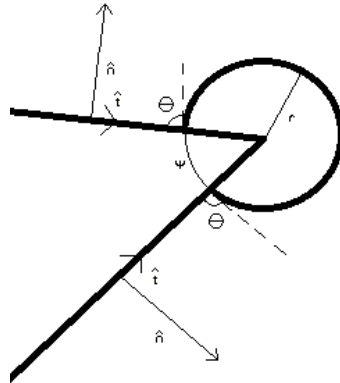


Figure V-1: Model of a two-dimensional isolated droplet at a geometric corner.

The direction of the resultant of the forces acting on the droplet is the criterion used to determine if the droplet remains attached or if it detaches. If the dot products of the vector resulting from the sum of the forces with the surface normal for the top and bottom surfaces are both less than 0, the forces are adhering the droplet to the surface. If either of the dot products is positive, then the resultant of the forces is pointing away from one of the surfaces and the droplet is assumed to detach, as shown in Figure V-2.

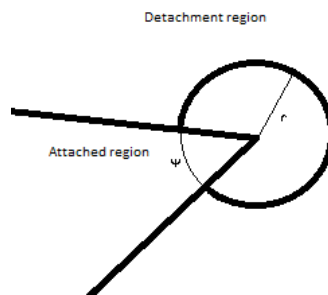


Figure V-2: Regions where droplet remains attached and regions where detachment is assumed to occur.

The surface tension force is modeled based on the following assumptions:

- the contact angle  $\theta$  is explicitly known and is the same for both corner surfaces
- the liquid droplet is isolated and so the effect of incoming water is ignored

With those assumptions, the surface tension force can be written as:

$$\vec{F}_\sigma = \int_0^L \sigma \cos(90^\circ - \theta)(-\hat{n}) + \sigma dl \sin(90^\circ - \theta)(-\hat{t}) \quad (\text{V.1})$$

For the present model, the following assumptions were made regarding the shear force:

- the velocity profile normal to the surface is linear
- shear remains constant with distance from the surface
- shear varies linearly between adjacent surface nodes in the computational domain
- the surface of the droplet is a circular arc
- the value of the shear force at the point of intersection with the surface remains constant for the remainder of the edge in the  $\hat{t}$  direction

These assumptions allow the shear force to be modeled as:

$$\vec{F}_\tau = \int_0^L \tau(r) dl \hat{t} \quad (\text{V.2})$$

Several assumptions were made with regards to the pressure force:

- $P$  varies linearly between surface nodes in the computational domain
- the effect of the curvature of the droplet at the corner on the pressure distribution is neglected (one-way coupling)
- the pressure force can be decomposed into two forces acting in the  $\hat{t}$  and  $\hat{n}$  directions
- the pressure is constant in the tail and head regions of the droplet

According to these assumptions, the pressure force can be written as a combination of the pressure acting in the  $\hat{t}$  and the  $\hat{n}$  directions for both the tail and head regions as:

$$\vec{F}_P = \int_0^L P_{0(r)} dl \hat{t} + P_{s(r)} \left( r - r \sin \frac{\psi}{2} \right) dl (-\hat{t}) + P_{0(r)} r dl (-\hat{n}) + P_{s(r)} \left( r \cos \frac{\psi}{2} \right) dl (-\hat{n}) \quad (\text{V.3})$$

where  $S(r)$  denotes the off-wall trailing edge position at a distance of  $r$  in the direction whose angle is  $(\pi - \psi / 2)$  from corner edges and  $r$  is the distance from the wall. The approach of

Zhang, [4] was adopted to provide the critical radius at which the buoyancy and gravitational forces become non-negligible. When

$$r > r_{crit} = \sqrt{\frac{0.06 * \sigma}{g(\rho_{water} - \rho_{air@corner})}} \quad (V.4)$$

the gravitational and buoyancy forces should be added:

$$\vec{F}_g = m\vec{\sigma} \quad (V.5)$$

$$\vec{F}_B = \rho_{air@corner} * \frac{m}{\rho_{water}} (-\vec{\sigma}) \quad (V.6)$$

where  $m = m(r, \psi, \rho_{water})$  is the mass of the liquid droplet. If centrifugal forces were present, they are projected into the two-dimensional plane where they are added to the resulting forces. A summation of the forces acting on the droplet results in:

$$\vec{F}_\tau(\psi(r), r, \psi) + \vec{F}_P(\psi(r), r, \psi) - \vec{F}_\sigma(\psi) \quad (V.7)$$

Should the criterion by Zhang, *et al.* [4] be met and should the conditions necessitate the inclusion of centrifugal forces (such as in the case of a helicopter rotor or a turbofan), the summation of the forces would result in:

$$\vec{F}_\tau(\psi(r), r, \psi) + \vec{F}_P(\psi(r), r, \psi) + \vec{F}_g + \vec{F}_B + \vec{F}_\omega - \vec{F}_\sigma(\psi) \quad (V.8)$$

### V.1.2 Model Sensitivity

In the absence of experimental data to validate the proposed two-dimensional model, a sensitivity study was performed to evaluate the effect of variations in  $P$ ,  $\psi$ ,  $\theta$ ,  $\tau$  and  $\sigma$  on the computed diameter of detaching droplets. The detachment model was tested making use of the McDonnell-Douglas LB606b airfoil in the 30P-30N configuration, whose geometric characteristics are summarized in Table V-1. A detail of the computational grid used for this study is presented in Figure IV-11. This grid was generated automatically using an in-house code [74]. Nine sets of asymptotic conditions were used as part of the sensitivity study at four

different locations (each with different local conditions, including  $\psi$ ) evaluated with 21 levels of discrete perturbation. The asymptotic conditions are summarized in Table V-2. The various asymptotic conditions result in different solutions on the surface and in the region around the trailing edge, which results in different boundary conditions being applied to the detaching model as a result of that aerodynamic solution.

<b>Geometric Parameter</b>	<b>Value</b>
Chord (m)	0.9144
Slat deflection (°)	30.
Slat overlap slat (% chord)	-2.5
Slat gap slat (mm)	26.97
Flap deflection (°)	30.
Flap overlap (% chord)	0.25
Flap gap (mm)	11.61

**Table V-1: Geometric characteristics of the MD LB606b airfoil**

Two methods of sensitivity study were employed, with the one-at-a-time approach providing insight for a two-variable and three-variable perturbation analysis [75]. In the one-at-a-time approach, individual boundary conditions of a model are subjected to a range of ‘small’ perturbations [76] to determine their effect on the output. The input parameters are then ranked by the magnitude of the output perturbation to provide a subset of the input parameters for further analysis (using the two- and three-variable perturbation approach for example). In the  $n$ -variable approach,  $n$  input parameters are perturbed to create a response surface. A representative result of the one-at-a-time analysis is shown in Figure V-3. Since  $P_3$  is the value of the pressure at the upstream node on the lower edge, used to determine  $P_{0(r)}$  for the lower surface, a perturbation in  $P_3$  results in a direct perturbation on  $P_{0(r)}$ . Perturbations were applied as a percentage of the magnitude of the shear stress and as a percentage of the maximum difference in pressure. In Figure V-3, the cross symbols represent the discrete location of the perturbation, with the horizontal axis indicating the percentage of the perturbation in  $P_3$  and the vertical axis showing the magnitude of the perturbation in the predicted diameter.

Perturbing  $P$ ,  $\theta$ ,  $\tau$ , and  $\sigma$  typically resulted in less than a 1% difference in the diameter of the detached droplet for all values of  $\psi$ . 5 of the 36 base cases were identified as having a larger output difference compared to the magnitude of the input perturbation. In these extreme cases, the boundary conditions differed by an order of magnitude, resulting in wide variations in the input parameters due to the perturbation. The model appeared to be most sensitive to perturbations of the pressure values at the upstream nodes and detachment location and to the magnitude of the shear stress at the detachment location.

Case (notes)	Pressure (kPa)	AoA (°)	V (m/s)
1	101.325	0	88.643
2	101.325	4	88.643
3	101.325	8	88.643
4	101.325	4	125.00
5	101.325	8	125.00
6	101.325	0	164.136
7	101.325	4	164.136
8	69.691	8	164.136
9 (with Gravity)	69.691	8	164.136

Table V-2: Test conditions for the sensitivity study.  
Common conditions: characteristic length (L) = 0.9144 m and  $T_\infty = 268.15$  K

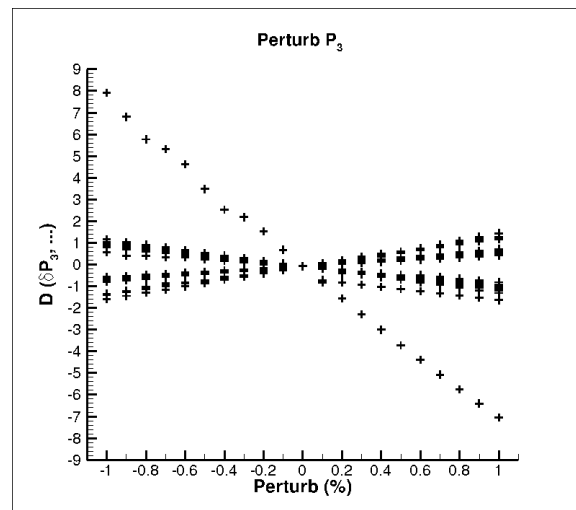


Figure V-3: A representative result of the one-at-a-time sensitivity study for the conditions evaluated

A two-variable evaluation of the shear stress ( $\tau_2$ ) and pressure ( $P_2$ ) at the detachment location was performed. As in the one-at-a-time method, the output perturbation was minimal compared to the input perturbation as shown in Figure V-4. Of the 36 cases evaluated, 5 had extrema deviating from that shown in Figure V-4 (left), with the most extreme being shown in Figure V-4 (right). These 5 cases correspond to the same cases identified as extreme in the one-at-a-time analysis. A three-variable evaluation was conducted with the pressures at both upstream nodes and the detachment node being perturbed. The typical change in predicted diameter was less than  $\pm 2.5\%$  at the most perturbed locations. There were a few extreme cases, as in the one-at-a-time and two-variable methods, with the most extreme difference being  $-10\% < \partial D < 17\%$ .

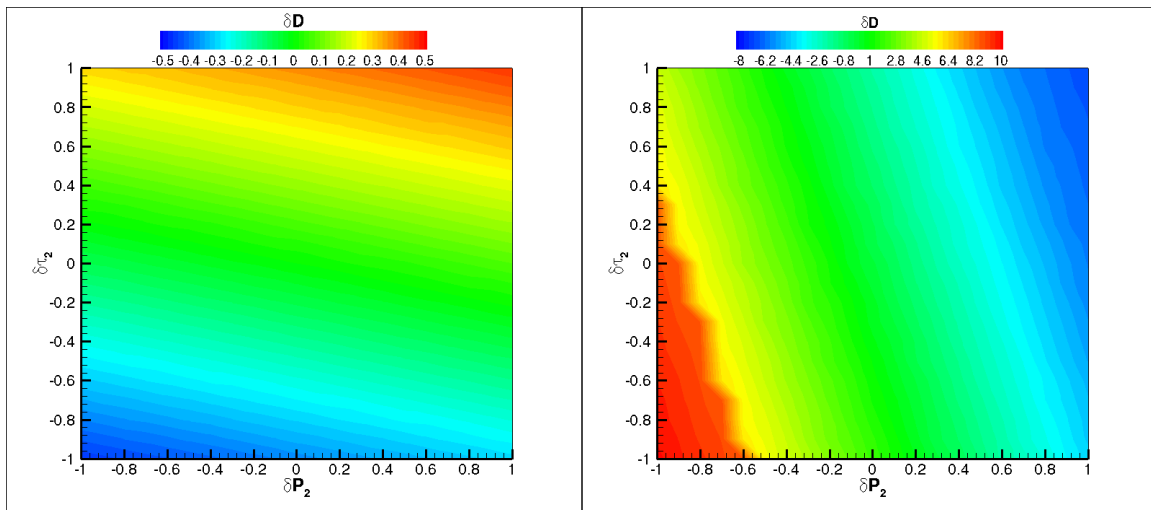


Figure V-4: Typical results of the 2 Variable sensitivity study perturbing the shear stress and pressure at the detachment location (Left) and the most extreme result of the 2-Variable sensitivity study (Right)

### V.1.3 Two-dimensional Trailing Edge Detachment Test Case

The two-dimensional droplet detachment model was applied to predict the detachment size for a McDonnell-Douglas LB606b airfoil, with the following free-stream conditions for the aerodynamic solution:  $P_\infty = 70.124$  kPa,  $T_\infty = 268.15$  K,  $V_\infty = 93$  m/s,  $AoA = 5^\circ$  and  $L = 0.9144$  m. The diameters of the detaching droplets were computed at 5 locations and varied from approximately  $500 \mu\text{m}$  to  $2.0$  mm in size. As this test case was not a part of an ice accretion study, no surface runback information was available to determine a Liquid Water Content

(LWC) at each detaching location. A constant LWC of  $1 \text{ g/m}^3$  was assumed for all detaching locations, and water droplets were re-injected to determine the potential effect of trailing edge detachment. Figure V-5 shows that there is some liquid water that re-impinges on downstream surfaces. Droplets detaching from the upper edge of the slat impinge on the upper surface of the main element, and droplets detaching from the trailing edge of the main element impinge on the flap.

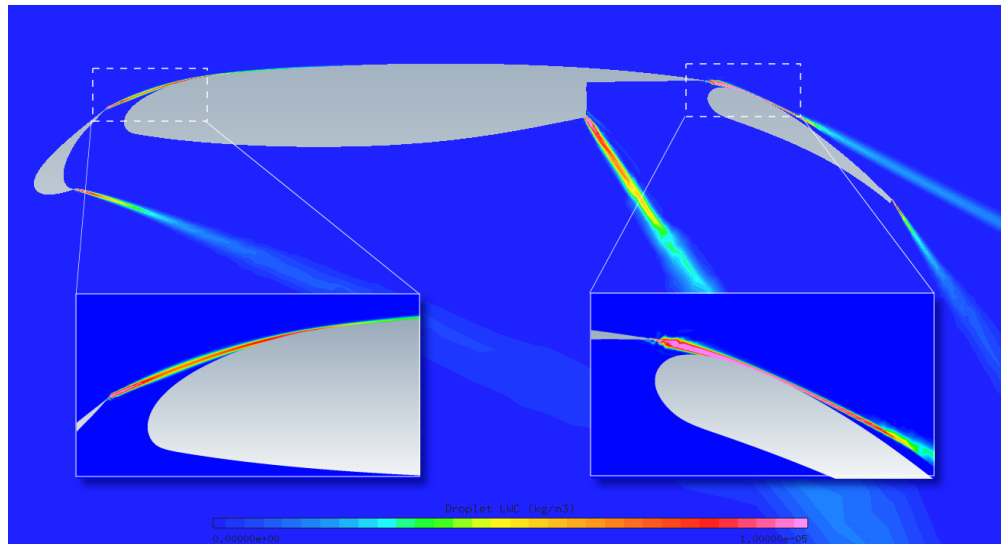


Figure V-5: LWC contours from the re-injection of detached droplets.

#### V.1.4 Limitations

Based on the sensitivity studies, the two-dimensional model appears to be insensitive to small perturbations of the boundary conditions for most cases. Since for this model, the boundary conditions being prescribed come from the aerodynamic solution at the nodes on the surface and in the freestream near the trailing edge, the mesh density in the region of the trailing edge has an effect on the model accuracy. The extreme cases revealed that in situations where the boundary conditions are very dissimilar, such as conditions when the mesh density is too coarse or when the detachment location is bounded by regions of strong recirculation and reverse flow, the model is sensitive to perturbations in the pressure and shear stress. When the mesh density is too coarse, mesh refinement [73] should make the model less sensitive to minor perturbations. In the presence of strong recirculation, the model will be unable to provide

accurate predictions unless the model describing the flow phenomena acting on the droplet is improved.

The model also suffers from issues with the extension to three-dimensions. Forces can no longer be computed per unit depth but must be computed with an assumed three-dimensional shape. The simplest assumption is to extend the assumed two-dimensional cross-section to make a cylindrical shape. An alternative shape involves the rotation of the quasi-circular profile about the sharp corner while maintaining the intersection with the surface. These two differing approaches produce differing forces due to the surface area and cross sectional profile that result.

One of the greatest limitations of the two-dimensional model is the assumption that the presence of the droplet does not impact the aerodynamic flow. While on a macroscopic scale this assumption is valid, as the droplets on the surface increase in size, the local disturbance of the flow in the vicinity of the droplet may become quite pronounced. By assuming the pressure forces can be obtained from the unperturbed flow is simple, it dramatically under-predicts the magnitude of the pressure drop across the droplet at even moderate freestream velocities. While the literature lacks experimental results for detachment from trailing edges/sharp corners, there are experimental results for droplets detaching from flat plates due to aerodynamic forces [4, 56, 77-79] to compare with. Theodorakakos, *et al.* [77] injected water from the bottom surface of a channel and then subjected the droplets to aerodynamic loads, recording the diameter at the moment of detachment. The channel was modeled with an artificial, spherical droplet placed at the location of liquid injection at the diameter that was experimentally determined for detachment and compared with a channel without a droplet, as seen in Figure V-6. A significant pressure variation between the empty channel and channel with droplet exists. In reality, the droplet would deform slightly as shown in the images of Theodorakakos, *et al.* [77] which would reduce the difference in the pressure drop across the droplet, though the magnitude of the difference between the empty channel and the one with droplet remains greater than an order of magnitude. As a result, it was deemed inappropriate to model the detaching forces by assuming the droplet did not perturb the flow and the

formulation presented for the two-dimensional model was not adopted for the three-dimensional analysis.

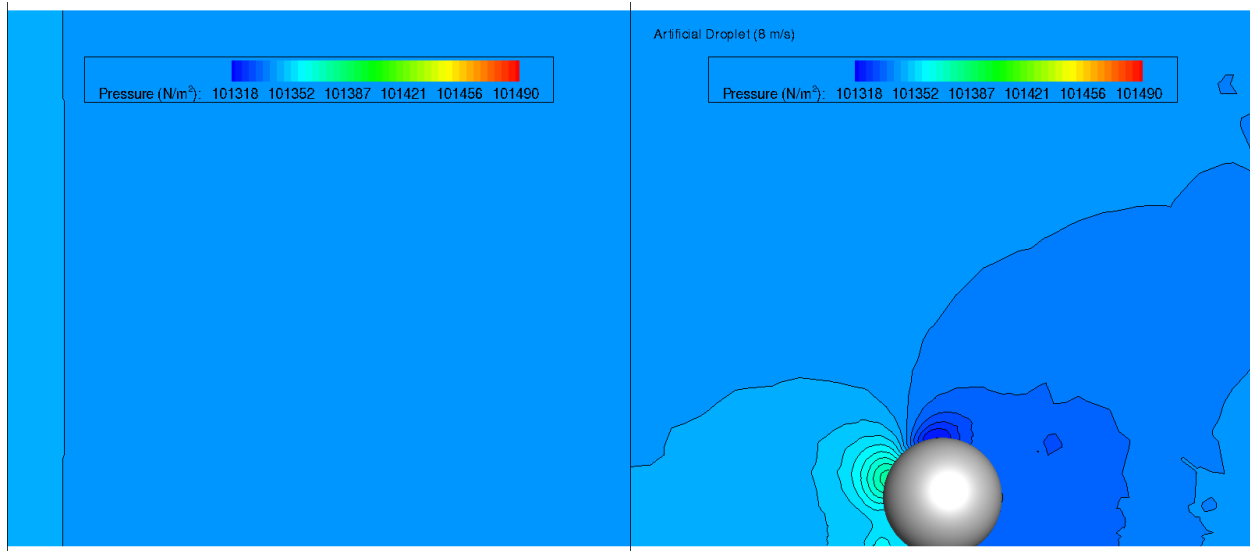


Figure V-6: The channel of Theodorakakos, *et al.* [77] without (left) and with (right) an artificial droplet in the air path. Significant pressure variation exists around the droplet

## V.2 Three-dimensional Model

The issues of the two-dimensional model, along with the possibility of validating a three-dimensional model by comparison with experimental results [4, 56, 77-79] of droplet detachment in three-dimension necessitated reformulating the detachment model. The three-dimensional model will be explained, followed by validation and application.

### V.2.1 Model Explained

The droplet is assumed to be a spherical cap shape with the distance between the sharp corner and apex of the droplet being defined by the static contact angle between the surface material and liquid phase as seen in Figure V-7. This is accomplished either by constraining the intersection of the spherical cap shape so that the droplet naturally meets the surface at the specified contact angle or by assuming that the droplet deviates from a general spherical shape only locally to respect the static contact angle. The latter case is used only in specific conditions when the simplification of the assumed shape precludes the calculation of a positive droplet volume.

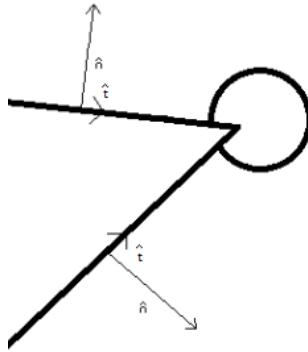


Figure V-7: Spherical cap shape, located at trailing edge of an airfoil, projected into two dimensions.

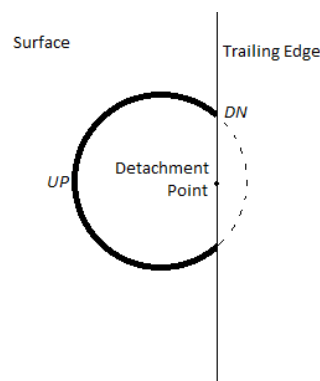


Figure V-8: Intersection of the assumed droplet with a surface on one side of the corner.

The primary adhesive force is the surface tension. Several assumptions are made as a part of the modeling, namely:

1. The contact line forms a circular profile on each connected surface, as seen in Figure V-8
2. The static, advancing, and receding contact angles are known
3. The liquid droplet is isolated and so the effect of incoming liquid on the shape and adhesion of the droplet to the surface can be ignored
4. The contact angle along the contact line varies linearly between the advancing and receding contact angles

The surface tension force  $F_\sigma$  is computed as the integration of  $dF_\sigma$  along the line of intersection between the droplet and the surfaces of the geometry as seen in Figure V-8, the intersection of the assumed spherical cap droplet is governed by the respecting of the static contact angle. The point labeled  $UP$  is assumed to have the receding contact angle. As the contact angle is

assumed to vary linearly, the point  $DN$  is computed based on the static contact angle and the radius of the droplet with the value of the contact angle at  $DN$  being computed from the linear variation between advancing and receding contact angles. The surface tension force is computed locally for each surface of intersection, allowing each surface to have unique boundary conditions for the integration. In Figure V-7 for example, both of the surfaces that the droplet is intersected appear upstream of the trailing edge resulting in receding contact angles for the extreme end of the contact line. The final equation for the surface tension force is given as:

$$F_{\sigma} = \sum_{i=1}^2 \left[ 2\sigma a \left[ \frac{-\pi \left[ \pi \sin(x) \cos\left(\theta_A - \frac{\Delta}{\pi} x\right) + \Delta \cos(x) \sin\left(\theta_A - \frac{\Delta}{\pi} x\right) \right]}{(\pi - \Delta)(\pi + \Delta)} \right]_{DN}^{UP} \hat{t}_i + 2\sigma a \left[ -\pi \frac{\cos\left(\theta_A - \frac{\Delta x}{\pi}\right)}{\Delta} \right]_{DN}^{UP} \hat{n}_i \right] \quad (V.9)$$

where  $a$  denotes the distance from the trailing edge to the centroid of the droplet,  $\theta_A$  is the advancing contact angle,  $\Delta$  is the contact angle hysteresis,  $x$  is the variable of integration along the contact line (with its limits being given by the upstream and downstream boundaries  $UP$  and  $DN$ ). In the two-dimensional model, the shedding/detaching forces were estimated from the forces due to the shear stress and the pressure. Since the pressure force is dominant in the detachment under most conditions, an accurate estimate of the pressure drop across the droplet is required. As the proposed model is to be used in a low-cost computational environment, the assumptions made in the two-dimensional model introduce a great degree of error in the estimation of the pressure force, in some cases being 2-3 orders of magnitude under-predicted. As a result, additional expressions were explored to model the detaching force. The combined drag force from Zhang, *et al.* [4] was selected:

$$F_{drag} = K_1 \frac{1}{2} C_{drag} \rho_{gas} U^2 A_p \quad (V.10)$$

where  $K_1$  is a corrective coefficient,  $C_{drag}$  is a drag coefficient,  $\rho_{gas}$  is the density of the gas phase,  $U$  is the freestream velocity of the gas phase, and  $A_p$  is the exposed frontal area of the droplet. Zhang, *et al.* [4] assumed that the combined effect of the shear and pressure forces acting on an isolated droplet in contact with a surface could be approximated using the drag experienced by the partial droplet. The great advantage over some of the previous work that relies on the work of Goldman is that the drag force presented by Zhang is more accurate across a larger range of Reynolds numbers. Additionally, as the droplet in contact with the solid surface is not a complete sphere, Zhang introduced a corrective coefficient to equation (V.10). In the work of Zhang, *et al.* [4], an empirical correlation is used for  $K_1$ , whereas in the present model it is assumed that the correction factor can be modeled as the ratio of the frontal area to that of a complete sphere with the same diameter.

The approach of Zhang, *et al.* [4] was adopted to provide the critical radius at which the buoyancy and gravitational forces become non-negligible. When the criteria in equation (V.4) is satisfied, the gravitational, buoyancy and centrifugal forces should be added:

$$\vec{F}_g = m_d \vec{g} \quad (V.11)$$

$$\vec{F}_B = \rho_g * \frac{m_d}{\rho_w} (-\vec{g}) \quad (V.12)$$

$$F_\Omega = m_d \left( \frac{\Omega^2}{r} \right) \quad (V.13)$$

where  $m_d$  is the mass of the liquid droplet,  $\vec{g}$  is the gravitational acceleration,  $\rho_g$  is the density of the gas phase,  $\rho_w$  is the density of water,  $\Omega$  is the rotational speed, and  $r$  is the distance from the center of the droplet to the center of rotation.

## V.2.2 Integration within a Multishot approach

In the previously discussed multishot approach for modeling in-flight icing, the runback of the surface film is computed as part of the ice accretion. As a result, determining how to incorporate the detached mass into the multishot framework requires some assumptions:

- The temperature change of the film on the surface is negligible resulting in the re-injected droplets being at the freestream temperature
- The predicted droplet size applies to the entire shot time, resulting in the total mass to be re-injected being divided to the LWC/time
- All re-injected mass only affects the next shot of the multishot

With the above assumptions, the multishot process with detachment is modeled as:

- An aerodynamic solution is computed in the customary manner
- The droplet impingement solution is computed with or without the effect of splashing and bouncing as outlined in III.1
- An ice accretion and film runback solution is computed for the desired shot time
- Locations with film buildup (film height > then a user defined threshold) are flagged as potential locations for detachment. The most downstream locations are converted to a flagged boundary condition and an additional computational mesh is saved
- An ice accretion and film runback solution is computed for the same shot time using the modified mesh where the flagged locations have a sink boundary condition
- The two film runback solutions are compared to determine the volume of liquid water arriving at each detachment location. The model presented in V.2.1 is applied to determine droplet detachment diameters and LWC is determined by assuming the volume of liquid arriving is able to leave at a uniform rate
- Secondary droplet solutions are computed with the detachment locations as inlets using the re-injection approach outlined herein
- The mesh is displaced to begin the next shot in the multishot framework. An aerodynamic solution is computed as is a droplet impingement solution. The secondary droplet solutions predicted as a result of detachment in the previous shot are combined

as a part of the droplet impingement for the subsequent ice accretion and film runback solution

This approach was implemented using FENSAP® as the aerodynamic solver, DROP3D® as the droplet impingement solver and ICE3D® to compute the ice accretion and film runback solution.

### V.2.3 Model Validation

There is a shortage of documentation regarding droplet detachment due to aerodynamic forces and none of the experiments discusses detachment from regions of sharp geometric features. As the predicted forces in the model are based on the corner angle, the model was extended to conditions where the corner angle approaches 180° for a flat plate. To validate the proposed detachment model, an experimental database by Theodorakakos, *et al.* [77] was selected where detailed experiments were conducted on various surfaces in a micro-channel flow. Three surfaces with different static, advancing, and receding contact angles, as reported in [77] as Figure 7 and shown again in Figure V-9 for completeness, were studied. The freestream velocity was varied from 5 m/s to 17 m/s to span the range of the tests performed by Theodorakakos. The droplet diameter at the moment of detachment (when the droplet began to move off and downstream with the aerodynamic flow) was carefully recorded, along with the cross-sectional shape of the droplet. Theodorakakos, *et al.* also presented results of a coupled, volume of fluid approach to numerically predict the detachment of the droplets in the same situation.

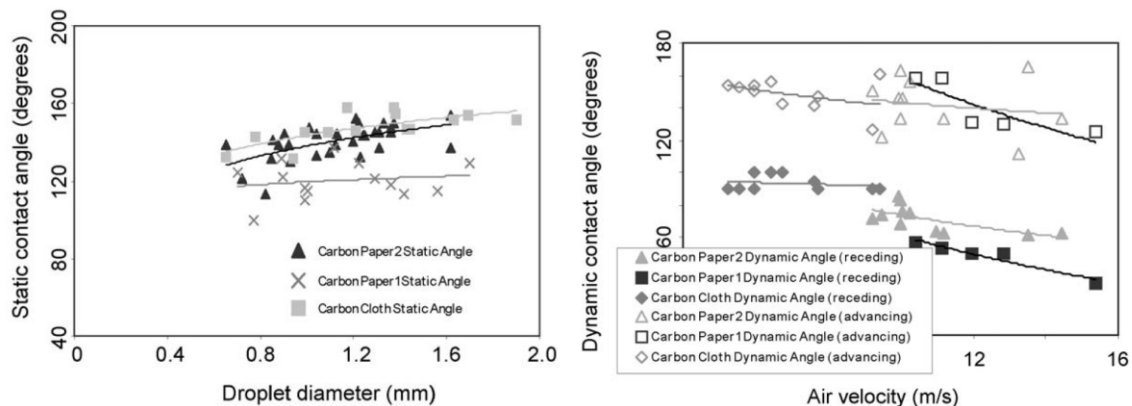


Figure V-9: Static and Dynamic contact angles for various droplet sizes as reported by Theodorakakos, *et al.* [77] as Figure 7

A mesh of 5,200,000 nodes and 5,095,629 hexahedral elements was generated to simulate the micro-channel. Aerodynamic solutions were generated [13] at various freestream velocities spanning the range of 5 m/s to 17 m/s, and the detachment model was used with the various contact angles recorded in the experiment to predict the detachment diameter.

As shown in Figure V-10, the predicted droplet diameter from the proposed model is very close to the measured values from experiment and to the Volume of Fluid results presented by Theodorakakos [77]. In Figure V-10, the symbols represent the experimental data from Theodorakakos, the colored line (denoted 'Calc, [surface type]) represent the results of the low-cost model presented herein, and the black line represents the results presented by Theodorakakos [77] employing a Volume of Fluid approach. Three different surface types, with differing contact angles, were employed by Theodorakakos [77] and the interested reader can examine [77] for their details. The names of the three surfaces in [77] are denoted as 'cloth', 'paper 1' and 'paper 2', respectively. While the agreement between experiment and the two computational approaches is quite good, in the case of paper 2, seen in Figure V-10C, the model over-predicted the detachment size. Theodorakakos, *et al.* [77] presented the variation in static, advancing and receding contact angles as both a function of the droplet diameter and the freestream velocity of the co-flowing fluid. While alternative contact angles were tested resulting in better results, in the present study the contact angles presented by Theodorakakos [77] were used. The reason for the discrepancy is likely due to the measured contact angle. The data for the contact angles for paper 2 appeared to contain outliers, and did not follow similar trends as the other measured contact angles when changing the droplet diameter or freestream velocity.

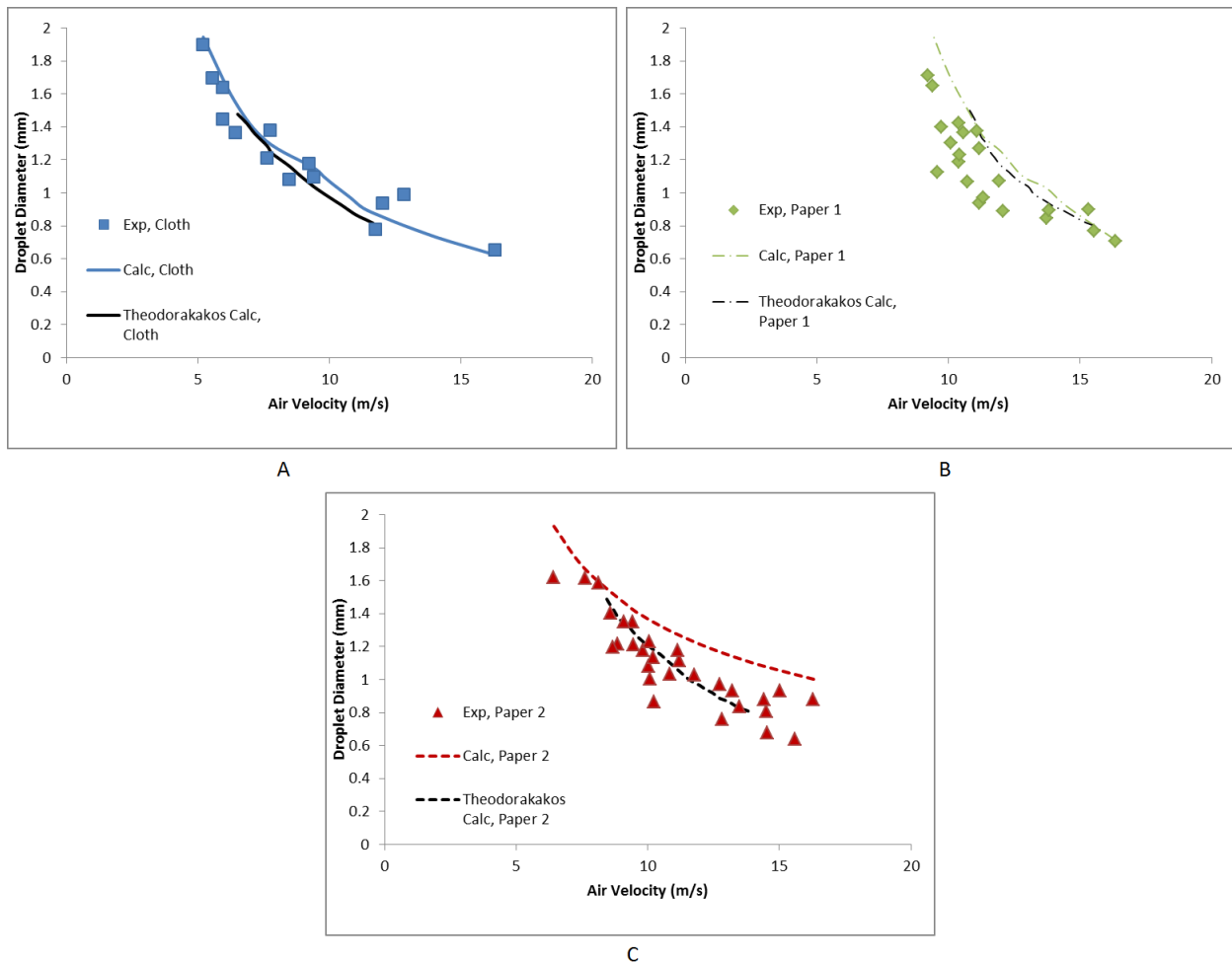


Figure V-10: Comparison between the experimental data of Theodorakakos, *et al.* [77], Volume of Fluid results from Theodorakakos and the results of the proposed detachment model for three surface A) a carbon cloth, B) a carbon paper and C) a second type of carbon paper

## V.2.4 Test Case

Two test cases were employed for the three-dimensional detachment model. The first was the Trap-wing geometry from AIAA HiLiftPW-1, subject to the impingement conditions summarized in Table V-3. The computational mesh used to compute the flow and droplet primary solutions consisted of more than 8,800,000 nodes and more than 21,000,000 elements. Only a single droplet diameter was employed with an unrealistically high LWC being prescribed. Ice was accreted in two equal shots of 5 seconds, for a total of 10 seconds of ice accretion. Even with the very high LWC and temperature near freezing, only minor amounts of liquid are predicted to detach from the surface and even less is predicted to impinge on a secondary location, as shown in Figure V-11 with the maximum difference being an order of magnitude lower than the

primary impingement. The bulk of the predicted change in the collection efficiency is much less, at 2-3 orders of magnitude lower than the primary impingement, suggesting numerical support for the assertion of Wright and Potapczuk [15] that in the case of an aircraft wing, droplet detachment can be classified as a second-order effect and provides negligible changes in the icing prediction.

Parameter	Value	Parameter	Value
$V_\infty$	70.0 m/s	LWC	1.00 g/m <sup>3</sup>
$P_\infty$	87887.82 Pa	D	500 μm
$T_\infty$	268.15 K	AOA	8°
$c$	6.27 m		

Table V-3: Summary of test conditions for the Trap-wing case

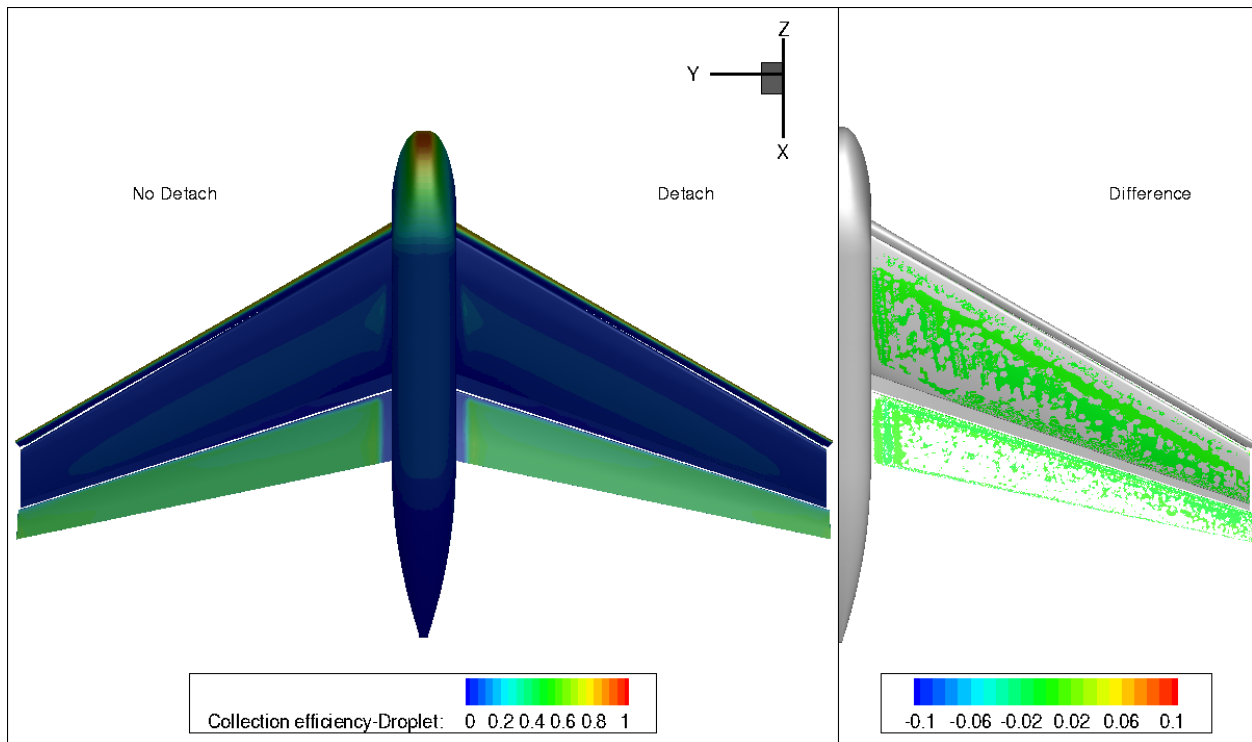


Figure V-11: Change in collection efficiency comparing no detachment to the predicted effect of detachment. The final difference is very small and is highlighted (right).

The second test case explored was a turbofan. The geometry modeled was the nacelle inlet, a fan blade, splitter, bypass, and inlet guide vane as seen in Figure V-12. FENSAP-ICE-TURBO was employed, requiring that each stage of the geometry be split into different computational meshes. Due to the deflection of smaller droplets along with the melting of ice crystals in

advance of the fan blade, much higher LWC values were available for study. The fan was studied with the mesh being refined to capture the secondary droplets with greater detail. The mesh for the fan employed 2,747,122 nodes and 2,673,482 elements and was rotationally periodic so that only 1 blade of the fan was studied. The region from the trailing edge to the exit plane of the turbofan stage was resolved with much greater detail than is typical for standard icing calculations in turbomachinery. The conditions for the simulation are summarized in Table V-4.

Parameter	Value	Parameter	Value
$V_\infty$	100.0 m/s	LWC	8.50 g/m <sup>3</sup>
$P_\infty$	75274.627 Pa	D	80 μm
$T_\infty$	268.15 K	AOA	0°
$c$	0.60 m	$t_{icing}$	30 s

Table V-4: Summary of test conditions for the turbofan case

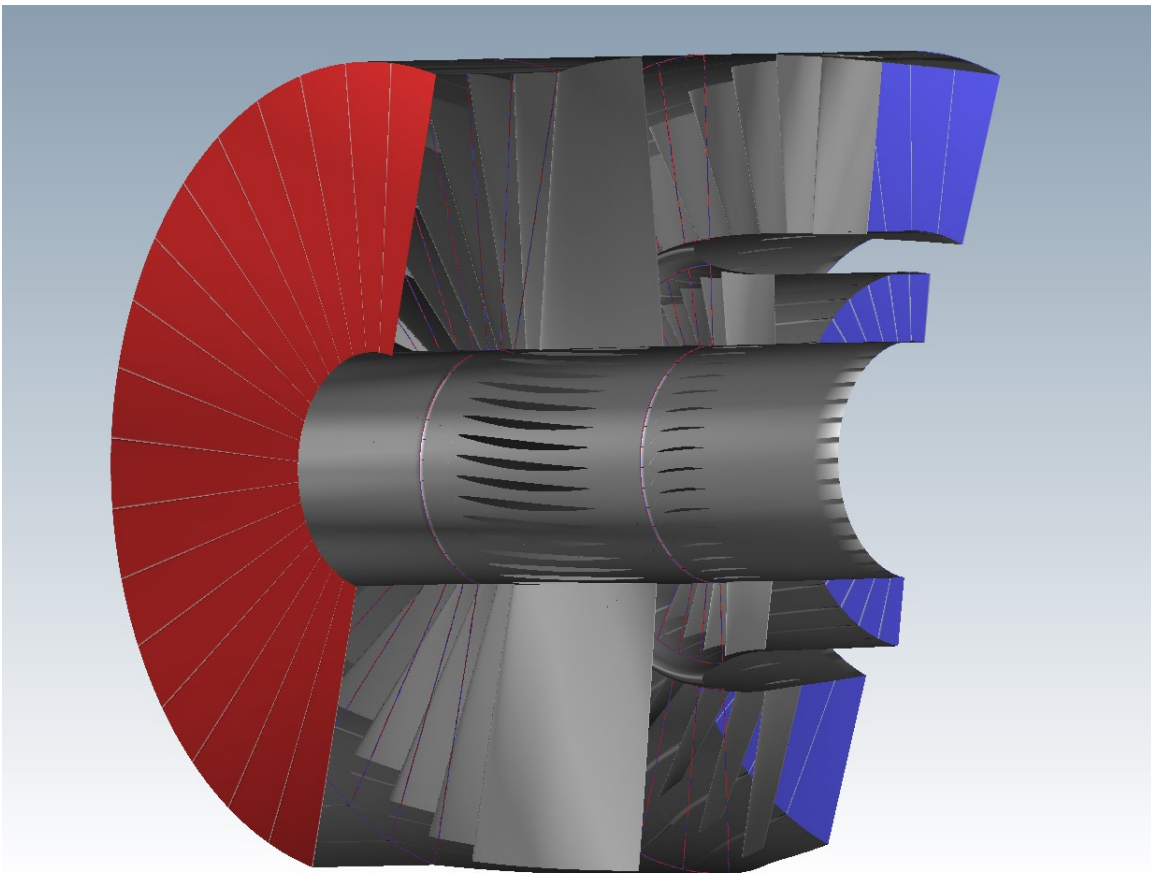
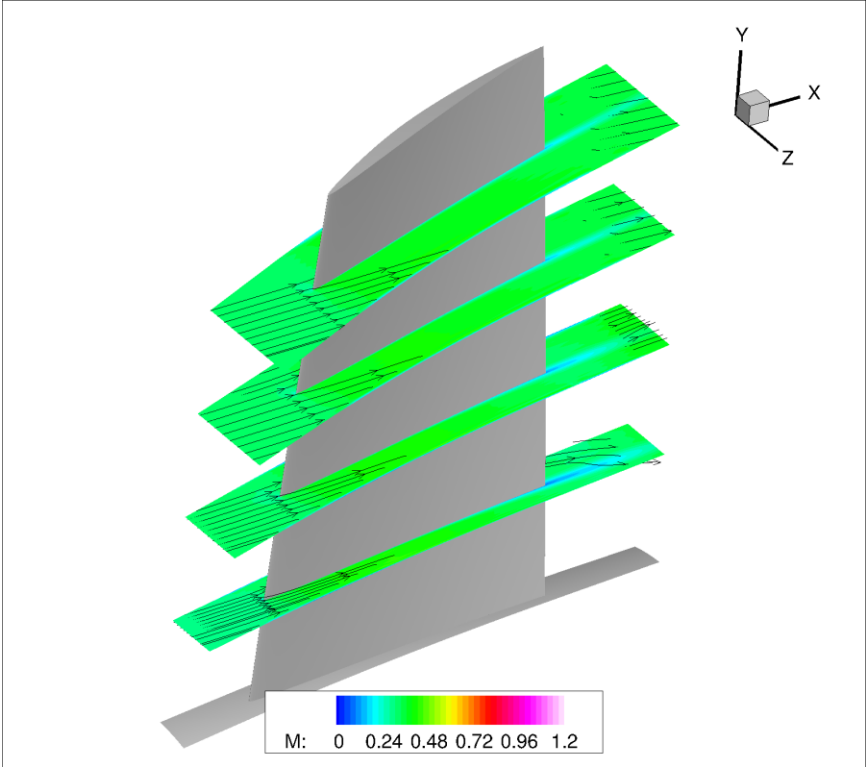
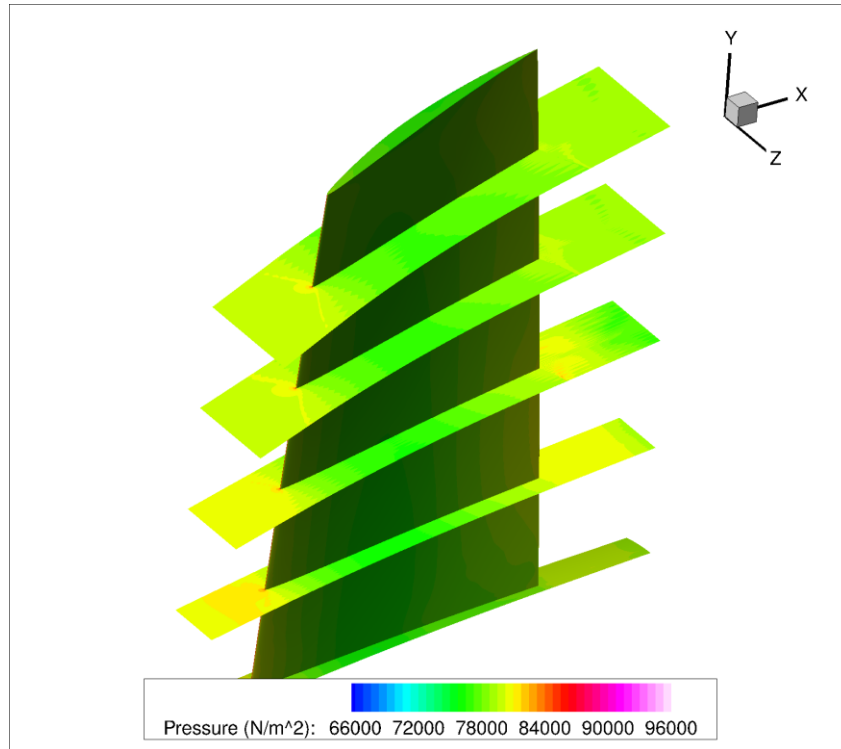


Figure V-12: Turbofan geometry studied

Shown in Figure V-13 are the Mach number contours around the turbofan blade with some sample streamlines. There is a region of flow separation near the hub on the back side of the blade. Figure V-14 shows sample pressure contours around the fan blade at the conditions indicated in Table V-4.



**Figure V-13: Mach contours around the turbofan blade along with select streamlines.**



**Figure V-14: Pressure contours at several radial positions on the turbofan blade.**

Shown in Figure V-15 are iso-surfaces bounding the region the re-injected droplets effect, coming from 3 instances of the turbofan blade. The bulk of the mass detaching from the trailing edge is predicted near the hub, with the droplet diameters varying from about 11  $\mu\text{m}$  to about 600  $\mu\text{m}$  at various locations. Figure V-16 shows the LWC contours at the exit of the turbofan stage from 3 instances of the turbofan. Figure V-17 shows the final LWC contours from both the primary impingement and the detached droplets predicted after 30 seconds, and how they will affect the first compressor stage of the geometry studied. While the conditions studied included a rather high amount of liquid water, the LWC arriving at the exit of the turbofan stage remains relatively insignificant. Table V-5 summarizes the effect of the detached mass as contributing less than 0.002% to the peak LWC at the exit plane and less than 0.0003% of the total LWC.

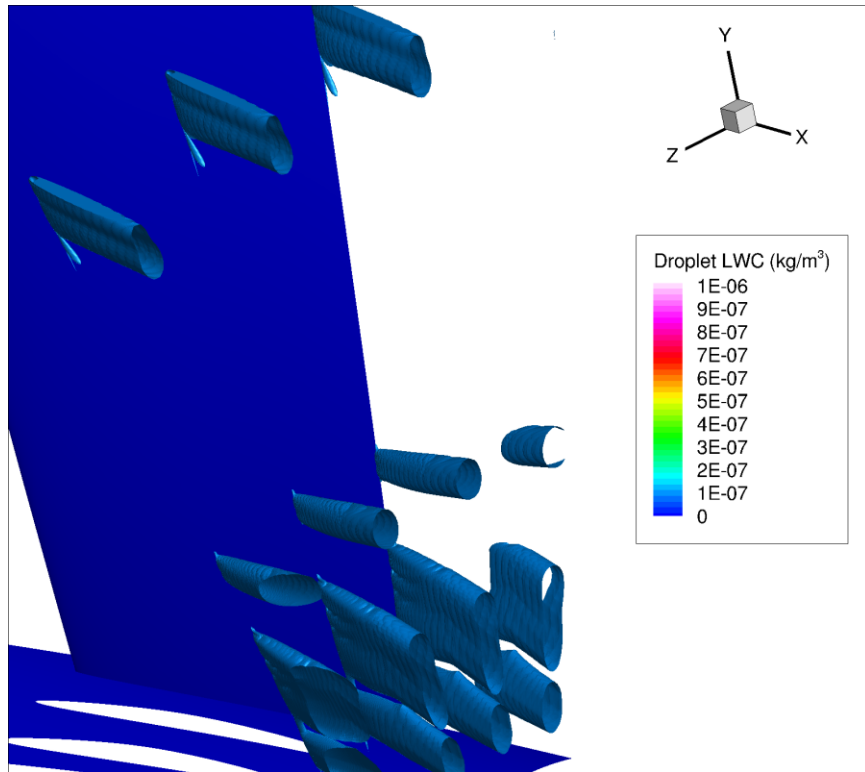
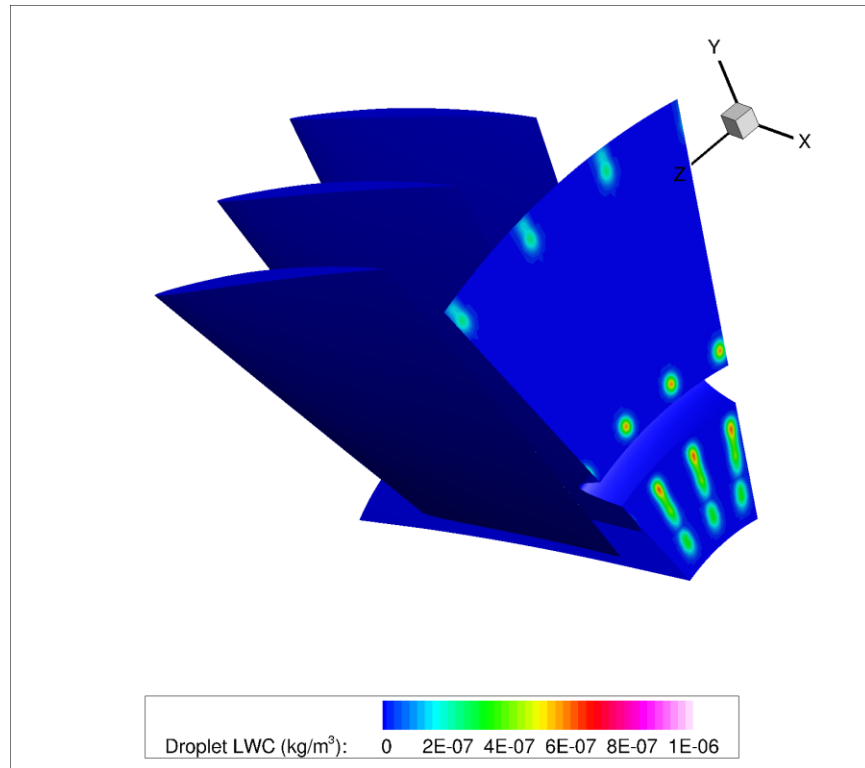


Figure V-15: Iso surfaces showing the effect of the detached droplets

	Without Detachment (kg/m <sup>3</sup> )	With Trailing Edge Detachment (kg/m <sup>3</sup> )	% Difference
Max LWC	0.0104977777	0.0104978908	0.00108
Total LWC	4.9409666E-05	4.94098053E-05	0.00028

Table V-5: Results of the detached mass



**Figure V-16: LWC at the exit planes from 3 turbfan blades**

It appears that the detachment of droplets from trailing edges for a turbfan blade is of little importance and has a negligible effect. Alternatively, a forthcoming study has recently shown that detachment during the surface runback, in advance of the trailing edge, subjected to adhesive forces in the form of surface tension and to detaching forces in the form of centrifugal forces may have a very pronounced effect on a turbfan [80]. This study of detachment during runback was performed as a part of the development of a commercial ice accretion code and compares to proprietary information for multi-stage turbfan inlets, though the results of this study should be presented in the near future. It is likely that detachment during runback has such a pronounced effect due to several factors. During the runback of the liquid water, isolated droplets that have not frozen are more susceptible to the relatively strong centrifugal forces as the adhesive forces on the droplet are limited to the area along the contact line around the droplet. Should the liquid form a rivulet or a cohesive film, the adhesive forces would have a larger area to distribute the detaching forces, potentially allowing greater mass to remain on the surface and runback to the trailing edge. Additionally, as the droplets are detaching during

runback, there is less time for heat exchange with the surface and for freezing to occur, resulting in a greater quantity of liquid that can detach.

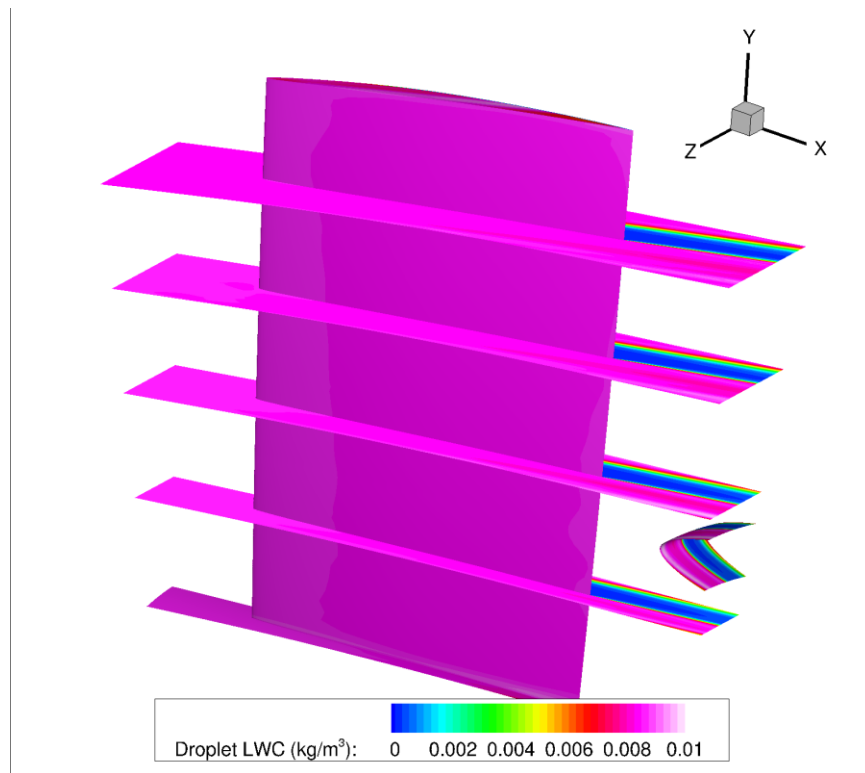


Figure V-17: Final LWC contours from both the primary and detached droplets as they will affect the first compressor stage of the geometry studied

## V.2.5 Limitations

While the three-dimensional detachment model offers advantages over the two-dimensional model, there are some limitations. It lacks complete validation for sharp corners and trailing edges, along with validation at higher freestream velocities. Additionally, the surfaces employed by Theodorakakos, *et al.* [77] were hydrophobic to super-hydrophobic and semi-porous in nature. The surfaces employed in aircraft wings and turbofan blades are typically aluminum, composite materials or metal alloys. These surfaces have a different contact angle than the hydrophobic and super-hydrophobic surfaces validated against and are also not porous.

Along with a limited validation, the modeling of droplet detachment is limited by the resolution of the mesh downstream of the geometry. Most CFD applications require a resolved mesh in the region near the geometry and in the upstream location. The downstream wake is often captured for the aerodynamic solution but the location and trajectory of the secondary droplets from detachment may not align well with the location of that wake. This results in a large amount of dissipation of the droplets as a result of the detachment. To track the mass effectively, a well resolved mesh is required in the downstream path. The initial mesh for the turbofan test case in V.2.4 was not sufficiently resolved, requiring significant mesh refinement. The computational cost for the turbofan test case was compared to the cost to provide acceptable results for primary impingement. The cost increased by more than  $2.0 \times 10^4$  due to the resolved mesh that was employed in the final study. It is unlikely that an engineer would be willing to increase the cost of simulating icing effects by such a large margin for a phenomenon which was demonstrated to have such a negligible impact on the overall impingement characteristics of an aircraft.

Having developed a model to predict the effect of detachment, along with approaches to investigate the effect of SLD splashing and bouncing, a realistic three-dimensional test case was evaluated in the form of an isolated rotor in hover. The investigation is presented in Chapter VI.

## Chapter VI ISOLATED ROTOR IN HOVER

A condition where both splashing and bouncing effects and droplet detachment may have an impact was studied in the form of an isolated rotor in hover. In the late 1970s and early 1980s, Caradonna and Tung [81] studied a rotor located at the Army Aeromechanics Laboratory to measure both the pressure on the blades as well as the tip vortices. They employed a 2 bladed, NACA 0012 with an untwisted and un-tapered profile. They studied conditions when the collective pitch was varied from  $0^\circ$  to  $12^\circ$  and the rate of rotation varied between 650 and 2400 rpm. The conditions selected for study are shown in Table VI-1. An Appendix O Freezing Drizzle condition was selected with an MVD  $> 40$  micron distribution. This resulted in a corrected LWC of  $0.22624 \text{ g/m}^3$ . The Appendix O distribution was approximated using 25 discrete diameters and they are shown in Figure VI-1. The mesh employed contained 3,119,372 nodes and 10,707,924 elements and is shown in Figure VI-2. Mesh adaptation and enrichment were performed iteratively to the final mesh as shown in Figure VI-3, which features 6,196,353 nodes and 21,375,878 elements. The aerodynamic simulation for this test case was a continuation of the work previously performed by Fouladi [82] as an unpublished extension to his PhD thesis work on Computational Methods for Rotorcraft Icing. Preliminary aerodynamic solutions and Appendix C droplet impingement solutions were performed by Fouladi [82]. In the present work, a similar approach to determine a flow solution was employed and the numerical code to compute the pressure coefficient, as provided by Fouladi [82] was used. To the best knowledge of the author, no data exists for comparison of droplet impingement profiles or ice accretion on this geometry though some comparison or study of the aerodynamics of the rotor are available in the literature from Palacios, *et al.* [83], Allen, *et al.* [84], Guruswamy [85], and many others.

Parameter	Value	Parameter	Value
$V_\infty$	149.618 m/s	LWC	$0.20966 \text{ g/m}^3$
$P_\infty$	101325.0 Pa	Pitch	$12^\circ$
$T_\infty$	270.15 K	$\Omega$	1250 rpm
$c$	1.143 m		

Table VI-1: Summary of test conditions for the isolated rotor case

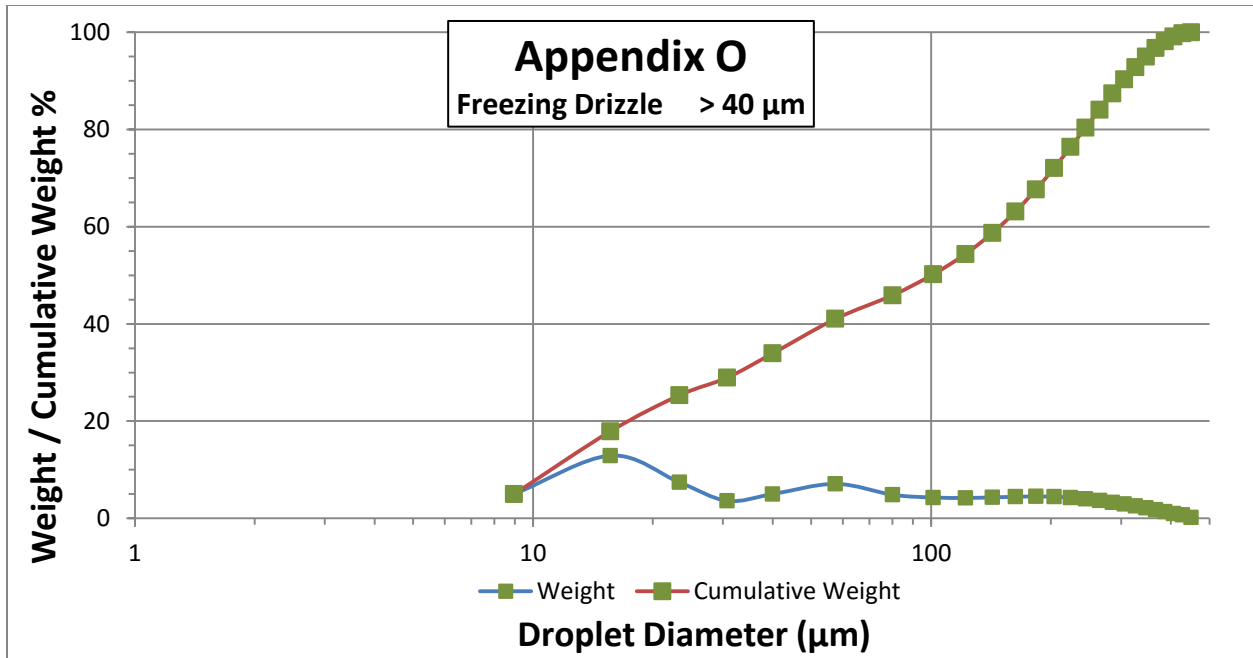
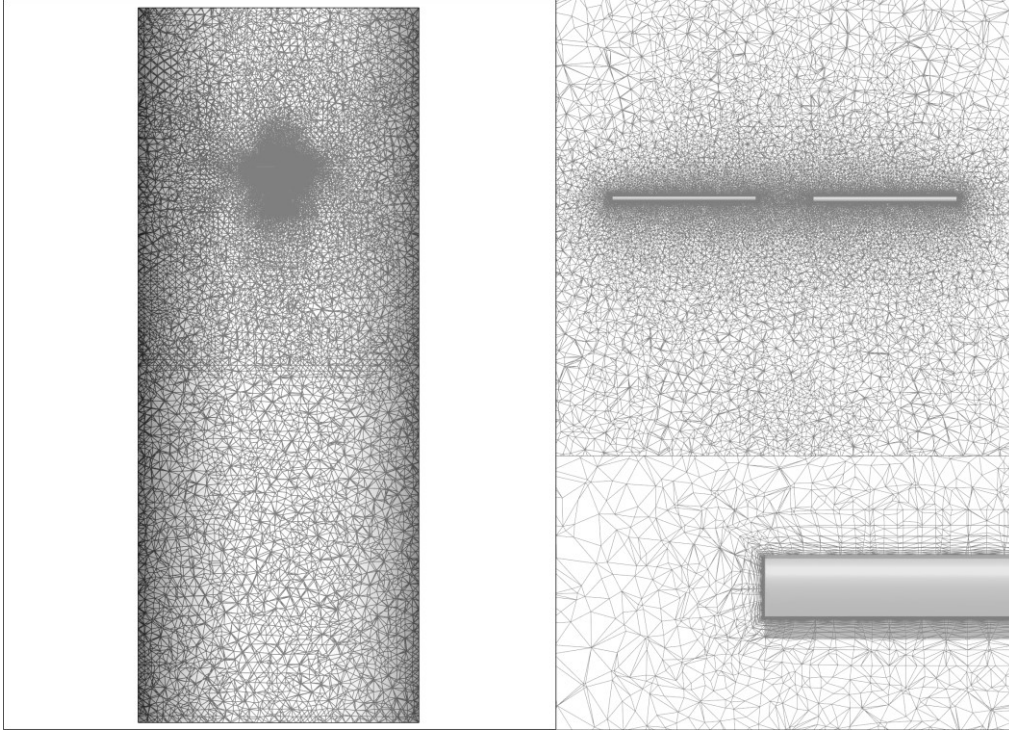
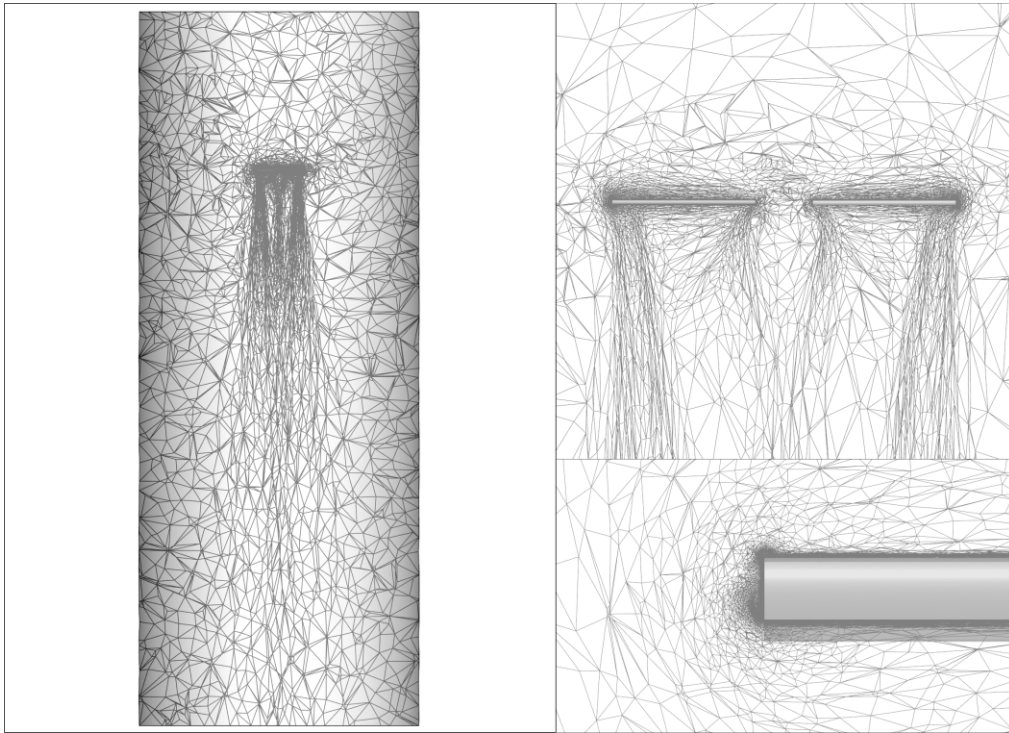


Figure VI-1: Appendix O Distribution with discrete diameters used to approximate the conditions

Comparisons of the pressure coefficient at four stations along the rotor are presented in Figure VI-4 through Figure VI-7. These results were computed at 24°C to more accurately match the experimental conditions based on the tip Mach number. For most of the stations, the pressure coefficient is in acceptable agreement with the experimental data. On both the  $r/R = 0.50$  and the  $r/R = 0.96$  positions, there are discrepancies on the upper surface near the leading edge. A number of factors may have contributed to the discrepancies. The hub was not modeled in the geometry, nor was the presence of the hot-wire probe nor its mounting structure. Additionally, the walls of the facility are not modeled in the aerodynamic simulation. With the intent of accreting ice, a temperature below freezing was ultimately employed, resulting in larger discrepancies when comparing the pressure coefficient with the experimental data, as seen in Figure VI-8.



**Figure VI-2: Initial mesh employed to study the Caradonna geometry. Full mesh (left), detail of rotor (top-right) and structured layers near the rotor tip (bottom-right)**



**Figure VI-3: Mesh employed to study the NACA 0012 rotor after 3 levels of adaptation and enrichment. Full mesh (left), detail of rotor (top-right) and structured layers near the rotor tip (bottom-right)**

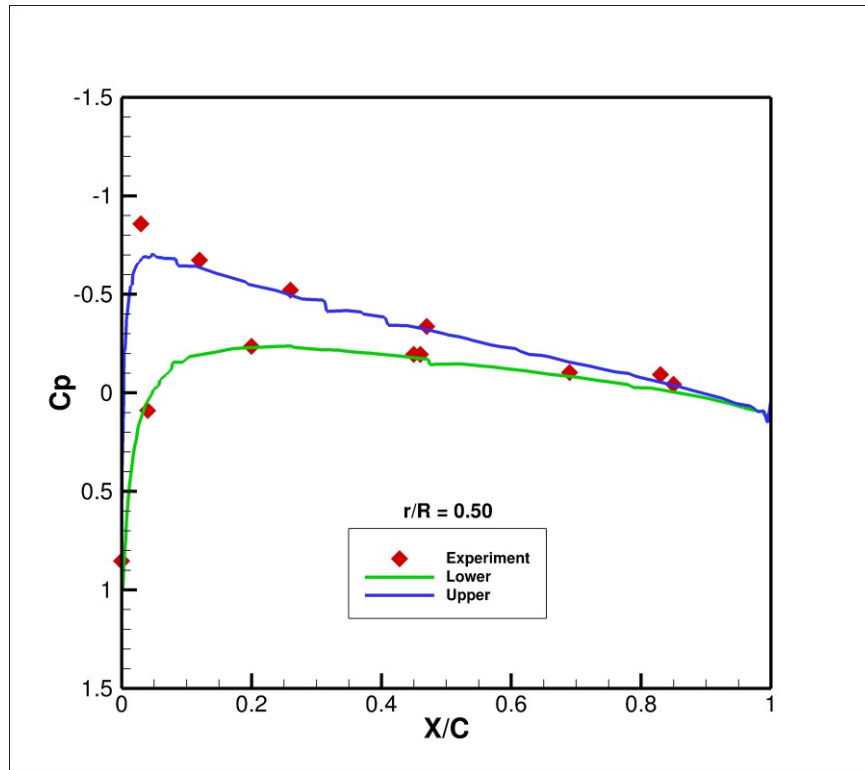


Figure VI-4: Pressure coefficient computed at  $r/R = 0.50$  as compared to Caradonna and Tung [81]

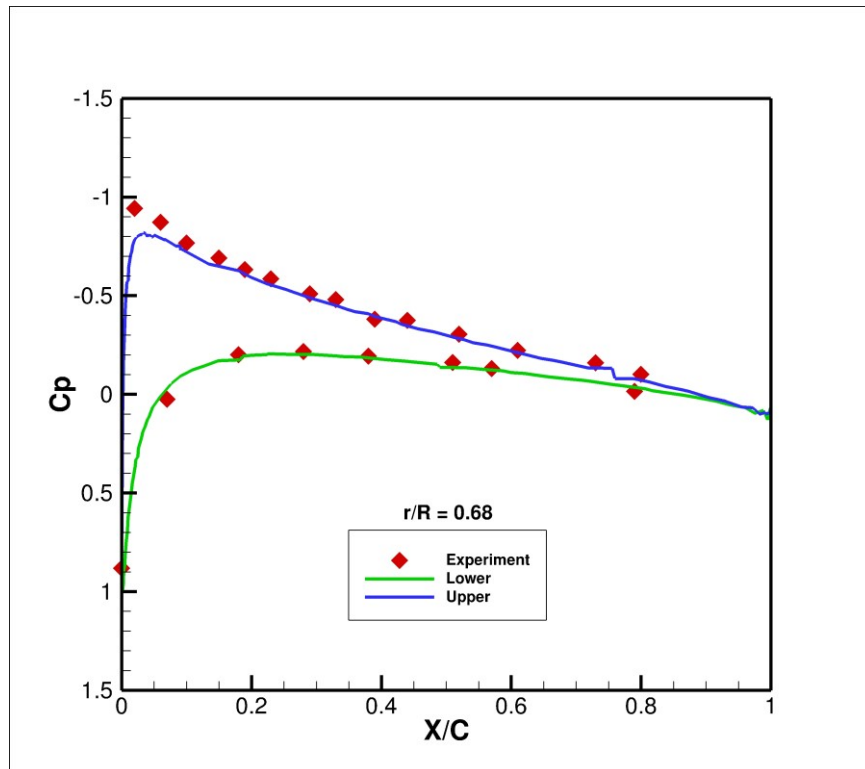


Figure VI-5: Pressure coefficient computed at  $r/R = 0.68$  as compared to Caradonna and Tung [81]

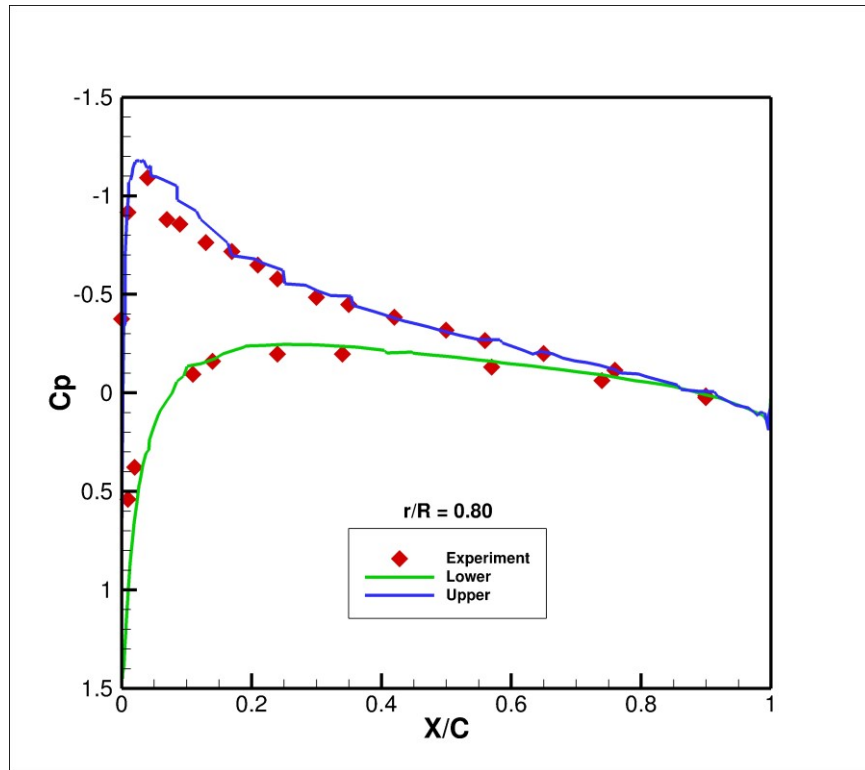


Figure VI-6: Pressure coefficient computed at  $r/R = 0.80$  as compared to Caradonna and Tung [81]

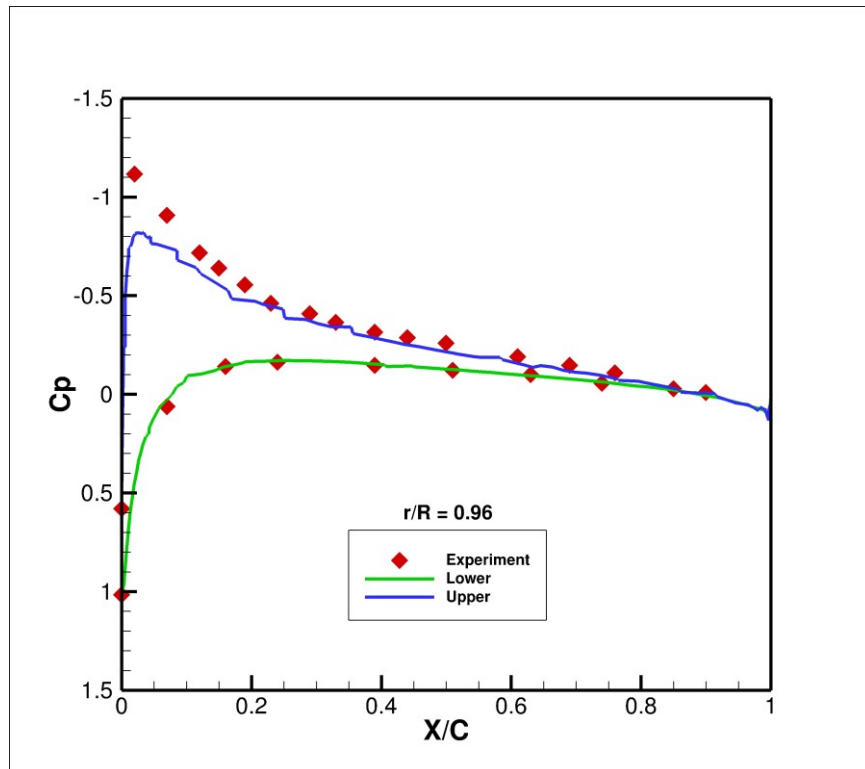


Figure VI-7: Pressure coefficient computed at  $r/R = 0.96$  as compared to Caradonna and Tung [81]

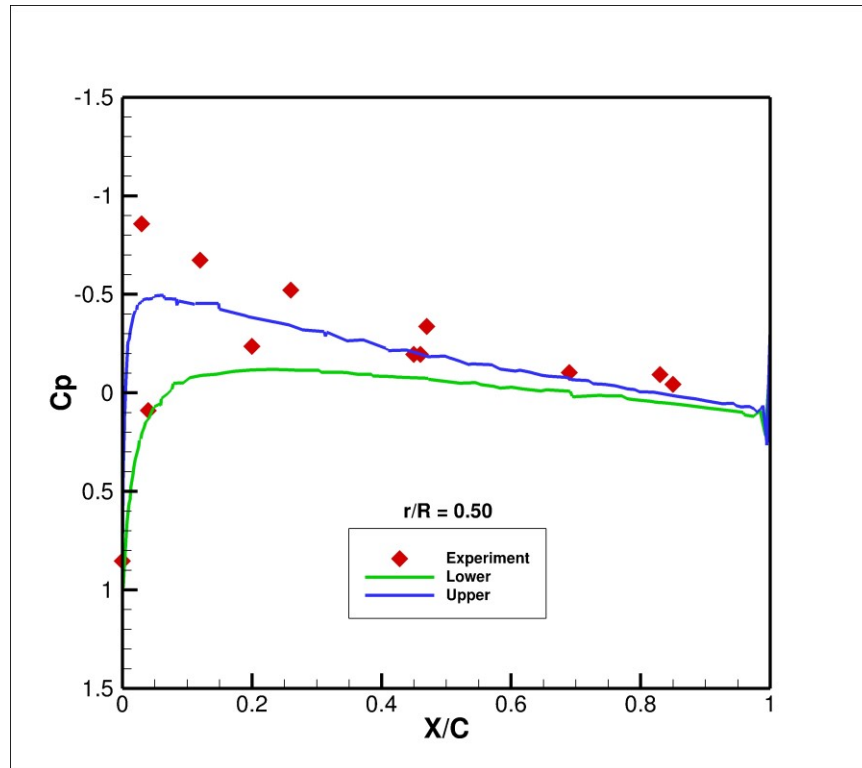
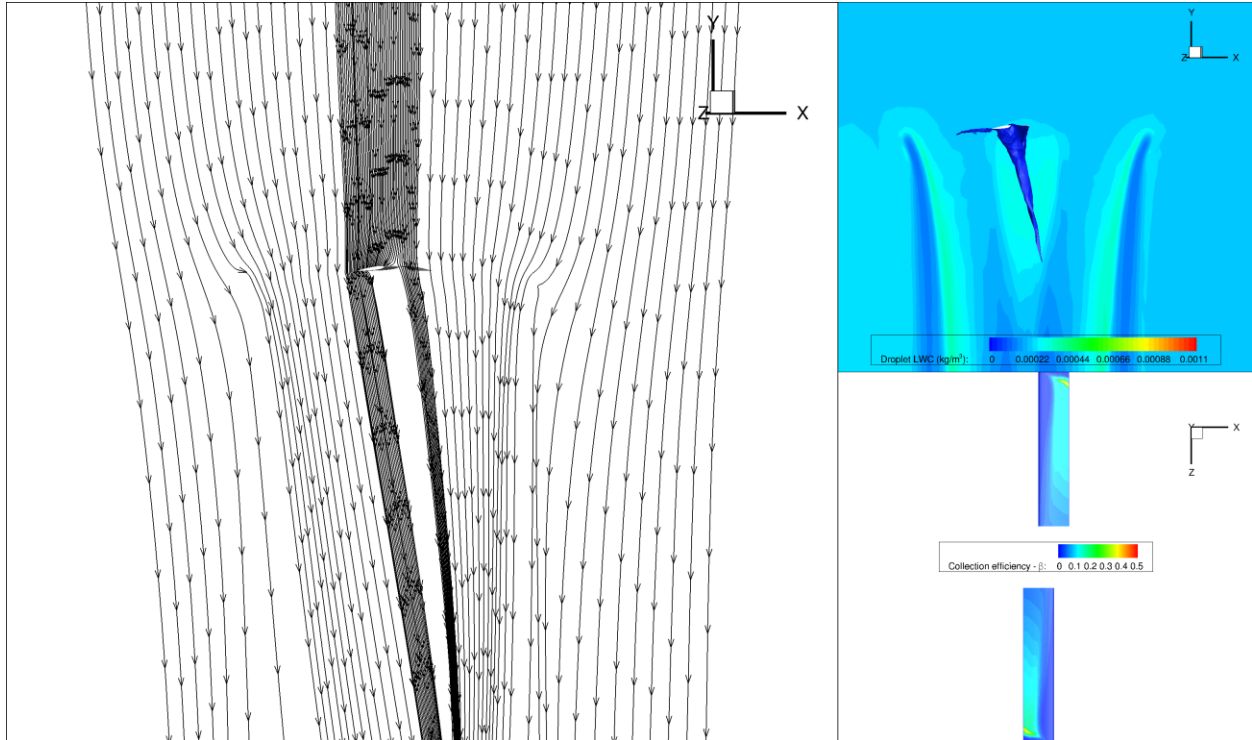


Figure VI-8: Sample pressure coefficient at  $r/R = 0.50$ , when a freestream temperature of  $-3^{\circ}\text{C}$  is employed to permit ice accretion, compared to Caradonna and Tung at  $24^{\circ}\text{C}$  [81]

Droplet impingement solutions were computed by making use of DROP3D<sup>®</sup> to compute the primary impingement. Some sample streamlines are shown in Figure VI-9. Due to the relatively large size of the droplets, the gravitational force dominates in most regions over the drag due to relative velocity as compared to the air. Due to the rotation of the blades, the shadow region below the blade would not be as well defined as it appears in Figure VI-9 but would be radially averaged. Instead, the streamlines presented show the instantaneous velocity field around the blades of the droplets. There are regions of lower LWC, as seen in Figure VI-9 (top-right) due to the aerodynamic interaction with the drag due to the airflow drawing additional droplets towards the rotor. The peak collection efficiency on the blades is 0.46 and the total collection efficiency for the two blades is  $\beta_{tot} = 0.02189$ . A simple post-process approach to SLD splashing and bouncing would result in a drop of the peak collection efficiency to 0.439 (a drop of about 5%) and the total collection efficiency to  $\beta_{tot} = 0.02151$  (a drop of about 2%).



**Figure VI-9: Droplet streamlines (left) in the Y-X plane.  
Iso-surface showing the shadow region and slice showing LWC contours (top-right).  
Collection efficiency ( $\beta$ ) on the blades (bottom-right).**

Computation of the secondary droplet solutions using the approach detailed in Chapter IV above, the change in the collection efficiency is summarized in Table VI-2. There is a significant decrease in the collection efficiency on the surface as a result of the splashing and bouncing. Table VI-2 omits the effect of the post-process approach as a very minor amount of mass that is re-injected impinges on the rotor surfaces, making the solution via a simple post-process and the solution via the clustered splashing and bouncing approach presented in Chapter IV almost the same. Figure VI-10 shows the collection efficiency on a single rotor blade as a result of a post-process approach. Figure VI-11 shows the collection efficiency after splashed and bounced droplets have been re-injected and allowed to impinge on the surface. Figure VI-12 shows a comparison between the post-process and re-injected approaches. It should be noted that the peak value in Figure VI-12 is more than three orders of magnitude lower than the peak value in Figure VI-10 or Figure VI-11. As a result of considering the splashing and bouncing, there is a 24% reduction in the peak collection efficiency and a 7.2% decrease in the total collection efficiency.

	Without Splashing & Bouncing	With Splashing & Bouncing + Re-injection	% Difference
$\beta_{\max}$	0.45778	0.34734	-24.1%
$\beta_{\text{total}}$	0.01121	0.01040	-7.2%

Table VI-2: Change in Collection Efficiency due to splashing and bouncing effects

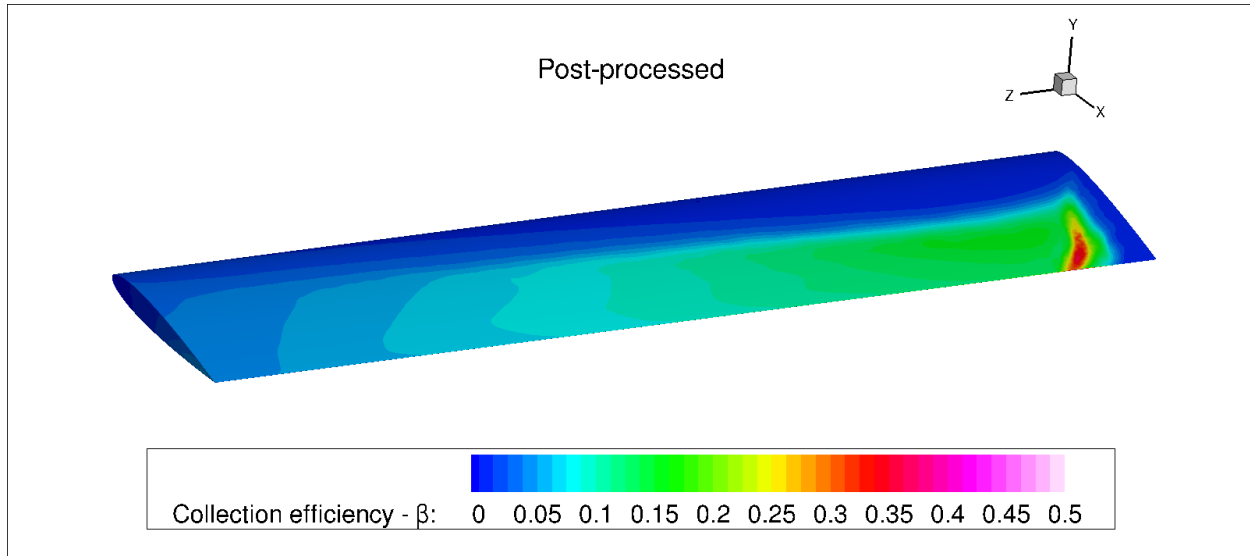


Figure VI-10: Collection efficiency on the surface of a single rotor blade from a post-processing approach

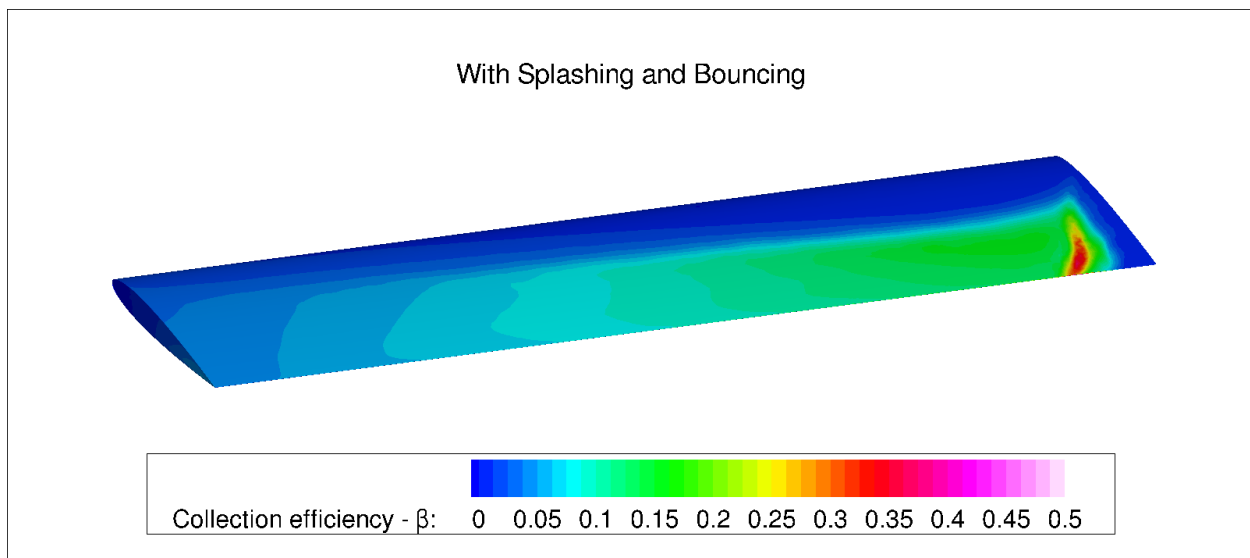


Figure VI-11: Collection efficiency on the surface of a single rotor blade following re-injection and re-impingement

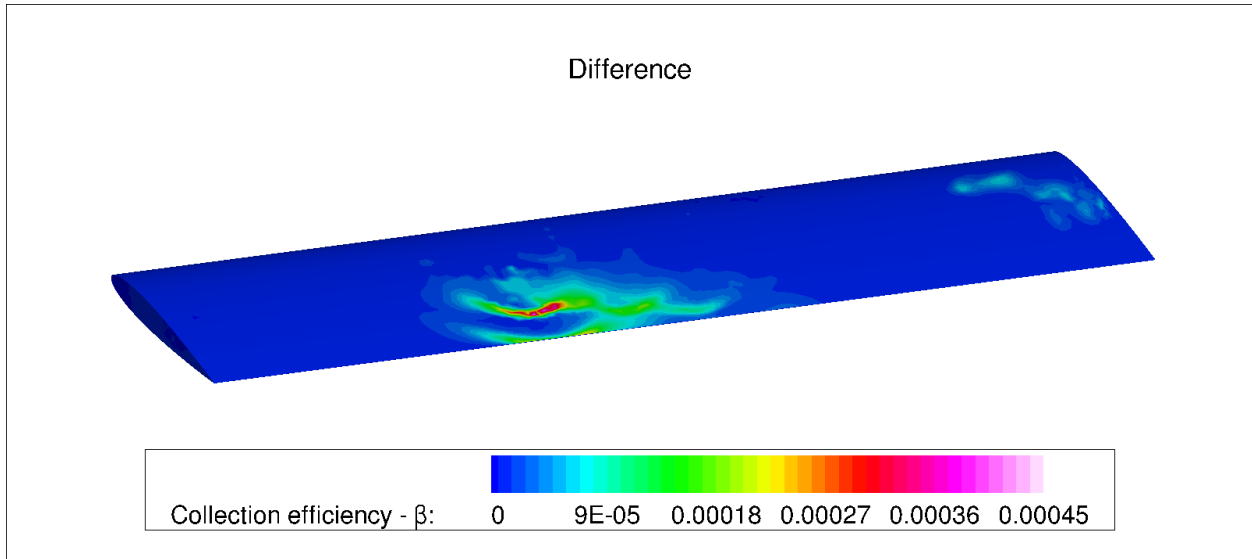


Figure VI-12: Collection efficiency on the surface of a single rotor blade, comparing a post-process and re-injected approach

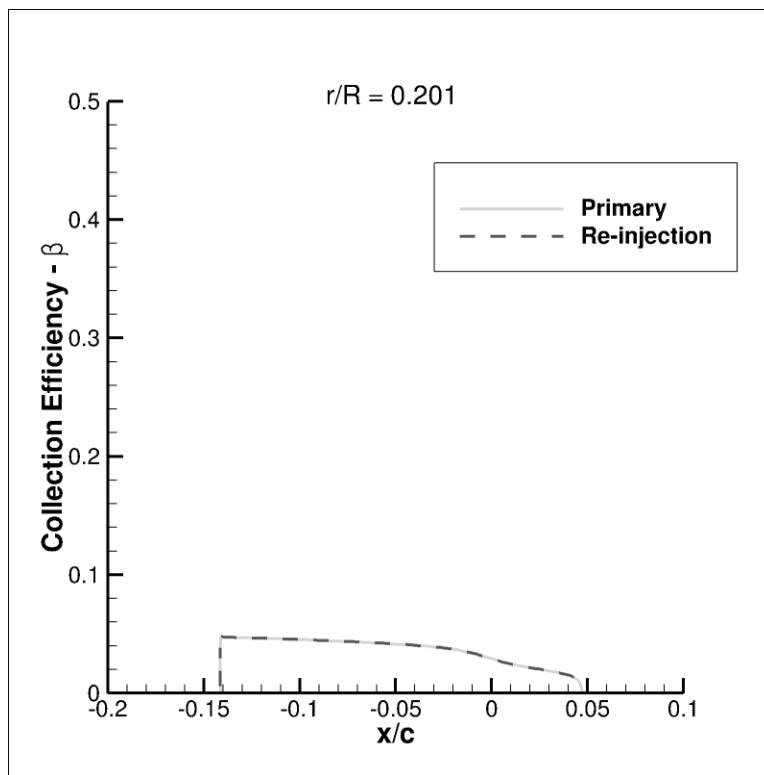


Figure VI-13: Collection efficiency comparing primary impingement and final solution post re-injection at  $r/R = 0.201$

Figure VI-13 shows a comparison between the primary collection efficiency and that considering splashing and bouncing using the clustered approach at  $r/R = 0.201$ . In the region close to the root, there is relatively little mass predicted to splash or bounce. Figure VI-14

shows the same collection efficiency comparison at  $r/R = 0.402$ . Like the  $r/R = 0.201$ , relatively little mass is predicted to splash or bounce, though some does near the trailing edge. There is also a local increase directly at the trailing edge, as the droplets that do re-impinge are drawn by the flow around the trailing edge.

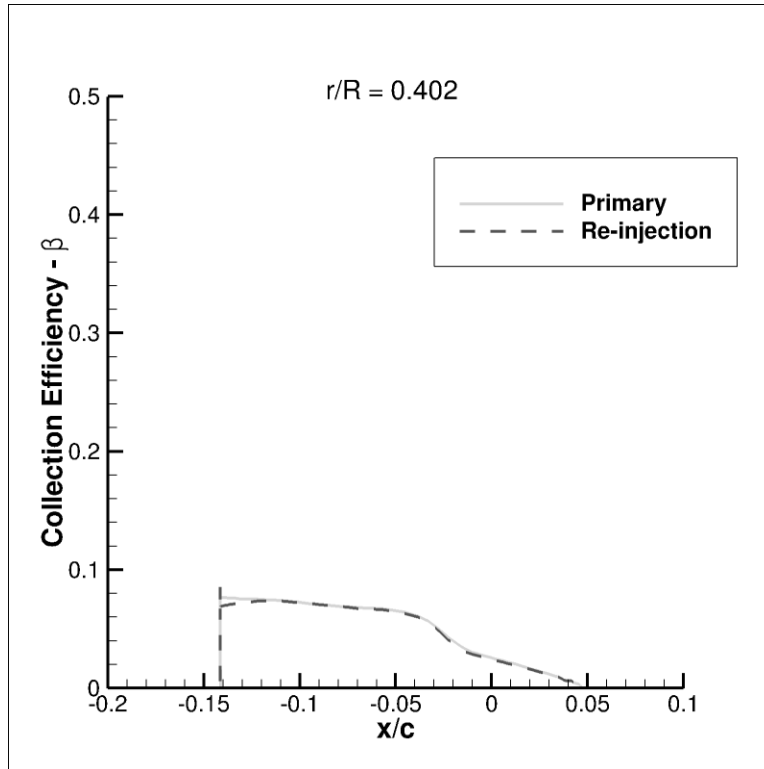


Figure VI-14: Collection efficiency comparing primary impingement and final solution post re-injection at  $r/R = 0.402$

Figure VI-15, Figure VI-16 and Figure VI-17 show the collection efficiency difference at the  $r/R = 0.604$ ,  $r/R = 0.805$ , and  $r/R = 0.938$  locations, respectively. There is progressively greater and greater mass that is predicted to splash and bounce, primarily due to the increase in impinging velocity. The region with the highest collection efficiency is the  $r/R = 0.938$ . Regions beyond this radial location approaching the tip are heavily impacted by the presence of tip vortices, as seen in Figure VI-18, pushing the droplets of a relatively small size away from the surface. Since the large droplets form only a small portion the Freezing Drizzle distribution of Appendix O, the vortex effectively shields the tip from impingement, though acts to increase the impingement in the region just inboard of this shielding as seen in Figure VI-19.

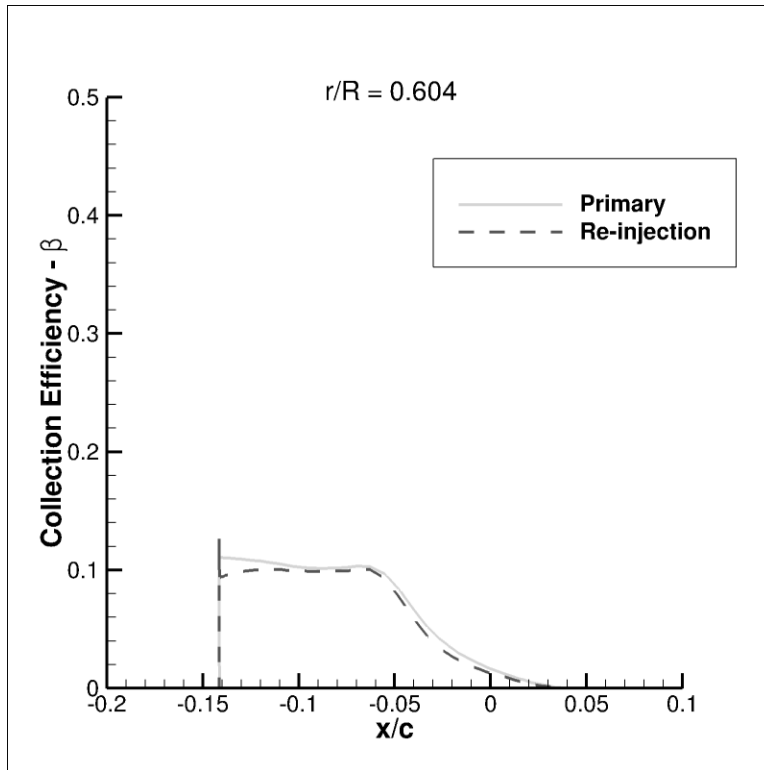


Figure VI-15: Collection efficiency comparing primary impingement and final solution post re-injection at  $r/R = 0.604$

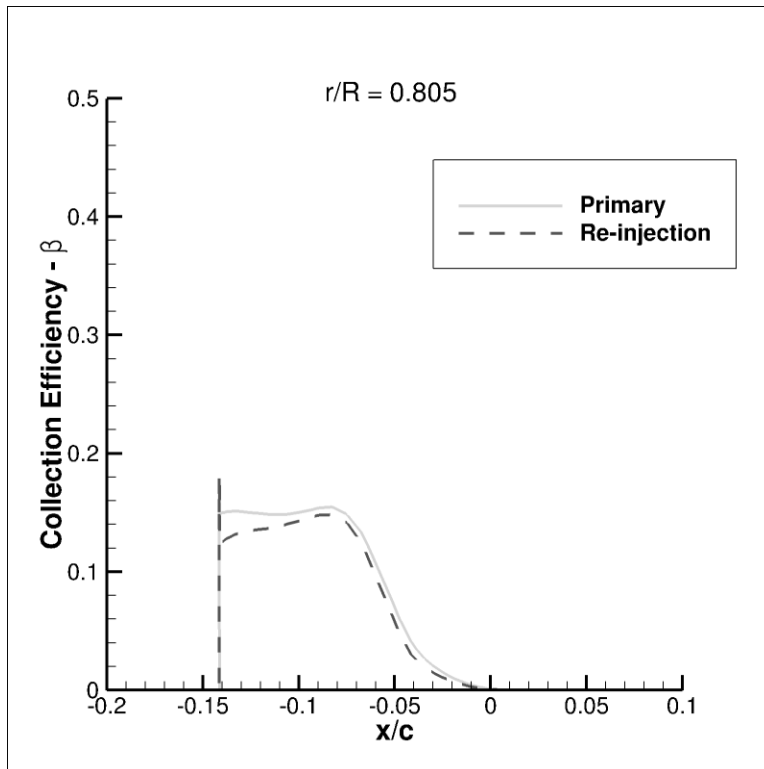


Figure VI-16: Collection efficiency comparing primary impingement and final solution post re-injection at  $r/R = 0.805$

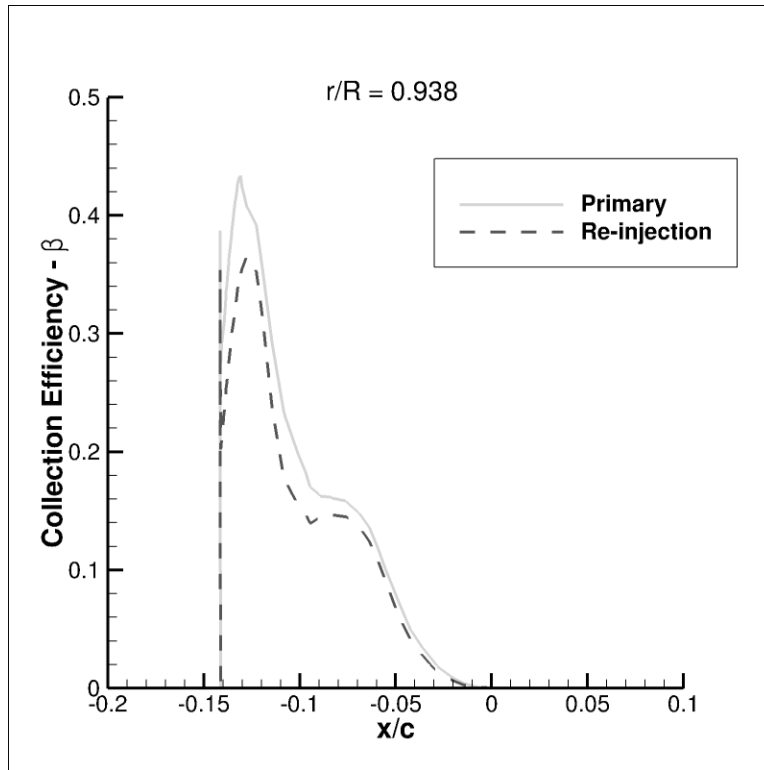


Figure VI-17: Collection efficiency comparing primary impingement and final solution post re-injection at  $r / R = 0.938$

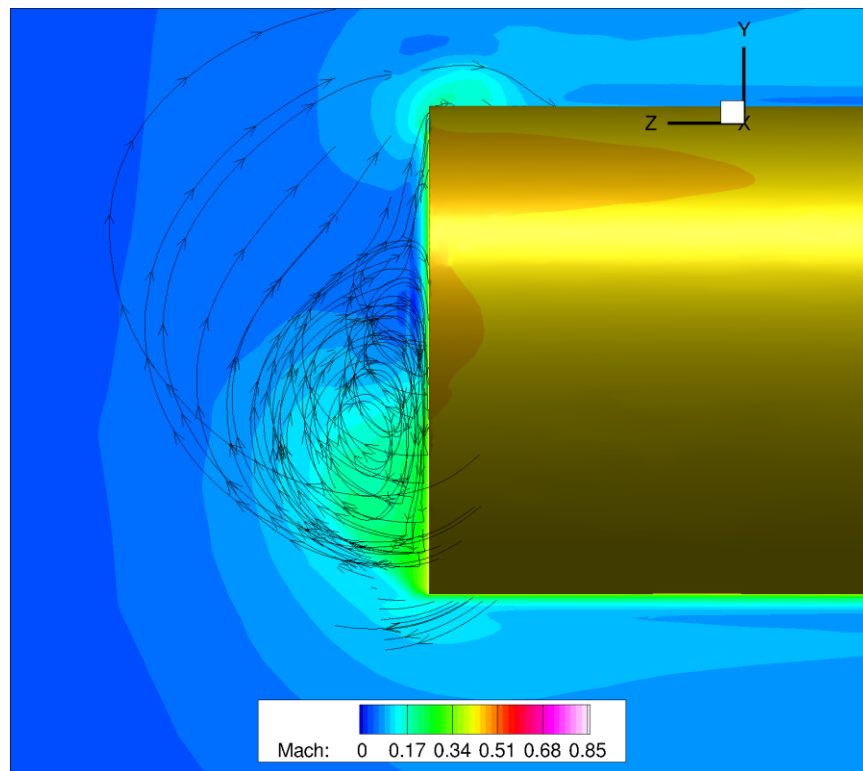


Figure VI-18: Mach contours near the tip of the Caradonna geometry with select streamlines to show the tip vortices

While the use of re-injection to understand the splashing and bouncing in this case did not alter significantly the collection efficiency on the rotor over that of a simple post-process approach, with the exception of the trailing edge, the advantage of the re-injection approach may be found in the interaction of the droplets with a fuselage. Figure VI-20 shows that some of the mass from splashing and bouncing that is re-injected may have impacted on the fuselage located below the rotor. To have an idea of the magnitude of the potential impingement, the LWC passing through a plane at a distance  $y/R=0.10$  below the rotor was generated. Figure VI-21 shows the LWC contours at this distance, with a very low quantity of liquid mass predicted to arrive at this distance due to splashing and bouncing. It is possible that should this rotor be subjected to alternative conditions, additional liquid water would be present below the rotor and possibly enter the engines.

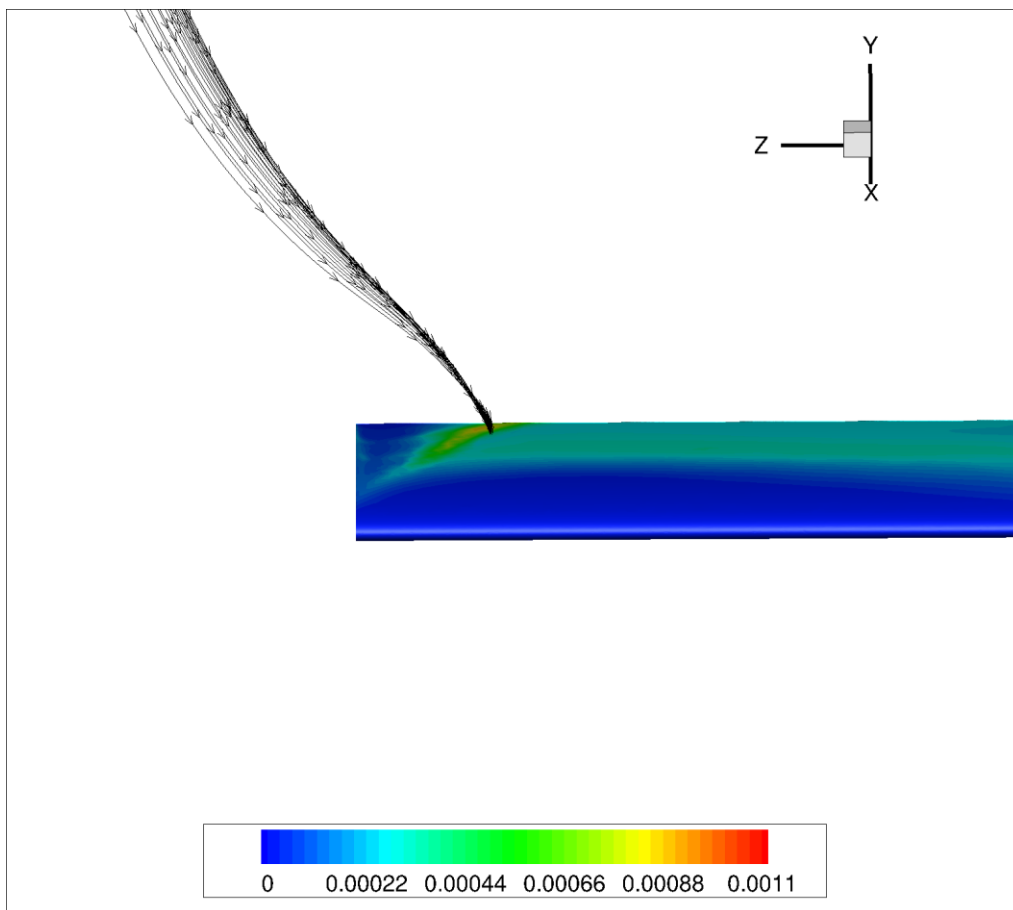


Figure VI-19: Primary droplet streamlines due to tip vortices. Surface contour is LWC

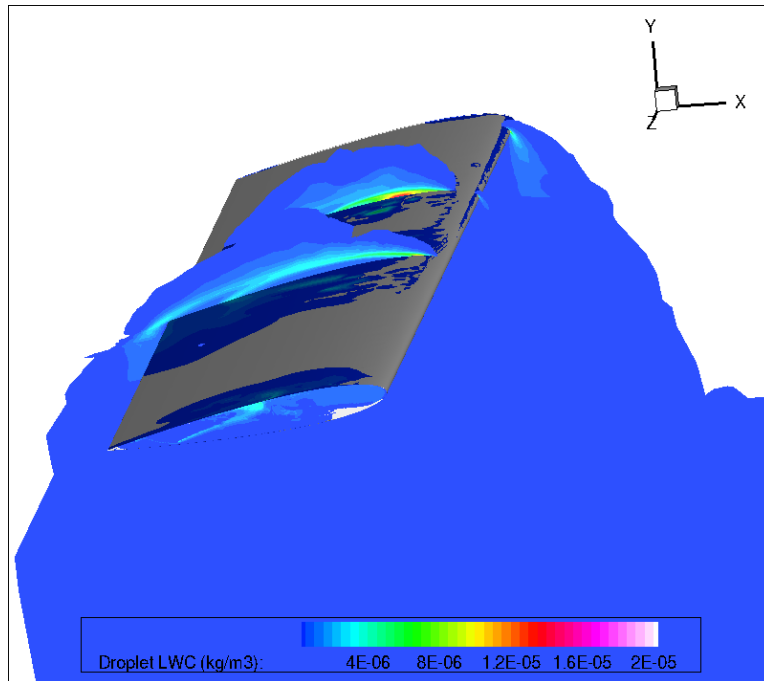


Figure VI-20: LWC contours from the re-injected droplets. Values below  $2E-07$  are blanked

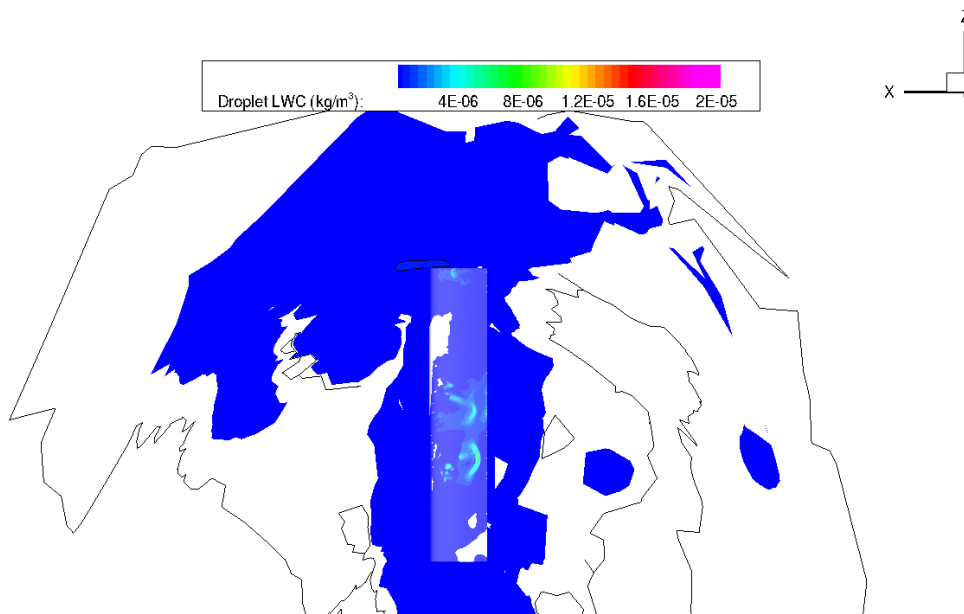


Figure VI-21: LWC contours on the rotor and at a distance  $y/R = 0.10$  below the rotor. Values below  $1E-7$  are truncated to better show the region potentially impacted by the re-injection

An ice solution, including runback was computed for this test case, and trailing edge detachment was predicted along the blade. In this instance, incredibly minor amounts of liquid were predicted to detach from the blade, resulting in a change in the ice and film less than

0.001% compared to the reference solution not considering detachment. The liquid that was predicted to detach was not predicted to re-impinge. This negligible effect of detachment is likely due to several factors. The first is the low primary LWC, resulting in small amounts of liquid on the surface, which are more likely to freeze due to the small amount of energy exchange needed to convert the liquid to solid state. In regions where the rotation causes a local increase in the surface temperature, there remains very little liquid due both to the low primary LWC and the relatively high splashing and bouncing effects. Finally, due to the rotation of the blades, the droplets that detach are unlikely to impinge on the blade again and are simply transported along with the freestream airflow downward and away from the rotor.

## Chapter VII CONCLUSIONS

A previously proposed approach for accounting for the splashing and bouncing of supercooled large droplets in an Eulerian framework has been extended to three-dimensions. The three-dimensional counterpart is extremely costly, even while reducing the degrees of freedom of the secondary droplet simulations. Without an a priori knowledge of the effect of splashing and bouncing on the geometry being studied, it is difficult to justify the computational expense that the approach requires to determine the full effect of splashing and bouncing.

An alternative, lower cost approach was also explored. To do so, the well-posedness of the partial differential equations governing droplet impingement is shown to hold even with discontinuous, non-smooth boundary conditions. This well-posedness allows for the combination of surface facets with unique inlet conditions. While this combination doesn't reduce the degrees of freedom of the secondary droplet simulations, it reduces the number of secondary simulations that must be run from the number of splashing and bouncing regions to a significantly lower number. This is accomplished through the introduction of clustering. Agglomerative Hierarchical clustering groups all surface facets into a single cluster of inlets with relationships defining potential dissimilarity between facets and clusters being stored for later use. Divisive Hierarchical clustering is then employed with the  $Je(2)/Je(1)$  stopping criterion from Duda and Hart being used to determine the natural number of clusters contained within the agglomerated cluster.

Criteria have been proposed to assign a dissimilarity/error value between facets and clusters. The first offers a first order approximation that mass re-injected from one facet could impact on another facet or cluster and is based on the inlet droplet vectors and a line joining the facets centroids. A second criterion looks at the difference in the inlet diameter and has the effect of grouping splashed droplets with other splashed droplets and bounced with other bounced. A third criterion is introduced to assist with numeric stability by comparing the inlet velocities.

This new approach that makes use of clustering to group secondary inlets is tested on both two-dimensional and three-dimensional geometries. On the two-dimensional geometry, both the un-clustered approach and the clustered approach are considered with comparison to

evaluate the error introduced by the clustered facets. While up to an 18% error is found on the aerodynamic performance after the computation of an ice shape, the clustered approach offers more than two orders of magnitude reduction in computational expense. As such, this approach can be used to provide justification for the added expense of the non-clustered approach should the clustered approach identify the potential for significant impact of splashed and bounced droplets.

The clustered approach is applied to a multi-element Trap-wing with slat and flap extended and a comparison is made between a post-process approach and the clustered approach. An almost 25% increase in the mass of ice in five minutes is found with significant increases to the ice affected regions of the lower surface, leading to potentially greater drag due to surface roughness. This significant increase predicted by the clustered approach can be used in connection with sound engineering judgement to justify the added expense of the non-clustered approach when exploring the regions affected by SLD splashing and bouncing. Alternatively, when the clustered approach is applied to an isolated rotor in a hover condition, relatively little difference is found on both the rotor and at a distance below the rotor indicative of the distance to a rotorcraft body. In this case, the clustered approach confirms what engineering judgement would suggest, that very little SLD splashing and bouncing will re-impinge and the added expense of computing the non-clustered approach is not needed.

A model and an approach were proposed to account for the detachment of droplets that have run back along a surface to a trailing edge. The two-dimensional model assumed one-way coupling with the aerodynamic solution and sought to account for the forces acting on a circular cross-section. Forces considered included surface tension, gravity, buoyancy, pressure and shear stress. No experimental data was found for validation. A sensitivity study was performed and the model was found to only be sensitive to extremely dissimilar conditions around sharp corners, such as when flow separation occurs resulting in strong pressure differences and very different values of shear stress. When the two-dimensional model was extended to three-dimensions, the assumption of one-way coupling was found to introduce significant error at all but the lowest freestream velocities.

A new three-dimensional model was proposed making use of a combined drag equation found in the literature to account for pressure and shear stress forces. An expression for the fitting coefficient based off numeric values, rather than experimental values was proposed. The three-dimensional model assumed a spherical cap shape with respect of the contact angle between the liquid and solid phases. By extending the angle of a sharp corner to approach that of a flat plate the three-dimensional model was partially validated against the work of Theodorakakos, *et al.* who experimented on droplet detachment in micro-channels. Good agreement was found with the results for the different surfaces employed in the experiments.

The three-dimensional detachment model was applied to the Trap-wing with a negligible impact on the surface deposition being observed. Peak collection efficiency due to detached droplets was 2-3 orders of magnitude lower than primary collection efficiency. The effect on final ice-shape was also negligible. A turbofan blade was also explored as the effect of higher surface temperature; higher inlet liquid water content and shorter chord length were presumed to provide ideal conditions for trailing edge detachment. Again, little effect was noted, with less than 0.003% increase in liquid water passing to the next stage in the turbomachine. It is believed that the detachment in a turbomachine due primarily to centrifugal forces *during* runback is the most critical, with little mass arriving at the trailing edge as a liquid.

A final test case was explored in the form of an isolated rotor in hover. An Appendix O, Freezing Drizzle distribution was studied with the clustered approach being used to determine splashing and bouncing effects on the collection efficiency. In this case, very little secondary mass impinges on rotor and the bulk of the mass being carried away from the rotor. Some secondary droplets are driven downward toward the location where a fuselage may be impacted, but the liquid water content is very low compared to the primary liquid water content in the same region. While the secondary impingement was a negligible phenomenon in this case, the effect of splashing and bouncing reduced the peak collection efficiency on the rotor by about 25% and the total collection efficiency by more than 7%. As such, splashing and bouncing must be considered, though the clustered approach suggests that a more detailed study of the

secondary droplets is not necessary in this case. The three-dimensional detachment model was also applied, again with a negligible effect.

## **Chapter VIII FUTURE WORK**

Future work includes the study of droplet detachment from rotating surfaces during liquid runback. In the framework of a turbomachine, while there is some liquid that arrives at a trailing edge, much of the liquid may be ejected from the surface during the runback due to the strong centrifugal forces. Future studies will include both the numerical detection of location where detachment is likely to occur, along with a study of the dominant forces acting on the liquid. Additionally, the use of multi-scale modeling to determine the contact angle would remove one of the limitations of the detachment model (that the contact angles are explicitly known and have a set variation along the contact line).

In addition to a study of the location of detachment, a study of the effect of the assumed shape should be performed to determine if a continuous film, rivulets or discrete droplets would have an effect on the quantity of liquid determined to detach and the diameter of the subsequent droplets. While the notion of an isolated droplet allows for simplification in the computation of the forces acting on the liquid, alternative descriptions of the liquid surface may improve the prediction of the detachment of liquid.

## Chapter IX REFERENCES

1. Duda, R.O. and Hart, P.E., *Pattern Classification and Scene Analysis*. 1973, New York: John Wiley and Sons.
2. Caliński, T. and Harabasz, J., *A Dendrite Method for Cluster Analysis*. *Communications in Statistics-Theory and Methods*, 1974. **Vol. 3**(1): pp. 1-27, DOI: 10.1080/03610927408827101.
3. Hubert, L.J. and Levin, J.R., *A General Statistical Framework for Assessing Categorical Clustering in Free Recall*. *Psychological Bulletin*, 1976. **Vol. 83**(6): pp. 1072, DOI: 10.1037/0033-2909.83.6.1072.
4. Zhang, F.Y., Yang, X.G., and Wang, C.Y., *Liquid Water Removal from a Polymer Electrolyte Fuel Cell*. *Journal of the Electrochemical Society*, 2006. **Vol. 153**(2): pp. A225-A232, DOI: 10.1149/1.2138675.
5. Habashi, W.G., *Recent Advances in CFD for In-Flight Icing Simulations*. *Japan Society of Fluid Mechanics*, 2009. **Vol. 28**(2): pp. 99-118.
6. FAA, *Airworthiness Standards: Transport Category Airplanes*, in *Appendix C to Part 25, Title 14*, 2009, Federal Aviation Administration.
7. FAA, *Airworthiness Standards: Transport Category Airplanes*, in *Appendix O to Part 25, Title 14 - Supercooled Large Drop Icing Conditions*, 2014, Federal Aviation Administration.
8. NTSB, *In-Flight Icing Encounter and Loss of Control*, 1994: National Transportation Safety Board, Washington, D.C.
9. Papadakis, M., Rachman, A., Wong, S., Bidwell, C., and Bencic, T.J., *An Experimental Investigation of SLD Impingement on Airfoils and Simulated Ice Shapes*, 2003: SAE Technical Paper 2003-01-2129, DOI: 10.4271/2003-01-2129.
10. Honsek, R., *Development of a Three-Dimensional Eulerian Model of Droplet-Wall Interaction Mechanisms*, in *Department of Mechanical Engineering*, 2005, Masters Thesis, McGill University: Montreal, QC. pp. 110.
11. Brahim, M.T., Tran, P., Chocron, D., Tezok, F., and Paraschivoiu, I., *Effect of Supercooled Large Droplets on Ice Accretion Characteristics*. in *35<sup>th</sup> Aerospace Sciences Meeting and Exhibit 1997*. Reno, NV: AIAA Paper-97-0306.
12. Tan, S.C. and Papadakis, M., *General Effects of Large Droplet Dynamics on Ice Accretion Modeling*. in *41<sup>st</sup> Aerospace Sciences Meeting and Exhibit*, 2003. Reno, NV: AIAA Paper-2003-0392.
13. Honsek, R. and Habashi, W.G., *FENSAP-ICE: Eulerian Modeling of Droplet Impingement in the SLD Regime of Aircraft Icing*. in *44<sup>th</sup> AIAA Aerospace Sciences Meeting and Exhibit*, 2006. Reno, NV: AIAA Paper-2006-0465.
14. Rutkowski, A., Wright, W.B., and Potapczuk, M.G., *Numerical Study of Droplet Splashing and Re-impingement*. in *41<sup>st</sup> Aerospace Sciences Meeting and Exhibit*, 2003. Reno, NV: AIAA Paper-2003-388.
15. Wright, W.B. and Potapczuk, M.G., *Semi-Empirical Modeling of SLD Physics*. in *42<sup>nd</sup> Aerospace Sciences Meeting and Exhibit*, 2004. Reno, NV: AIAA Paper-2004-0412.
16. Wright, W.B., *Further Refinement of the LEWICE SLD Model*. in *44<sup>th</sup> AIAA Aerospace Sciences Meeting and Exhibit*, 2006. Reno, NV: AIAA Paper-2006-0464.
17. Beaugendre, H., Morency, F., and Habashi, W.G., *FENSAP-ICE's Three-Dimensional In-Flight Ice Accretion Module: ICE3D*. *Journal of Aircraft*, 2003. **Vol. 40**(3), DOI: 10.2514/2.3113.
18. Aliaga, C.N., Aubé, M.S., Baruzzi, G.S., and Habashi, W.G., *FENSAP-ICE UNSTEADY: A Unified In-Flight Icing Simulation Methodology for Aircraft, Rotorcraft and Jet Engines*. *AIAA Journal of Aircraft*, 2011. **Vol. 48**(1): pp. 119-126.

19. Beaugendre, H., *A PDE-Based 3D Approach to In-Flight Ice Accretion*, in *Department of Mechanical Engineering*, 2003, Doctoral Thesis, McGill University: Montreal, QC. pp. 196.
20. Bourgault, Y., Beaugendre, H., and Habashi, W.G., *Development of a Shallow-Water Icing Model in FENSAP-ICE*. *Journal of Aircraft*, 2000. **Vol. 37**(4): pp. 640-646, DOI: 10.2514/2.2646.
21. Morency, F., Beaugendre, H., and Habashi, W.G., *FENSAP-ICE: A Navier-Stokes Eulerian Droplet Impingement Approach for High-Lift Devices*. in *Canadian Aeronautics and Space Institute: 48<sup>th</sup> Annual Conference*. 2001. Toronto, ON. pp. 277-282.
22. Sussman, M., Smereka, P., and Osher, S., *A Level Set Approach for Computing Solutions to Incompressible Two-Phase Flow*. *Journal of Computational Physics*, 1994. **Vol. 114**(1), DOI: 10.1006/jcph.1994.1155.
23. Bakkar, A., Habashi, W.G., Baruzzi, G.S., and Fossati, M., *A Hybrid Taylor-Galerkin Variational Multi-Scale Stabilization Method for the Level Set Equation*. *Computers & Fluids*, 2015. **Vol. 121**: pp. 192–205, DOI: 10.1016/j.compfluid.2015.08.008.
24. Sussman, M. and Puckett, E.G., *A Coupled Level Set and Volume-of-Fluid Method for Computing 3D and Axisymmetric Incompressible Two-Phase Flows*. *Journal of Computational Physics*, 2000. **Vol. 162**(2): pp. 301–337, DOI: 10.1006/jcph.2000.6537.
25. Bourgault, Y., Habashi, W.G., Dompierre, J., and Baruzzi, G.S., *A Finite Element Method Study of Eulerian Droplet Impingement Models*. *International Journal for Numerical Methods in Fluids*, 1999. **Vol. 29**(4): pp. 429-449, DOI: 10.1002/(SICI)1097-0363(19990228)29:4<429::AID-FLD795>3.0.CO;2-F.
26. Wright, W.B., *Validation Results for LEWICE 3.0*. in *43<sup>rd</sup> AIAA Aerospace Sciences Meeting and Exhibit*, 2005. Reno, NV: AIAA Paper-2005-1243.
27. Durst, F., Milojevic, D., and Schönung, B., *Eulerian and Lagrangian Predictions of Particulate Two-Phase Flows: A Numerical Study*. *Applied Mathematical Modeling*, 1984. **Vol. 8**: pp. 101-115, DOI: 10.1016/0307-904X(84)90062-3.
28. Cliff, R., Grace, J.R., and Weber, M.E., *Bubbles, Drops and Particles*. 1978, New York: Academic Press.
29. Pilch, M. and Erdman, C.A., *Use of Breakup Time Data and Velocity History Data to Predict the Maximum Size of Stable Fragments for Acceleration-Induced Breakup of a Liquid Drop*. *International Journal of Multiphase Flow*, 1987. **Vol. 13**(6): pp. 741-757.
30. Newmerical Technologies International Inc., *FENSAP-ICE User Manual*, 2013. pp. 113, Montreal, QC.
31. Bilodeau, D.R., *An Eulerian Framework for Supercooled Large Droplets Splashing and Bouncing*, in *Department of Mechanical Engineering*, 2013, Masters Thesis, McGill University: Montreal, QC. pp. 95.
32. Bilodeau, D.R., Habashi, W.G., Fossati, M., and Baruzzi, G.S., *Eulerian Modeling of Supercooled Large Droplet Splashing and Bouncing*. *Journal of Aircraft*, 2015. **Vol. 52**(5): pp. 1611-1624, DOI: 10.2514/1.C033023.
33. Bai, C. and Gosman, A.D., *Development of Methodology for Spray Impingement Simulation*. SAE Technical Report 950283, 1995, DOI: 10.4271/950283.
34. Mundo, C., Sommerfeld, M., and Tropea, C., *Droplet-Wall Collisions: Experimental Studies of the Deformation and Breakup Process*. *International Journal of Multiphase Flow*, 1995. **Vol. 21**(2): pp. 151-173, DOI: 10.1016/0301-9322(94)00069-V.
35. Mundo, C., Tropea, C., and Sommerfeld, M., *Numerical and Experimental Investigation of Spray Characteristics in the Vicinity of a Rigid Wall*. *Experimental Thermal and Fluid Science*, 1997. **Vol. 15**: pp. 228-237, DOI: 10.1016/S0894-1777(97)00015-0.
36. Mundo, C., Sommerfeld, M., and Tropea, C., *On the Modeling of Liquid Sprays Impinging on Surfaces*. *Atomization and Sprays*, 1998. **Vol. 8**: pp. 625-652, DOI: 10.1615/AtomizSpr.v8.i6.20

37. Trujillo, M.F., Mathews, W.S., Lee, C.F., and Peters, J.E., *Modeling and Experiment of Impingement and Atomization of a Liquid Spray on a Wall*. International Journal of Engine Research, 2000. **Vol. 1**(1): pp. 87-105, DOI: 10.1243/1468087001545281.
38. Stow, C.D. and Hadfield, M.G., *An Experimental Investigation of Fluid Flow Resulting From the Impact of a Water Drop With an Unyielding Dry Surface*. Proceedings of the Royal Society of London, 1981. **Vol. A373**: pp. 419-441, DOI: 10.2307/2397009.
39. Yarin, A.L. and Weiss, D.A., *Impact of Drops on Solid Surfaces: Self-Similar Capillary Waves and Splashing as a New Type of Kinematic Discontinuity*. Journal of Fluid Mechanics, 1995. **Vol. 283**: pp. 141-173.
40. Moreira, A.L.N., Moita, A.S., and Pañão, M.R., *Advances and Challenges in Explaining Fuel Spray Impingement: How Much of Single Droplet Impact Research is Useful?* Progress in Energy and Combustion Science, 2010. **Vol. 36**: pp. 554-580, DOI: 10.1016/j.pecs.2010.01.002.
41. Luliano, E., *3D Ice Accretion Simulation in SLD Conditions*, in *EXTICE: EXTreme Icing Environment*, 2012: Capua, Italy.
42. Mingione, G., Luliano, E., Guffond, D., and Tropea, C., *EXTICE: EXTreme Icing Environment*. in *SAE 2011 International Conference on Aircraft and Engine Icing and Ground Deicing*. 2011. Chicago, IL: 2011-38-0063.
43. *Icing Wind Tunnel Interfacility Comparison Tests*, 2012, SAE-AIR5666. p. 107.
44. Jung, S.K. and Kim, J.H., *Numerical Model for Eulerian Droplet Impingement in Supercooled Large Droplet Conditions*. in *51<sup>st</sup> AIAA Aerospace Sciences Meeting*, 2013. Dallas, TX: AIAA Paper-2013-0244.
45. Papadakis, M., Rachman, A., Wong, S., Yeong, H., Kuohsing, E., Giao, T., and Bidwell, C., *Water Droplet Impingement on Simulated Glaze, Mixed, and Rime Ice Accretions*, 2007, NASA/TM Paper 2007-213961.
46. Bilodeau, D.R., Habashi, W.G., and Fossati, M., *Numerical Modeling of Supercooled Large Droplets Re-impingement*. in *21<sup>st</sup> Annual Conference of the CFD Society of Canada*, 2013. Sherbrooke, QC.
47. Bilodeau, D.R., Habashi, W.G., Fossati, M., and Baruzzi, G.S., *An Eulerian Re-impingement Model of Splashing and Bouncing Supercooled Large Droplets*. in *5<sup>th</sup> AIAA Atmospheric and Space Environments Conference*, 2013. San Diego, CA: AIAA Paper-2013-3058.
48. Sibson, R., *SLINK: An Optimally Efficient Algorithm for the Single-Link Cluster Method*. The Computer Journal, 1973. **Vol. 16**(1): pp. 30-34, DOI: 10.1093/comjnl/16.1.30.
49. Hartigan, J.A. and Wong, M.A., *Algorithm AS 136: A K-Means Clustering Algorithm*. Journal of the Royal Statistical Society. Series C (Applied Statistics), 1979. **Vol. 28**(1): pp. 100-108, DOI: 10.2307/2346830
50. Fraley, C. and Raftery, A.E., *Model-Based Clustering, Discriminant Analysis, and Density Estimation*. Journal of the American statistical Association, 2002. **Vol. 97**(458): pp. 611-631, DOI: 10.1198/016214502760047131.
51. Milligan, G.W. and Cooper, M.C., *An Examination of Procedures for Determining the Number of Clusters in a Data Set*. Psychometrika, 1985. **Vol. 50**(2): pp. 159-179, DOI: 10.1007/BF02294245.
52. El-Hamdouchi, A. and Willett, P., *Comparison of Hierarchic Agglomerative Clustering Methods for Document Retrieval*. The Computer Journal, 1989. **Vol. 32**(3): pp. 220-227, DOI: 10.1093/comjnl/32.3.220.
53. Bensaou, M. and Venkatraman, N., *Configurations of Interorganizational Relationships: A Comparison Between US and Japanese Automakers*. Management Science, 1995. **Vol. 41**(9): pp. 1471-1492, DOI: 10.1287/mnsc.41.9.1471.
54. Schillberg, C.H. and Kandlikar, S.G., *A Review of Models for Water Droplet Detachment from the Gas Diffusion Layer-Gas Flow Channel Interface in PEMFCs*. in *ASME 5<sup>th</sup> International Conference*

- on Nanochannels, Microchannels and Minichannels, 2007. Puebla, MX: ICNMM2007-30029. pp. 299-310.
55. Chen, K.S., Hickner, M.A., and Noble, D.R., *Simplified Models for Predicting the Onset of Liquid Water Droplet Instability at the Gas Diffusion Layer/Gas Flow Channel Interface*. International Journal of Energy Research, 2005. **Vol. 29**(12): pp. 1113-1132, DOI: 10.1002/er.1143.
  56. Kumbur, E.C., Sharp, K.V., and Mench, M.M., *Liquid Droplet Behavior and Instability in a Polymer Electrolyte Fuel Cell Flow Channel*. Journal of Power Sources, 2006. **Vol. 161**(1): pp. 333-345, DOI: 10.1016/j.jpowsour.2006.04.093.
  57. Fortin, G., Laforte, J., and Beisswenger, A., *Prediction of Ice Shapes on NACA0012 2D Airfoil*, 2003: SAE Technical Paper 2003-01-2154, DOI: 10.4271/2003-01-2154.
  58. Mansour, A. and Chigier, N., *Dynamic Behavior of Liquid Sheets*. Physics of Fluids A: Fluid Dynamics (1989-1993), 1991. **Vol. 3**(12): pp. 2971-2980.
  59. Ponter, A.B., Davies, G.A., Ross, T.K., and Thornley, P.G., *The Influence of Mass Transfer on Liquid Film Breakdown*. International Journal of Heat and Mass Transfer, 1967. **Vol. 10**(3): pp. 349-352, DOI: 10.1016/0017-9310(67)90151-2.
  60. Craster, R.V. and Matar, O.K., *Dynamics and Stability of Thin Liquid Films*. Reviews of modern physics, 2009. **Vol. 81**(3): pp. 1131, DOI: 10.1103/RevModPhys.81.1131.
  61. Wilson, S.K. and Duffy, B.R., *When is it Energetically Favorable for a Rivulet of Perfectly Wetting Fluid to Split?* Physics of Fluids (1994-present), 2005. **Vol. 17**(7): pp. 078104, DOI: 10.1063/1.1979521.
  62. Lasheras, J.C., Villermaux, E., and Hopfinger, E.J., *Break-up and Atomization of a Round Water Jet by a High-Speed Annular Air Jet*. Journal of Fluid Mechanics, 1998. **Vol. 357**: pp. 351-379, DOI: 10.1017/S0022112097008070.
  63. Okawa, T., Kitahara, T., Yoshida, K., Matsumoto, T., and Kataoka, I., *New Entrainment Rate Correlation in Annular Two-Phase Flow Applicable to Wide Range of Flow Condition*. International Journal of Heat and Mass Transfer, 2002. **Vol. 45**(1): pp. 87-98, DOI: 10.1016/S0017-9310(01)00111-9.
  64. van Rossum, J.J., *Experimental Investigation of Horizontal Liquid Films: Wave Formation, Atomization, Film Thickness*. Chemical Engineering Science, 1959. **Vol. 11**(1): pp. 35-52, DOI: 10.1016/0009-2509(59)80071-3.
  65. Basu, S., Nandakumar, K., and Masliyah, J.H., *A Model for Detachment of a Partially Wetting Drop From a Solid Surface by Shear Flow*. Journal of Colloid and Interface Science, 1997. **Vol. 190**(1): pp. 253-257, DOI: 10.1006/jcis.1997.4856.
  66. Goldman, A.J., Cox, R.G., and Brenner, H., *Slow Viscous Motion of a Sphere Parallel to a Plane Wall—II Couette Flow*. Chemical Engineering Science, 1967. **Vol. 22**(4): pp. 653-660, DOI: 10.1016/0009-2509(67)80048-4.
  67. Hubbe, M.A., *Theory of Detachment of Colloidal Particles from Flat Surfaces Exposed to Flow*. Colloids and Surfaces, 1984. **Vol. 12**: pp. 151-178, DOI: 10.1016/0166-6622(84)80096-7.
  68. Edwards, A.W.F. and Cavalli-Sforza, L.L., *A Method for Cluster Analysis*. Biometrics, 1965: pp. 362-375, DOI: 10.2307/2528096.
  69. Defays, D., *An Efficient Algorithm for a Complete Link Method*. The Computer Journal, 1977. **Vol. 20**(4): pp. 364-366, DOI: 10.1093/comjnl/20.4.364.
  70. Olson, C.F., *Parallel Algorithms for Hierarchical Clustering*. Parallel Computing, 1995. **Vol. 21**(8): pp. 1313-1325, DOI: 10.1016/0167-8191(95)00017-1.
  71. Papadakis, M., Hung, K.E., Vu, G.T., Yeong, H.W., Bidwell, C., Breer, M.D., and Bencic, T.J., *Experimental Investigation of Water Droplet Impingement on Airfoils, Finite Wings, and an S-Duct Engine Inlet*, 2002, Technical Report, NASA/TM-2002-211700: NASA.

72. Wright, W.B., Potapczuk, M.G., and Levinson, L.H., *Comparison of LEWICE and GlennICE in the SLD Regime*. in *46<sup>th</sup> AIAA Aerospace Sciences Meeting and Exhibit*, 2008. Reno, NV: AIAA Paper-2008-0439.
73. Fossati, M., Guardone, A., and Vigevano, L., *A Node-Pair Finite Element/Volume Mesh Adaptation Technique for Compressible Flows Based on a Hierarchical Approach*. *International Journal for Numerical Methods in Fluids*, 2012. **Vol. 70**(8): pp. 1004-1026, DOI: 10.1002/flid.2728.
74. Dussin, D., Fossati, M., Guardone, A., and Vigevano, L., *Hybrid Grid Generation for Two-Dimensional High-Reynolds Flows*. *Computers & Fluids*, 2009. **Vol. 38**(10): pp. 1863-1875, DOI: 10.1016/j.compfluid.2009.04.007.
75. Hamby, D.M., *A Review of Techniques for Parameter Sensitivity Analysis of Environmental Models*. *Environmental Monitoring and Assessment*, 1994. **Vol. 32**(2): pp. 135-154, DOI: 10.1007/BF00547132.
76. Ho, Y.C., *Perturbation Analysis Explained*. *IEEE Transactions on Automatic Control*, 1988. **Vol. 33**(8): pp. 761-763, DOI: 10.1109/9.1294.
77. Theodorakakos, A., Ous, T., Gavaises, M., Nouri, J.M., Nikolopoulos, N., and Yanagihara, H., *Dynamics of Water Droplets Detached from Porous Surfaces of Relevance to PEM Fuel Cells*. *Journal of Colloid and Interface Science*, 2006. **Vol. 300**(2): pp. 673-687, DOI: 10.1016/j.jcis.2006.04.021.
78. Ous, T. and Arcoumanis, C., *Visualisation of Water Droplets During the Operation of PEM Fuel Cells*. *Journal of Power Sources*, 2007. **Vol. 173**(1): pp. 137-148, DOI: 10.1016/j.jpowsour.2007.04.075.
79. Zhu, Z., Sui, P.C., and Djilali, N., *Three-Dimensional Numerical Simulations of Water Droplet Dynamics in a PEMFC Gas Channel*. *Journal of Power Sources*, 2008. **Vol. 181**(1): pp. 101-115, DOI: 10.1016/j.jpowsour.2008.03.005.
80. Nilamdeen, S., Senior Developer - Turbomachinery Icing, ANSYS Canada Ltd., *Personal Communication*, 4 March 2016.
81. Caradonna, F.X. and Tung, C., *Experimental and Analytical Studies of a Model Helicopter Rotor in Hover*. in *6<sup>th</sup> European Rotorcraft and Powered Lift Aircraft Forum*, 1981. Bristol.
82. Fouladi, H., *Computational Methods for Rotorcraft Icing*, in *Department of Mechanical Engineering*, 2015, Doctoral Thesis, McGill University: Montreal, QC. pp. 161.
83. Palacios, F., Alonso, J., Duraisamy, K., Colonno, M., Hicken, J., Aranake, A., Campos, A., Copeland, S., Economon, T., Lonkar, A., Lukaczyk, T., and Taylor, T., *Stanford University Unstructured (SU<sup>2</sup>): An Open-Source Integrated Computational Environment for Multi-Physics Simulation and Design*. in *51<sup>st</sup> AIAA Aerospace Sciences Meeting*, 2013. Dallas, TX: AIAA Paper-2013-0287.
84. Allen, C.B., Rendall, T.C.S., and Morris, A.M., *Computational-Fluid-Dynamics-Based Twist Optimization of Hovering Rotors*. *Journal of Aircraft*, 2010. **Vol. 47**(6): pp. 2075-2085, DOI: 10.2514/1.C000316.
85. Guruswamy, G.P., *Computational-Fluid-Dynamics- and Computational-Structural-Dynamics-Based Time-Accurate Aeroelasticity of Helicopter Rotor Blades*. *Journal of Aircraft*, 2010. **Vol. 47**(3): pp. 858-863, DOI: 10.2514/1.45744.